

POLITECNICO DI TORINO

Master's Degree in Aerospace Engineering



Master's Degree Thesis

LOW-ORDER PREDICTION METHODOLOGY
FOR MULTI-ROTORS TONAL NOISE

Supervisor:

Prof. Dominic D'ambrosio

Advisors:

Prof. Arina Renzo

Prof. Christophe Schram

Dr. Julien Christophe

Candidate:

Edoardo Dell'Erba

Academic year 2020/2021

von Karman Institute of Fluid Dynamics

Chaussée de Waterloo, 72

B-1640 Rhode-Saint-Genèse - Belgium



Short Training Program Report 2021

Low-Order Prediction Methodology for Multi-Rotors Tonal Noise

Edoardo Dell'Erba

Supervisor: C. Schram

Advisor: A. Zarri, W. Munters, J. Christophe

March 2021

Acknowledgements

Un percorso durato quasi 6 anni al Politecnico di Torino si conclude con questa tesi. E' stato un periodo duro, in cui le difficoltà non sono state poche, ma mi hanno permesso di crescere personalmente e professionalmente. Vorrei quindi spendere due parole di ringraziamento nei confronti di tutte le persone che mi hanno sostenuto e aiutato durante questo periodo.

I would first like to thank the Von Karman Institute for giving me the opportunity to develop my thesis work. Even if the pandemic got in the way, the VKI allowed me to have an experience that will be invaluable for my future. In particular, I would like to thank Alessandro and Wim for supporting me during these long 6 months, your patience and your advice have been essential for me.

Un sentito grazie a Prof. Domenic D'ambrosio e Prof. Renzo Arina per avermi supportato nella fase più importante del mio percorso accademico.

Un ringraziamento speciale alla mia famiglia, in particolare a mia madre e mio padre: è grazie al vostro sostegno e al vostro incoraggiamento se oggi sono riuscito a raggiungere questo traguardo. Siete il mio punto fisso, una continua fonte di ispirazione e motivazione. Questa laurea è tanto mia, quanto vostra.

Grazie a chi a Torino mi ha sempre sopportato. Riccardo, dalle elementari alle nottate di studio per gli esami, eccoci di nuovo a festeggiare un traguardo insieme. Enrico, sei forse la scoperta più piacevole della mia avventura torinese, grazie per essere diventato una certezza. Albe, Stefano, Antonio, grazie delle tante avventure e delle risate, quando racconterò di questi anni, vi fischieranno spesso le orecchie.

Ringrazio chi c'è da sempre e mi ha fatto capire che l'amicizia vera non conosce distanza. Laura, ormai sei diventata come una sorella, grazie per esserci sempre stata. Simone e Riccardo, non ricordo un momento importante in cui voi non foste con me a festeggiare. Matteo, molto più di un cugino, quanta strada abbiamo fatto da quelle nottate con il gameboy.

Ai miei amici che mi sono stati vicini durante un periodo stressante come questo della scrittura della tesi. Luca, Giovanni, Laura, Stefano, Monte, Enrico T. e tutti gli altri, grazie per tutti i momenti di spensieratezza che mi avete regalato.

Alessia, grazie per avermi accompagnato mano per mano attraverso ogni mio piccolo traguardo, spronandomi sempre ad essere la migliore versione di me stesso. Grazie di esserci stata, sei stata per me fondamentale.

Infine, dedico questa tesi a me stesso, ai miei sacrifici e alla mia tenacia che mi hanno permesso di non mollare mai ed arrivare fin qui.

Abstract

Recent advancements in electric propulsion, autonomous tech solutions, and the need for a faster, safer, and greener way of transports lead to the quick development of Urban Air Mobility. In this background in the past years, electric vertical take-off and landing aircraft (eVTOL) have been largely considered as a solution to the issue of urban traffic congestion. One of the main barriers to large-scale implementation and public acceptance is the noise emitted by this vehicle's class. This is due to the complex aerodynamics caused by the presence of multiple rotors spread across the wings.

The aim of this thesis is to define a computational methodology, which is able to predict the tonal noise generated by a specific class of eVTOL: drones. The DJI Phantom 2 is chosen as the subject of the study, considering its wide use in literature. The coupling of unsteady Reynolds-averaged Navier–Stokes (uRANS) simulations and an analytical reformulation of the Ffowcs-Williams and Hawkings analogy permit to quantify the tonal noise for different configurations. Following the difficulties related to the development of a simulation with the full drone configuration, the final purpose is reached by a sequence of simpler steps:

1. isolated actuator disk case to study the more appropriate setting in terms of domain characteristics and boundary conditions;
2. isolated propeller case to validate the post-processing methodology and the tonal noise computation;
3. drone air-frame and four rotating propellers case to analyze the characteristic of multi-rotor configuration.

The current results are found to be in good agreement with several experimental and numerical observations from literature, including the overall thrust generated, the flow structure, and the tonal noise at the low frequencies. This illustrates the accuracy and usability of the proposed framework for further assessment of multi-rotor noise emissions.

Table of Contents

List of Figures	VI
List of Tables	IX
Acronyms	XI
List of Symbols	XV
1 Introduction	1
1.1 Unmanned Aerial Vehicle	1
1.2 Literature Review	2
1.3 Motivation	4
1.4 Thesis outline	4
2 Tonal noise prediction background theories	6
2.1 Conservation equations in fluid dynamics	6
2.2 Linear acoustic theory	8
2.2.1 Linearization of the equations of fluid mechanics	8
2.2.2 Sound wave equation	9
2.2.3 Green's function methods	10
2.3 Aeroacoustic prediction methods	12
2.4 Aeroacoustic analogies	13
2.4.1 Lighthill's analogy	14
2.4.2 Curle's analogy	17
2.4.3 Ffowcs-Williams and Hawking's analogy	19
2.5 Fan noise	22
2.5.1 Tonal fan noise: fundamental equations	23
2.5.2 Far-field approximation	26
2.5.3 Near-field correction	28
2.5.4 Fixed dipoles array	29

3	Computational fluid dynamics theoretic background	32
3.1	Introduction to turbulence	32
3.2	Numerical methods	33
3.2.1	Direct numerical simulation	35
3.2.2	Reynolds average Navier Stokes equations	35
3.3	RANS turbulence models	37
3.3.1	Zero-order models	37
3.3.2	One-equation models	38
3.3.3	Two-equation models: $k - \varepsilon$ model	40
3.3.4	Two-equation models: $k - \omega$ model	41
4	Numerical setup for computational fluid dynamic simulations	44
4.1	Geometry	44
4.2	Domain	45
4.3	Motion	46
4.3.1	Moving reference frame	47
4.4	Boundary conditions	48
4.5	Physics models and solvers	49
4.5.1	Virtual disk model	50
4.6	Mesh generation	53
4.6.1	Polyhedral and trimmed grid comparison	56
4.7	CFD data extraction	57
4.7.1	Accumulated force tables	58
5	CFD validation and results	60
5.1	Isolated actuator disk	60
5.1.1	Structured-unstructured grid comparison	60
5.1.2	Validation of the virtual disk model for hovering configuration	62
5.2	Isolated propeller	63
5.2.1	Validation and verification of the isolated propeller simulation	63
5.2.2	Flow field of an isolated propeller in hovering configuration	64
5.2.3	Actuator disk and propeller flow field comparison	67
5.3	Drone air-frame and propellers	69
5.3.1	Validation of a full drone configuration in hovering	69
5.3.2	Quadcopter flow field: rotor-on-rotor interactions	70
5.3.3	Quadcopter flow field: rotor-on-body interactions	73
5.4	Conclusion remarks	75
6	Acoustic results	76
6.1	CFD post-processing and preliminary analysis	77
6.1.1	Acoustic analysis input data elaboration	77

6.1.2	Number of the strips convergence study	78
6.1.3	Number of the dipoles convergence study	80
6.2	Validation of the tonal noise computation methodology	83
6.2.1	Isolated propeller case	83
6.2.2	Quadcopter case	86
6.3	Multi-rotors noise field characterization	89
6.3.1	Isolated propeller noise pattern	89
6.3.2	Installation effect of a propeller in a quadcopter configuration	90
7	Conclusions and Future Works	92
7.1	Conclusions	92
7.2	Perspectives	93
A	APC 9x4.5 MR Performance Table	96
	Bibliography	99

List of Figures

1.1	Unmanned Aerial Vehicles examples	2
2.1	A differential control volume in the Cartesian coordinate.	7
2.2	Control volume V , boundary ∂V and outer normal n	11
2.3	CAA procedure.	14
2.4	Source and listener in the analogy of Lighthill.	16
2.5	Body motion trajectory function F characteristics	20
2.6	Source and listener coordinates.	26
2.7	Fan source modeling strategies: single rotating dipole (left) and continuous array of phase shifted dipoles (right).	30
3.1	A schematic overview of turbulence modelling.	34
3.2	$k - \omega$ SST model basic idea representation. Picture modified from [70]	43
4.1	Geometry CAD of cases P and PD	45
4.2	Simulation domains considered for the UAV CFD simulations in this thesis. Left: single-propeller domain (cases P , AD). Right: full-drone domain (case PD).	46
4.3	Simulation motion volume considered for the UAV CFD simulations in this thesis. Left: case P with isolated propeller. Right: case PD with propellers close to drone's surface	46
4.4	Full-drone propellers configurations. Two couple of both clockwise (top and bottom) and counterclockwise (left and right) rotating propellers.	47
4.5	Coordinate system for moving reference frame.	48
4.6	Boundary conditions used in simulations P , AD and PD	49
4.7	Visualization of the actuator disk by the polyhedral cells where the momentum source is added following the body force propeller method.	52
4.8	Comparison of the DJI Phantom 3 propeller and, the APC 9×4.5 MR.	53
4.9	Final surface mesh. Left: details of the propeller surface mesh. Right: details of drone-airframe surface mesh.	55

4.10	Prism layer mesh details. Left: drone arms boundary layer detail. Right: blade section boundary layer detail.	55
4.11	Final meshing scheme used for the fluid domain for cases <i>P</i> and <i>AD</i> . Left: external view. Center: midplane view through rotor plane. Right: topview through rotor plane.	56
4.12	Midplane view through rotor plane of polyhedral mesh (left) and trimmed (right) mesh for case <i>B</i>	57
4.13	Example of blade stripping.	58
5.1	Structured and unstructured mesh schemes for case <i>AD</i> velocity field (top-left) and velocity profile comparison at $z = -40mm$ (1), $z = -800mm$ (2) and $z = -1600mm$ (3).	62
5.2	Comparison of thrust (left) and torque (right) CFD results to experimental data from NASA Ames [71] considering different mesh sizes. The horizontal levels indicate the confidence interval of 95%.	64
5.3	Velocity magnitude plot (a), compared with previous work (b).	65
5.4	Vorticity magnitude plot (a), compared with previous work (b).	65
5.5	Turbulent Kinetic Energy plot.	66
5.6	Full wake development representing by velocity magnitude (a), vorticity magnitude (b) and turbulent kinetic energy (c) plot.	67
5.7	Comparison between the vector contours of case <i>P</i> (left) and <i>PD</i> (right) in different sections downstream.	68
5.8	Thrust time-history comparison between case <i>C</i> and previous works [74].	69
5.9	Comparison of thrust CFD results to empirical data from NASA Ames [71].	70
5.10	Velocity magnitude plot of a multi-rotor configuration.	71
5.11	Vorticity distribution of a multi-rotor configuration: (a) CFD results (b) D. Shukla PIV results [82].	72
5.12	TKE magnitude plot of a multi-rotor configuration.	73
5.13	Full wake development of a full quadcopter configuration represented by velocity magnitude (a) and vorticity magnitude (b) plot.	74
6.1	Case <i>P</i> force post-processing example considering the propeller surface divided in 120 strips. Left: time-history of the axial force of a single strip. Right: Fourier spectrum of the axial force of a single strip.	78
6.2	Diagram of microphone locations considered for the strip convergence study. (Diagram not to scale).	79

6.3	Sound pressure level considering different number of strips at different receiver positions. (a) above the rotor (b) rotation plane (c) below the rotor.	80
6.4	Comparison of the free-field directivities of the isolated propeller in its far-field (a) and near-field (b) at the first BPF. Different number of dipoles are used in the formulation (2.96). Blue dot symbols (solution Eq. (2.82)), black solid line (solution Eq. (2.91)) and red cross symbols (formulation (2.96)).	81
6.5	Comparison of the free-field normalized sound pressure level of the isolated propeller in its far-field (a) and near-field (b) at the first BPF. Different number of dipoles are used in the formulation (2.96).	83
6.6	Diagram of microphone locations considered for the validation of the CFD results against experimental and numerical data [83]. (Diagram not to scale).	84
6.7	Comparison of the sound pressure level at the BPF of the isolated propeller between the CFD results and both numerical and experimental data from literature [83]. Radial position of the listener: 1.2m. Five elevation angle considered: 45°, 77.5°, 90°, 112.5°, 135°.	85
6.8	Comparison of the sound pressure level at the first twenty BPFs of the isolated propeller between the CFD results and both numerical and experimental data from literature [83]. Radial position of the listener: 1.2m. Two elevation angle considered: 90° (top) and 112.5° (bottom).	86
6.9	Diagram of microphone locations considered for the validation of the CFD results against experimental data [14]. (Diagram not to scale).	87
6.10	Comparison of the sound pressure level at the first eleven BPFs of the quadcopter configuration between the CFD results and experimental data from literature [14]. Radial position of the listener: 1.51 m. Elevation angle considered: 130°.	87
6.11	Comparison of the free-field directivities of the quadcopter configuration with numerical results [9]. Receivers at a radial distance of approximately 16R on plane xz	88
6.12	Radiation map in the $\theta = 90^\circ$ (a) and $\theta = 0^\circ$ (b) plane of the full acoustic field radiated by an isolated propeller represented by a circular array of phased dipoles.	89
6.13	Free-field directivities plot in the $\theta = 90^\circ$ (a) plane for the isolated propeller configuration at different blade passing frequencies. (a) BPF (b) 2BPF (c) 3BPF (d) 5BPF.	90
6.14	Radiation map in the $\theta = 90^\circ$ (a) and $\theta = 0^\circ$ (b) plane of the full acoustic field radiated by a quadcopter configuration represented by four circular array of phased dipoles.	91

List of Tables

3.1	Closure coefficients in the standard $k-\varepsilon$ model.	41
4.1	Physics parameters used in the simulations.	50
4.2	Polyhedral mesh control values.	54
4.3	Cell number final mesh schemes.	56
5.1	Structured and unstructured mesh parameters for case AD (see Figure 4.12)	61
5.2	Structured and unstructured mesh T and Q comparison.	61
5.3	Comparison of thrust and torque CFD results of case AD to manufacturer and experimental data [80, 81]	63
5.4	Grid size and predicted thrust.	64
5.5	Comparison of thrust value between isolated propeller (case P) and single propeller of the multi-rotor configuration (case PD).	71
A.1	Performance data of the APC9×4.5MR from [80] considering a rotation rate of $6000rpm$	97

Acronyms

AD Actuator Disk

BEM Blade Element Method

BFPM Body Force Propeller Method

BPF Blade Passing Frequency

BS Base Size

CAA Computational AeroAcoustic

CCW Counterclockwise

CW Clockwise

CFD Computational Fluid Dynamics

DES Detached Eddy Simulation

DNS Direct Numerical Simulation

eVTOL electric Vertical Take-Off and Landing

FFT Fast Fourier Transform

LEE Linearized Euler Equations

LES Large Eddy Simulation

MRF Moving Reference Frame

NVLM Nonlinear Vortex Lattice Method

P Propeller

PD Propeller and Drone

PDE Partial Differential Equation

PSD Power Spectral Density

RANS Reynolds-Averaged Navier–Stokes

RBM Rigid Body Motion

SPL Sound Pressure Level

STOL Short Takeoff and Landing

TKE Turbulent Kinetic Energy

UAM Urban Air Mobility

UAV Unmanned Aerial Vehicle

uRANS unsteady Reynolds-Averaged Navier–Stokes

List of Symbols

Latin letters

B	blade number	
c	speed of sound	$[J]$
D	Doppler factor	
f	force per unit area on body surface	$[Pa]$
e_t	total energy	$[J]$
F_i	point dipole strength	$[N]$
$G(\cdot)$	Green's function	
$H(\cdot)$	Heaviside function	
h	enthalpy	$[J]$
k	specific turbulence kinetic energy	$[J/Kg]$
L	characteristic length	$[m]$
M	Mach number	
M_r	source Mach number	
m	harmonic number	
N	rotor speed	$[rpm]$
\mathbf{n}	surface unit normal	
Pr	Prandtl number	
p	pressure	$[Pa]$

p'	acoustic pressure fluctuation	$[Pa]$
p'_{rms}	sound pressure reference value	$[Pa]$
p'_{BB}	broad-band component of pressure fluctuations	$[Pa]$
p'_{NB}	narrow-band component of pressure fluctuations	$[Pa]$
q	heat flux	$[J/kg]$
\mathbf{R}	source-observer distance	$[m]$
r	receiver radial position	$[m]$
Re	Reynolds number	
S	rigid surface	$[m^2]$
s	entropy	$[J]$
T	temperature	$[K]$
t	time	$[s]$
T_{ij}	Lighthill stress tensor	$[Pa]$
V	control volume	$[m^3]$
v	velocity	$[m/s]$
\mathbf{x}	observer distance	$[m]$
\mathbf{y}	source distance	$[m]$

Greek letters

β	source azimuthal angle	$[^\circ]$
β_{dipo}	azimuthal position of the dipoles	$[^\circ]$
δ	Dirac function	
ε	turbulence dissipation rate	$[J/Kg \cdot s]$
κ	thermal conductivity	$[W/mK]$
λ	wave length	$[m]$
η	source Lagrangian coordinates	

τ	viscous stress tensor	[Pa]
μ	dynamic viscosity	[Pa · s]
ν	kinematic viscosity	[m ² /s]
ν_T	turbulent viscosity	[m ² /s]
Ω	rotating rate	[rpm]
ω	specific turbulence dissipation rate	[1/s]
∂V	control volume boundary	[m ²]
φ	observer azimuthal angle	[°]
φ'	source azimuthal angle at initial instant	[°]
ρ	density	[kg/m ³]
σ_k	Prandtl-Schmidt number	
τ	retarded time	[s]
θ	observer azimuthal angle	[°]

Other Symbols

[·]	evaluation of quantity in brackets at retarded time
[]'	fluctuation of value about mean
[] ₀	mean value
[] _D	drag
[] _R	radial
[] _T	thrust

Chapter 1

Introduction

1.1 Unmanned Aerial Vehicle

Unmanned Aerial Vehicles (UAVs), commonly known as drones (see Figure 1.1), have grown very popular over the last decade. While originally UAVs were designed for military applications, their use has rapidly expanded to the civil market. The unique ability of vertical lift vehicles to hover (flight at a constant altitude) has great potential for human and cargo transportation, delivery systems, inspection and surveillance missions, and disaster relief [1]. For those reasons, the global drone market will grow in the next years [2, 3]. Furthermore, Urban Air Mobility (UAM) is conceived to be the future of transportation in the urban area, since it can potentially aid in avoiding congestion in cities across the globe.

The idea of transferring urban mobility to the air presents many problems. In fact, in order to operate an aircraft in an urban setting, it must be designed with two key constraints in mind: limited space for takeoff and landing, and urban noise regulations [4]. Although the Vertical Takeoff and Landing (VTOL) aircraft (like helicopter or quadcopter) and Short Takeoff and Landing (STOL) aircraft (like an overpowered airplane) be able to take off and land within the space constraints of a city [5], the challenge of noise still exists.

The issue of noise pollution, mainly due to the relatively lower altitude of these vehicles and to the proximity of their routes to extremely densely populated areas, must be taken into account directly during the product conception. The two main contributors to noise generation on a traditional propeller-driven aircraft are related to the combustion engines and the propellers. While the first of these is significantly reduced through the usage of brushless motors [6] rather than traditional combustion engines, the matter regarding propeller noise reduction is far to the conclusion, and it's been in-depth studied in the last few years (see Section 1.2).

Nowadays, the noise theme is one of the main obstacles to widespread public acceptance of flying drones in residential areas [7]. Indeed, it is known that exposure to aircraft noise might be a significant cause of community reaction and social disturbance. Furthermore, several studies indicated that aircraft noise exposure can be associated with a prevalence of psychological and psychiatric symptoms [8].



Figure 1.1: Unmanned Aerial Vehicles examples

1.2 Literature Review

The industries for both recreational-use quadcopters and VTOL urban air taxis have recently seen significant growth. This has been followed by a considerable amount of new challenges related to the aerodynamics and the acoustic of that kind of vehicle. In recent years the interactions related to the multi-rotor configuration have been the subject of many researches. The main focus of these studies is on the rotor-on-rotor interactions [9, 10, 11] and the influence of the airframe [12, 13]. Lee et al. [9] investigated the influence of the spacing between rotor tips on the thrust force for small UAM propellers. They show that the rotor interaction effects increase as the separation distance between the rotor tip decrease. Considered 4 rotors operating in the same plane, the thrust coefficient decreases 7% when varying the tip separation distance from D to $0.2D$.

Similar results were obtained by Intratep et al. [14]. They obtained that the thrust is reduced by 5.8% for 2 rotor operation and 7.3% for the 4 rotor operation in comparison to scaled single rotor performance. From this, we can conclude that the interaction between multiple rotors can decrease aerodynamic performance.

Yoon et al. [10] confirmed the general trends that for a coplanar counter-rotating configuration there was a 4% decrease in the coefficient of thrust as the rotors were brought from a tip separation distance of $2D$ down to $0.1D$. Moreover, when the aircraft body is included in their simulations, there is a less negative interaction between the rotors as the actual aircraft body appeared to be limiting

the downstream interactions of the individual rotors. This would lead to the conclusion that the interactions between rotor wakes are a partial cause of the decrease in thrust.

Thai et al. [12] examined in-depth the aerodynamics of rotor-fuselage interactions. Considering different configurations of the drone DJI Phantom 2, they show that the standard quadrotor case produces a lower value of thrust than the no-fuselage quadrotors case. Again, due to rotor-rotor interactions, neither of the cases were able to reach four times the isolated rotor thrust. Besides, they observed that varying the distance between the rotors and the fuselage produces rotor blade performance lower than the no-fuselage case. The reasoning of that was addressed to the increase of the flow directed upward produced by the fuselage-rotor interactions (called fountain flow), which reduced the performance of the quadrotor.

Yoon et al. [13] focused on the evaluation of the mentioned interactions for small quad-rotor vehicle systems, considering also unconventional configurations. The rotors are placed on the underside of the fuselage arms instead of above. They show that the under-mount configuration generates 1% less total thrust than the overmount. concluding that the under-mount rotors do not offer any improved performance compared to traditional overmount rotors. However, they observed that varying the height of the rotors from the fuselage in under-mount configurations produces significantly more rotor-rotor interactions. Furthermore, the overmount configuration presents strong interactions between the inboard rotor wake and the fuselage wake.

While the aforementioned research suggests that the effects of rotor-rotor and rotor-fuselage interactions on total thrust are minimally significant, the same is not true for their effects on noise.

Zawdony et al. [15] investigated the rotor-airframe interaction noise. The propeller tonal noise changes considerably with the rotor-airframe spacings. The rotor-airframe interaction noise was found to be highly directive as a function of observer azimuth, with the highest amplitudes of which were exhibited by observers located out of the center plane of the airframe. In such a situation, the case of a tip-fuselage distance of 1.2mm presented a level sound increased by approximately 15dB, from the isolate rotor case.

Lee et al. [9] show that the rotor interaction phenomenon significantly increases the sound pressure level (SPL) related to unsteady loading noise, especially along the direction normal to the rotor plane. The insight analysis on the effect of the rotor spacing shows the efficiency of this parameter as a way to relieve the force fluctuation and increased noise level.

The presented literature shows significant effort spent researching the noise generation of single rotors and the aerodynamic effects of rotor-rotor and rotor-fuselage interaction on performance. However, very little research has been done specifically on the effects that the mentioned interactions have on noise generation.

1.3 Motivation

The researches reported in the previous section highlights the lack of in-depth studies on the effects that aerodynamic interactions have on noise generation, and on a feasible way to alleviate it. Moreover, the methods followed by the cited studies require a relevant amount of time and resources. Indeed, the research done on this specific issue considers mainly high-fidelity computational fluid dynamics (CFD) [10], like LES and DES, and experimental methods [16].

This thesis aims to supply a computationally tractable methodology that can predict with a satisfying level of accuracy the tonal noise sound level emitted by multi-rotor configuration. Simplified cases show the integrity of the presented approach through the validation of the aerodynamic and acoustic results.

The presented framework's purpose is to be a starting point for broader works. For example, it can be seen as a fast way to produce the preliminary results for unconventional configurations which have not already been investigated.

1.4 Thesis outline

This first chapter introduced the problems related to multi-rotor drone vehicles, focusing on the current state of research into its complex aerodynamics and aeroacoustics.

The second and the third chapters report the theoretical foundations utilized in the study. The third chapter discusses the acoustic analogy and examines in depth the analytical acoustic derived from the Ffowcs-Williams and Hawkings analogy, needed to estimate the noise generated by propellers. The second chapter regards the numerical formulation of the governing equations for fluid motion and the associated turbulence models used in this research.

The fourth chapter provides the numerical setup implemented in STARCCM+ for the aerodynamic simulations. The description of the CFD setup of the case isolated actuator disk, isolated propeller, and quadcopter is given. The methodology followed for the post-processing of the data is also introduced.

The fifth chapter contains the aerodynamic results. The three simulations are validated against data from precedence works and a qualitative description of the obtained outputs is carried out.

The sixth chapter contains the acoustic results. The outputs from the single propeller and quadcopter simulation are processed to evaluate the tonal noise generated. The validation of the computed sound is reported, and a description of the results is provided.

The final chapter summarizes the obtained results and the validity of the methodology supplied by this thesis. The suggestions for future work are provided based

on the obtained results.

Chapter 2

Tonal noise prediction background theories

In this chapter, the theory implemented for the computation of the noise emitted by a propeller is presented. First of all, the governing equations of motion are discussed in Section 2.1, which are used to evaluate any flow problem. The discussion of the acoustic analogies is reported in Section 2.4, which are introduced by the linear acoustic theory given in Section 2.2. In the end, Section 2.5 shows the three formulations used in this work for the prediction of tonal noise generated by a rotating rotor.

2.1 Conservation equations in fluid dynamics

Fluid flow is governed by the Navier-Stokes equations [17], a coupled set of partial differential equations based on the conservation of mass, momentum, and energy. The three unknowns present in the three basic conservation equations are the three-dimensional velocity \mathbf{v} (with components u_1, u_2, u_3), the pressure p and the absolute temperature T . The final form of the conservation equations also contains four other thermodynamic variables: density ρ , enthalpy h , viscosity μ , and thermal conductivity κ . These four quantities are uniquely determined by the value of p and T .

The fluid flow should be analyzed to know \mathbf{v} , p and T throughout every point of the flow regime. Movement of fluid can be investigated with either Lagrangian or Eulerian methods:

- Lagrangian: take up every point at the beginning of the domain and trace its path until it reaches the end;

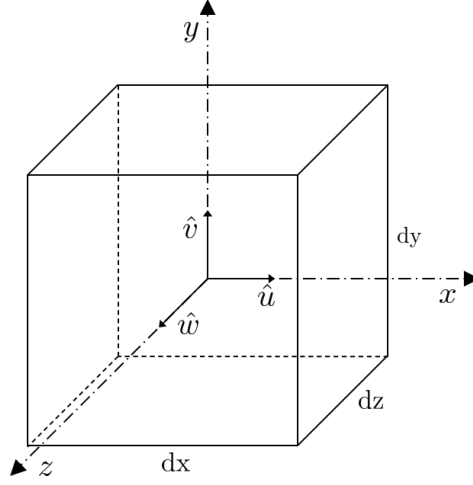


Figure 2.1: A differential control volume in the Cartesian coordinate.

- Eulerian: consider a window (Control Volume) within the fluid and analyze the particle flow within this volume.

Because following millions of separate particles through the path is almost impossible, the three conservation laws are applied to Newtonian fluid (e.g. air) in an Eulerian reference approach. The reference system and the volume are both considered fixed in time and space, as shown in Figure 2.1.

Considering the Einstein convention, for a fluid in motion with a compressible behavior, the conservation equations can be written as:

$$\frac{\partial \rho}{\partial t} + \frac{\partial}{\partial x_j}(\rho u_j) = 0, \quad (2.1)$$

$$\frac{\partial (\rho u_i)}{\partial t} + \frac{\partial}{\partial x_j} [\rho u_i u_j + p \delta_{ij} - \tau_{ij}] = f_i \quad i = 1 \dots 3, \quad (2.2)$$

$$\frac{\partial (\rho e_t)}{\partial t} + \frac{\partial}{\partial x_j} [\rho u_j e_t + p u_j + q_j - u_i \tau_{ij}] = 0, \quad (2.3)$$

where e_t is the total energy, q is the heat flux, τ is the viscous stress term and f is a body force. It should be noted that $p \delta_{ij} - \tau_{ij}$ corresponds to the forces acting on the fluid surface.

In order to close the set of equations, the following relations are considered:

- Newton's constitutive law for viscous stresses:

$$\tau_{ij} = 2\mu S_{ij} - \frac{1}{3} \frac{\partial u_k}{\partial x_k} \delta_{ij}, \quad (2.4)$$

where $S_{ij} = \frac{1}{2} \left(\frac{\partial u_i}{\partial x_j} + \frac{\partial u_j}{\partial x_i} \right)$ is the strain rate tensor.

- Fourier model for heat fluxes:

$$q_j = -\kappa \left(\frac{\partial T}{\partial x_j} \right) \equiv c_p \frac{\mu}{Pr} \frac{\partial T}{\partial x_j}, \quad (2.5)$$

where Pr is the Prandtl number, κ is the thermal conductivity of the gas and μ is the dynamic viscosity.

Substituting (2.4) into (2.2), we find the Navier-Stokes equation of motion:

$$\frac{D(\rho u_i)}{Dt} = -\frac{\partial p}{\partial x_j} + \frac{\partial}{\partial x_j} \left[2\mu S_{ij} - \frac{1}{3} \frac{\partial u_k}{\partial x_k} \delta_{ij} \right] + f_i \quad (2.6)$$

In the end, the Navier Stokes equations contain 6 unknowns: the fields of velocity u_1 , u_2 and u_3 , the pressure p , the temperature T and the density ρ . The additional equation comes from the ideal gas law, which couple the state variables p , ρ and T as:

$$p = \rho R^* T, \quad (2.7)$$

where R^* is the specific gas constant. The PDEs system can be closed through the boundary conditions definition.

2.2 Linear acoustic theory

This section presents the derivation of the governing equation for acoustics and its fundamental solution is obtained starting from the linearization of fluid dynamics equations.

2.2.1 Linearization of the equations of fluid mechanics

The acoustics equations may be derived from the full Navier-Stokes introduced in Section 2.1. However, because most acoustical phenomena involve very small perturbations from steady-state conditions [18], it is possible to make significant simplifications. Considering a uniform ($p_0, \rho_0, \mathbf{v}_0 \dots$) and stagnant ($\mathbf{v}_0 = 0$) fluid, when a disturbance ($p', \rho', \mathbf{v}' \dots$) is present, the field variables could be decomposed into mean values and perturbations around them:

$$p(x_i, t) = p_0 + p'(x_i, t), \quad (2.8)$$

$$\rho(x_i, t) = \rho_0 + \rho'(x_i, t), \quad (2.9)$$

$$v_i(x_i, t) = v_{0,i} + v'(x_i, t) = v'_i(x_i, t). \quad (2.10)$$

Substituting Eqs. (2.8), (2.9) and (2.10) into the conservation equations (2.1) and (2.2), and neglecting second order terms (the so called acoustic approximation), we end to the linear acoustic equations:

$$\frac{\partial \rho'}{\partial t} + \rho_0 \frac{\partial v'_i}{\partial x_i} = Q_m, \quad (2.11)$$

$$\rho_0 \frac{\partial v'_i}{\partial t} + \frac{\partial p'}{\partial x_i} = \frac{\partial \tau'_{ij}}{\partial x_i} + f_i, \quad (2.12)$$

where the source terms Q_m , f_i have been introduced into the conservation equations. To obtain a linear wave propagation, a linearized constitutive equation is formed from the equation of state:

$$p = p(\rho, s), \quad (2.13)$$

where s is the entropy. Applying the chain rule of differentiation:

$$p' = \left(\frac{\partial p}{\partial \rho} \right)_{s=\text{const}} \rho' + \left(\frac{\partial p}{\partial s} \right)_{\rho=\text{const}} s' = c_0^2 \rho' + \left(\frac{\partial p}{\partial s} \right)_{\rho=\text{const}} s', \quad (2.14)$$

where the isentropic speed of sound has been introduced. The subscript 0 indicates that we will now assume a homogeneous propagation medium, with a constant and uniform speed of sound.

2.2.2 Sound wave equation

The wave equation results directly from Eqs. (2.11) and (2.12). Indeed, the acoustic velocity perturbation \mathbf{v}' is eliminated by taking the time derivative of Eq. (2.11), from which we subtract the divergence of Eq. (2.12), giving:

$$\frac{\partial^2 \rho'}{\partial t^2} - \frac{\partial^2 p'}{\partial x_i^2} = -\frac{\partial f_i}{\partial x_i} - \frac{\partial^2 \tau'_{ij}}{\partial x_i^2} + \frac{\partial Q_m}{\partial t} \quad (2.15)$$

Substitution of (2.14) into (2.15) leads to the wave propagation equation for the acoustic pressure perturbation:

$$\frac{1}{c_0^2} \frac{\partial^2 p'}{\partial t^2} - \frac{\partial^2 p'}{\partial x_i^2} = -\frac{\partial f_i}{\partial x_i} - \frac{\partial^2 \tau'_{ij}}{\partial x_i^2} + \frac{1}{c_0^2} \left(\frac{\partial p}{\partial s} \right)_\rho \frac{\partial^2 s'}{\partial t^2} + \frac{\partial Q_m}{\partial t} \quad (2.16)$$

Eq. (2.16) can be rewritten as:

$$\frac{1}{c_0^2} \frac{\partial^2 p'}{\partial t^2} - \frac{\partial^2 p'}{\partial x_i^2} = q \quad (2.17)$$

where has been introduced a shorthand notation for the source term in the wave equation:

$$q(\mathbf{x}, t) = \underbrace{-\frac{\partial f_i}{\partial x_i}}_1 - \underbrace{\frac{\partial^2 \tau'_{ij}}{\partial x_i^2}}_2 + \underbrace{\frac{1}{c_0^2} \left(\frac{\partial p}{\partial s} \right)_\rho \frac{\partial^2 s'}{\partial t^2} + \frac{\partial Q_m}{\partial t}}_3 \quad (2.18)$$

The left-hand side of Eq. 2.17 is the D'Alembertian operator applied to the acoustic pressure perturbation p' , and the right-hand side represents all the possible sources of sound:

1. the term $-\frac{\partial f_i}{\partial x_i}$ represents the effect of a non-uniform body force field, induces dipole like sources;
2. the term $-\frac{\partial^2 \tau'_{ij}}{\partial x_i^2}$ is related to fluctuating viscous stresses, and represents the sound due to the turbulence modeled by quadrupole like sources;
3. the terms $\frac{1}{c_0^2} \left(\frac{\partial p}{\partial s} \right)_\rho \frac{\partial^2 s'}{\partial t^2}$ and $\frac{\partial Q_m}{\partial t}$, both represents a volume source, thus they are both expressed by monopole like source.

2.2.3 Green's function methods

Green's function [18, 19] formalism is useful to obtain an integral solution of the wave propagation equation (2.17) accounting for the effects of the sources, boundary conditions, and initial conditions. The Green's function is defined as the solution of the following inhomogeneous wave equation:

$$\frac{\partial^2 G}{\partial t^2} - c_0^2 \nabla^2 G = \delta(\mathbf{x} - \mathbf{y}) \delta(t - \tau) \quad (2.19)$$

where the right-hand side is the product of two Kronecker delta functions, where \mathbf{x} and t are the listener position and time, and \mathbf{y} is the position of an impulsive source emitting a pulse at the time τ ($\tau > t$). Boundary conditions must be provided to solve Eq. (2.19), determining the type of Green's function.

In free-field conditions, the appropriate boundary condition is the Sommerfeld's condition:

$$\lim_{r \rightarrow \infty} r \left(\frac{\partial G}{\partial t} + c_0 \frac{\partial G}{\partial r} \right) = 0 \quad (2.20)$$

The corresponding solution, noted G_0 , is:

$$G_0(\mathbf{x}, t | \mathbf{y}, \tau) = \frac{\delta \left(t - \tau - \frac{|\mathbf{x} - \mathbf{y}|}{c_0} \right)}{4\pi c_0^2 |\mathbf{x} - \mathbf{y}|} = \frac{\delta(\tau^* - \tau)}{4\pi c_0^2 |\mathbf{x} - \mathbf{y}|} \quad (2.21)$$

where:

$$\tau^* = t - |\mathbf{x} - \mathbf{y}|/c_0 \quad (2.22)$$

is the retarded time at which the source field must be known at the position \mathbf{y} in order to calculate the sound field at the listener position \mathbf{x} at the time t .

The main purpose of a Green's function consists in finding solutions of the wave propagation equation with a generic source term $q(\mathbf{x}, t)$. Combining Eq. (2.17) multiplied by G , with the equation (2.19) itself multiplied by the unknown pressure perturbation p' , and integrating the difference of these equations over a control volume V and times from an arbitrary time t_0 to the listener time t , yields:

$$\begin{aligned}
 p'(\mathbf{x}, t) = & \int_{t_0}^t \iiint_V q(\mathbf{y}, t) G_0(\mathbf{x}, t | \mathbf{y}, \tau) d^3 \mathbf{y} d\tau \\
 & + \int_{t_0}^t \iiint_V \left(p'(\mathbf{y}, t) \frac{\partial^2 G}{\partial \tau^2} - G \frac{\partial^2 p'(\mathbf{y}, t)}{\partial \tau^2} \right) d^3 \mathbf{y} d\tau \\
 & - \int_{t_0}^t \iiint_V \left(p'(\mathbf{y}, t) \frac{\partial^2 G}{\partial y_i^2} - G \frac{\partial^2 p'(\mathbf{y}, t)}{\partial y_i^2} \right) d^3 \mathbf{y} d\tau \quad (2.23)
 \end{aligned}$$

The second and third integrals of Eq. (2.23) can be integrated by parts with respect to time and space respectively, to yield (with the normal direction defined in Figure 2.2):

$$\begin{aligned}
 p'(\mathbf{x}, t) = & \int_{t_0}^t \iiint_V q(\mathbf{y}, t) G_0(\mathbf{x}, t | \mathbf{y}, \tau) d^3 \mathbf{y} d\tau \\
 & - \left[\iiint_V \left(p'(\mathbf{y}, t) \frac{\partial G}{\partial \tau} - G \frac{\partial p'(\mathbf{y}, t)}{\partial \tau} \right) d^3 \mathbf{y} \right]_{\tau=t_0}^{\tau=t} \\
 & - \int_{t_0}^t \iint_{\partial V} \left(p'(\mathbf{y}, t) \frac{\partial G}{\partial y_i} - G \frac{\partial p'(\mathbf{y}, t)}{\partial y_i} \right) n_i d^2 \mathbf{y} d\tau \quad (2.24)
 \end{aligned}$$

The contribution of the second integral in Eq. (2.24) can be brought to zero by virtue of causality and by choosing silent initial conditions. The third integral represents the contribution of the boundaries of the control volume.

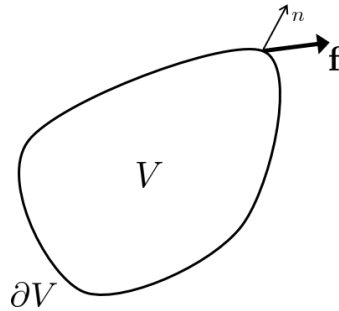


Figure 2.2: Control volume V , boundary ∂V and outer normal n .

In absence of a solid body in the propagation domain, the only boundary is the one at infinity, where the Green's function and/or source vanishes, giving a null contribution. If a solid body is present, it will from now on be assumed that the control volume boundary coincides with the surface of a solid body. In such a case, considering a fixed body, Eq. (2.24) becomes:

$$p'(\mathbf{x}, t) = \int_{t_0}^t \iiint_V q(\mathbf{y}, \tau) G_0(\mathbf{x}, t | \mathbf{y}, \tau) d^3\mathbf{y} d\tau - \int_{t_0}^t \iint_{\partial V} p'(\mathbf{y}, \tau) \frac{\partial G}{\partial y_i} n_i d^2\mathbf{y} d\tau \quad (2.25)$$

where the surface integral represents the scattering of the incident field on the domain boundary. It makes Eq. (2.25) implicit since the sound field at the listener depends on the acoustic reflections over the surfaces. The dependence of the solution on the arbitrary shapes of the bounding surface leads to difficulties in solving Eq. (2.25). However, there are a number of instances in which solutions of Eq. (2.25) can be relatively easily obtained. Indeed, instead of using the free-field Green's function G_0 , can be adopted the tailored Green's function G_t , which satisfies Eq. (2.19) and the condition $\partial G / \partial n$ over the boundary S . In that case, the surface integral vanishes, yielding an explicit integral solution for the acoustic density perturbation:

$$p'(\mathbf{x}, t) = \int_{t_0}^t \iiint_V q(\mathbf{y}, \tau) G_t(\mathbf{x}, t | \mathbf{y}, \tau) d^3\mathbf{y} d\tau \quad (2.26)$$

The geometrical configurations for which such tailored Green's functions can be found are unfortunately not numerous.

2.3 Aeroacoustic prediction methods

The numerical approach to evaluate the aerodynamic sound is called Computational AeroAcoustics (CAA) [20, 21], that is defined in the broadest sense, regrouping all methods involving numerical computations to produce acoustical information for aerodynamic phenomena (see Figure 3.1).

All the aeroacoustic mechanisms involved (source generation, acoustic propagation, refraction, and scattering) could be theoretically simulated by solving the Navier–Stokes equations on a domain extending from the source region to the receiver position, which could be placed far from the source, extending the size of the computational domain and so the computational time required. Most of the aeroacoustic problems associated with industries involve fluid flow at low Mach numbers, which means the presence of a scale disparity between the hydrodynamic and the acoustic waves. Therefore, a higher-order scheme is employed to capture the acoustics and the flow at the same time. Hence, Direct Numerical Simulation

(DNS), which resolves all flow scales including small dissipative scales, or Large-Eddy simulation (LES), which resolves only the dynamically important flow scales and models the effect of smaller scales, can be employed. Unsteady Reynolds-Averaged Navier-Stokes (URANS) computations or Detached-Eddy simulations (DES) can also be used if only large flow structures are considered.

Evaluating the flow and sound fields altogether, CAA techniques called direct methods, requires large computing resources and can only be achieved for academic cases. For more realistic cases, it is often necessary to partition the problem and simulate it separately. Hybrid methods decouple the computation of the flow from the computation of the sound, and consist of a two steps procedure:

1. firstly, near the noise source, the flow field is obtained from the computation of the more energetic contents of the turbulent flow;
2. secondly, the acoustic source radiation is computed in the far-field using an acoustic propagation method.

The main assumption of such a hybrid method is the one-way coupling of the flow and sound. In other words, the effects that the flow can have on the acoustic propagation (such as convection or refraction) will be properly taken into account, but not the contrary. However, this restriction is weakly limiting since such feedback only occurs in special situations [22].

On the acoustic propagation side, different techniques can be used. The acoustic information from the sources can be obtained at the receiver position using computational or analytical transport methods [23]. Usually, computational methods solve Linearized Euler Equations (LEE) or transport equations concentrating only on acoustic propagation, instead of direct methods which consider also the aerodynamic flow field. The analytical transport methods are related to acoustic analogies [24, 25, 26] and Kirchhoff integrals [27]. The first method is based on the substitution of the real flow by equivalent sources, computed as a post-processing of the flow data. The second one employs an analytical solution of the wave equation using Kirchhoff integral provided that a wave equation is satisfied at the edge of the simulation domain.

In this thesis only the analytical transport methods related to acoustic analogies are analyzed in more detail.

2.4 Aeroacoustic analogies

An aeroacoustic analogy is a reformulation of the fluid dynamics equations that allows distinguishing the sound generation mechanisms from the sound propagation. Indeed, considering the sound field as a small perturbation of the flow allows

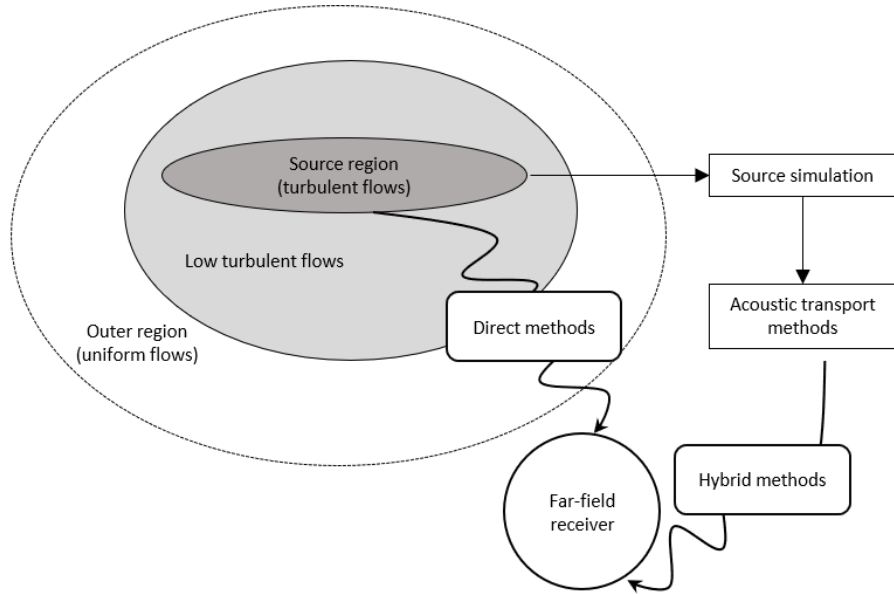


Figure 2.3: CAA procedure.

rearranging the Navier-Stokes equations into various forms of the inhomogeneous acoustic wave equation.

The part of the flow in which sound production is expected is called the source region. The part of the flow in which the listener is standing defines the reference flow. The difference between the actual flow and an extrapolation of the reference flow into the source region is identified as the source of the sound. This idea was introduced by Lighthill [24] who calls this an analogy.

In some cases, the distinction between sound production and sound propagation mechanisms can be delicate. These aspects can even become coupled when aeroacoustic resonances occur. One has then to resort to CFD accuracy to capture the coupling phenomenon. This imposes severe accuracy requirements for the compressible numerical simulation that must be used in order to capture the acoustic propagation and feedback on the source mechanism. The flow-acoustic resonances are not considered in this thesis, where it is assumed that the sound emitted by the low Mach number flow does not perturb the flow.

2.4.1 Lighthill's analogy

In the 1950s, Lighthill [24] first addressed the problem of turbulence and jet noise. His work is usually referred to as the starting point of most of the aeroacoustic analogies.

Lighthill's analogy is derived from the exact Navier-Stokes equations. We take the

time derivative of the mass equation (2.1) and subtract from this the divergence of the momentum equation (2.2) to obtain:

$$\frac{\partial^2 \rho}{\partial t^2} = \frac{\partial^2 (\rho v_i v_j - \tau_{ij})}{\partial x_i \partial x_j} + \frac{\partial^2 p}{\partial x_i^2} - \frac{\partial f_i}{\partial x_i} \quad (2.27)$$

We can subtract on both sides of this equation a term $c_0^2 (\partial^2 \rho / \partial x_i^2)$. This provides an equation in which the left hand side is the wave propagation operator of d'Alembert:

$$\frac{\partial^2 \rho}{\partial t^2} - c_0^2 \frac{\partial^2 \rho}{\partial x_i^2} = \frac{\partial^2 (\rho v_i v_j - \tau_{ij})}{\partial x_i \partial x_j} + \frac{\partial^2 (p - c_0^2 \rho)}{\partial x_i^2} - \frac{\partial f_i}{\partial x_i} \quad (2.28)$$

In order to proceed, the key idea is to follow the same procedure used to obtain Eq. (2.16) to form a D'Alembertian. That means the distinction of a quiescent and uniform reference fluid state in which happens the acoustical propagation. It should be noted that these conditions (ρ_0, p_0) were introduced in Eqs. (2.8), (2.9) and (2.10) to linearize the governing equations, but they are used here to define a reference uniform and stagnant propagation medium surrounding the jet flow, where the acoustic waves are by definition propagating at the constant speed c_0 . Note that these definitions do not restrict in any way the generality of the equation that will follow, known as Lighthill's analogy:

$$\frac{\partial^2 \rho'}{\partial t^2} - c_0^2 \frac{\partial^2 \rho'}{\partial x_i^2} = \frac{\partial^2 T_{ij}}{\partial x_i \partial x_j} - \frac{\partial f_i}{\partial x_i} \quad (2.29)$$

where T_{ij} is the Lighthill stress tensor defined as:

$$T_{ij} = \rho v_i v_j + (p' - c_0^2 \rho') \delta_{ij} - \tau_{ij} \quad (2.30)$$

It should be noted that there has been no approximation nor linearization, i.e. all non-linearities of the flow field are still included in the right-hand side of Eq. (2.29). Therefore, Eq. (2.29) involves all the unknowns of the original Navier-Stokes equations, and is generally not easier to solve than the latter. It provides however a powerful formalism to introduce quite useful approximations in the description of the source field.

We have seen in Section 2.2.3 how to solve the inhomogeneous wave propagation equation using a Green's function. Adopting the same arguments about causality and initial silent boundary conditions, we end up with a very similar equation:

$$\rho'(\mathbf{x}, t) = \int_{-\infty}^t \iiint_V \frac{\partial^2 T_{ij}}{\partial y_i \partial y_j} G d^3 \mathbf{y} d\tau - c_0^2 \int_{-\infty}^t \iint_{\partial V} \left(\rho' \frac{\partial G}{\partial y_i} - G \frac{\partial \rho'}{\partial y_i} \right) n_i d^2 \mathbf{y} d\tau \quad (2.31)$$

where the first integral represents the incident sound field due to the aerodynamic sources distributed in the fluid volume V , and the second integral represents the

scattering over the boundaries ∂V of this volume and possible vibration of a solid surface bounding the volume. In absence of solid bodies, the only contribution from the boundary is from its portion at infinity, leading to the neglecting of the surface integral. In presence of solid bodies, the contribution of the scattering part of the integral can also be brought to zero by finding a suitable tailored Green's function such as $\partial G/\partial n = 0$ on ∂V , as explained in Section 2.2.3.

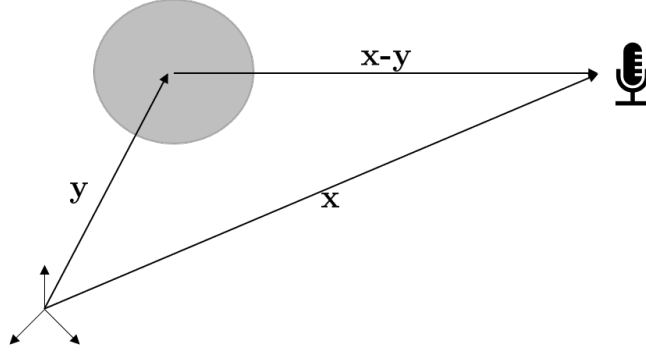


Figure 2.4: Source and listener in the analogy of Lighthill.

The integral solution of Eq. (2.29) is obtained by the introduction of classical approximation used for this type of problems:

- the acoustic far-field is defined when the observer distance from the closest point in the source region exceeds the acoustic wavelength: $d/\lambda \gg 1$;
- the geometric far-field is defined when the observer location is large compared to the size of the source region: $d/L_s \gg 1$;
- a source or source region is considered acoustically compact when its size is much smaller than the acoustic wavelength: $l/\lambda \ll 1$ or $L_s/\lambda \ll 1$ respectively;

where has been considered a source region of size L_s , containing individual sources of size l , (the corresponding wavelength is given by $\lambda = l/M$, where M is the Mach number) and an observer located at a distance d from the source.

We assume that no solid boundaries are present inside the domain (no external forces f_i are exerted in the reference quiescent flow region), and consider the case of an unbounded domain, so free-field Green's function can be used. Furthermore, if the receiver is placed in the geometric and acoustic far-field of a compact source region, Lighthill's integral solution can be written as:

$$\rho'(\mathbf{x}, t) \approx \frac{x_i x_j}{4\pi c_0^4 |\mathbf{x}|^3} \int_V \frac{\partial^2}{\partial t^2} \left[T_{ij} \left(\mathbf{y}, t - \frac{|\mathbf{x}|}{c_0} \right) \right] dV \quad (2.32)$$

Eq. (2.32) is the fundamental result of Lighthill's analogy. Indeed, from this equation, the well-known 8-th power law of Lighthill can be obtained, indicating that the sound power of a jet increases with the eighth power of the velocity [28].

2.4.2 Curle's analogy

Curle [25] extended Lighthill's results for the sound generated by unsteady flows interacting with steady surfaces. Indeed, the flow volume boundary ∂V in (2.31) includes the surface of the solid body, and if we use the free field Green's function G_0 as before, the surface integral will yield the implicit scattering of the volume source over the body surface.

Considering the solid boundaries inside the domain, performing the double integration by parts of the volume source in (2.31), we obtain the following expression:

$$\begin{aligned} \rho'(\mathbf{x}, t) &= \int_{-\infty}^t \iiint_V T_{ij} \frac{\partial^2 G}{\partial y_i \partial y_j} d^3 \mathbf{y} d\tau \\ &\quad + \int_{-\infty}^t \iint_{\partial V} \left(\frac{\partial T_{ij}}{\partial y_i} G n_j - T_{ij} \frac{\partial G}{\partial y_j} \right) d^2 \mathbf{y} d\tau \\ &\quad - c_0^2 \int_{-\infty}^t \iint_{\partial V} \left(\rho' \frac{\partial G}{\partial y_i} - G \frac{\partial \rho'}{\partial y_i} \right) n_i d^2 \mathbf{y} d\tau \end{aligned} \quad (2.33)$$

Since T_{ij} is a symmetrical tensor, we have $(\partial T_{ij} / \partial y_i) n_j = (\partial T_{ij} / \partial y_j) n_i$ and using the conservation of momentum (2.2)(8) in absence of external forces, we find:

$$\begin{aligned} \frac{\partial T_{ij}}{\partial y_j} &= \frac{\partial}{\partial y_j} \left(\rho v_i v_j + (p' - c_0^2 \rho') \delta_{ij} - \sigma_{ij} \right) \\ &= -\frac{\partial \rho v_i}{\partial \tau} - c_0^2 \frac{\partial \rho'}{\partial y_i} \end{aligned} \quad (2.34)$$

Introducing the expression of the source tensor T_{ij} in (2.33), we obtain therefore:

$$\begin{aligned} \rho'(\mathbf{x}, t) &= \int_{-\infty}^t \iiint_V T_{ij} \frac{\partial^2 G}{\partial y_i \partial y_j} d^3 \mathbf{y} d\tau \\ &\quad + \int_{-\infty}^t \iint_{\partial V} \left\{ \left(-\frac{\partial \rho v_i}{\partial \tau} - c_0^2 \frac{\partial \rho'}{\partial y_i} \right) G - (\rho v_i v_j + (p' - c_0^2 \rho') \delta_{ij} - \sigma_{ij}) \frac{\partial G}{\partial y_j} \right\} d^2 \mathbf{y} d\tau \\ &\quad - c_0^2 \int_{-\infty}^t \iint_{\partial V} \left(\rho' \frac{\partial G}{\partial y_i} - G \frac{\partial \rho'}{\partial y_i} \right) n_i d^2 \mathbf{y} d\tau \end{aligned} \quad (2.35)$$

and we see that the scattering terms corresponding to the second integral cancel

out with the density perturbation terms coming from Lighthill's tensor. We obtain:

$$\begin{aligned} \rho'(\mathbf{x}, t) = & \int_{-\infty}^t \iiint_V T_{ij} \frac{\partial^2 G}{\partial y_i \partial y_j} d^3 \mathbf{y} d\tau \\ & - \int_{-\infty}^t \iint_{\partial V} \left(\frac{\partial \rho v_i}{\partial \tau} G + (\rho v_i v_j + p' \delta_{ij} - \sigma_{ij}) \frac{\partial G}{\partial y_j} \right) d^2 \mathbf{y} d\tau \end{aligned} \quad (2.36)$$

where the first term in the second integral can be integrated by parts (assuming the normal n_i does not vary in time):

$$\int_{-\infty}^t \iint_{\partial V} \frac{\partial \rho v_i}{\partial \tau} G d^2 \mathbf{y} d\tau = \iint_{\partial V} [\rho v_i n_i G]_{-\infty}^t d^2 \mathbf{y} - \int_{-\infty}^t \iint_{\partial V} \rho v_i n_i \frac{\partial G}{\partial y_j} d^2 \mathbf{y} d\tau \quad (2.37)$$

The first integral vanishes either as before by virtue of causality, or simply because the surface or the solid body is here assumed steady and impermeable, thereby canceling the contribution of the second integral as well. We obtain:

$$\rho'(\mathbf{x}, t) = \int_{-\infty}^t \iiint_V T_{ij} \frac{\partial^2 G}{\partial y_i \partial y_j} d^3 \mathbf{y} d\tau - \int_{-\infty}^t \iint_{\partial V} (p' \delta_{ij} - \sigma_{ij}) \frac{\partial G}{\partial y_j} d^2 \mathbf{y} d\tau \quad (2.38)$$

Note that the above derivations are valid irrespectively of the Green's function is free field or tailored. Choosing a free field Green's function G_0 with space and time reciprocity properties and using the far-field approximation:

$$\frac{\partial}{\partial x_i} \approx -\frac{x_i}{c_0 |\mathbf{x}|} \frac{\partial}{\partial t} \quad (2.39)$$

allows finding:

$$\begin{aligned} \rho'(\mathbf{x}, t) = & \frac{x_i x_j}{4\pi |\mathbf{x}|^2 c_0^4} \iiint_V \frac{\partial^2}{\partial t^2} \left[\frac{T_{ij}}{|\mathbf{x} - \mathbf{y}|} \right] d^3 \mathbf{y} - \frac{1}{4\pi c_0^2} \iint_{\partial V} \frac{\partial}{\partial t} \left[\frac{\rho v_i n_i}{|\mathbf{x} - \mathbf{y}|} \right] d^2 \mathbf{y} \\ & + \frac{x_i}{4\pi |\mathbf{x}| c_0^3} \iint_{\partial V} \frac{\partial}{\partial t} \left[\frac{(\rho v_i v_j + p' \delta_{ij} - \sigma_{ij}) n_j}{|\mathbf{x} - \mathbf{y}|} \right] d^2 \mathbf{y} \end{aligned} \quad (2.40)$$

where n_j are the components of the outward pointing (into the fluid volume V) unit normal of the surface S . Notice that the bracketed terms are to be evaluated at the retarded time (2.22).

For a steady, nonpenetrable surface, and assuming a low Mach number and isentropic flow in the source region, the same approximations as above yield:

$$\begin{aligned} \rho'(\mathbf{x}, t) \approx & \frac{x_i x_j}{4\pi |\mathbf{x}|^3 c_0^4} \iiint_V \frac{\partial^2}{\partial t^2} \left[T_{ij} \left(\mathbf{y}, t - \frac{|\mathbf{x}|}{c_0} \right) \right] dV \\ & + \frac{x_i}{4\pi |\mathbf{x}|^2 c_0^3} \iint_S \frac{\partial}{\partial t} \left[p_{ij} n_j \left(\mathbf{y}, t - \frac{|\mathbf{x}|}{c_0} \right) \right] dS \end{aligned} \quad (2.41)$$

where $p_{ij} = p'\delta_{ij} - \sigma_{ij}$ is the stress tensor including the pressure and viscous stress contributions.

Eq. (2.41) is the fundamental result of Curle's analogy. In it, the surface integral, representing the modification to Lighthill's theory, is exactly equivalent to the sound generated in a medium at rest by a distribution of dipoles of strength $F_i = p_{ij}$ per unit area, and, F_i is exactly the force per unit area exerted on the fluid by the solid boundaries in the x_i direction. Physically, therefore, one can look upon the sound field as the sum generated by a volume distribution of quadrupoles and by a surface distribution of dipoles.

It is important to notice that, just as in Lighthill's theory, the analysis is exact and no simplifying assumptions have been made regarding the relationship between stresses and rates of strain.

2.4.3 Ffowcs-Williams and Hawking's analogy

Ffowcs-Williams and Hawkings [26] extended Lighthill and Curle's theory for the aerodynamic sound to include arbitrary convective motion. Indeed, Ffowcs-Williams and Hawking's analogy introduces the effect of motion of the surfaces present inside the domain. Those surfaces can be set as surfaces of a solid body (impermeable) or as any free surface located in the domain (permeable). In other words, in contradiction to Curle's analogy, Ffowcs-Williams and Hawking's analogy allows the motion of the bodies inside the fluid domain.

To account the motion of the surface Ffowcs-Williams and Hawking considered the setting up of a generalized function. In this section, the discussion will be restricted to the case of a rigid surface S . Assuming that the body motion trajectory is described by a function $F(x, y, z, t)$, which is equal to zero on the surface of the bodies, negative inside the solid bodies, and positive in the fluid regions (figure 2.5). Hence, the generalized function is formed with the aid of Heavyside's unit function $H(F)$, defined to be unity where $F > 0$ and zero where $F < 0$. That means that the generalized function equals the required function in the relevant region, and is zero elsewhere.

In order to proceed, the conservation Eqs. (2.1), (2.2) can be rewritten using the generalized function:

$$\frac{\partial(\rho'H)}{\partial t} + \frac{\partial(\rho'v_iH)}{\partial x_i} = \rho_0(\mathbf{v} \cdot \nabla F)\delta(F) = \rho_0V_n\delta(F), \quad (2.42)$$

$$\frac{\partial(\rho'v_iH)}{\partial t} + \frac{\partial}{\partial x_j} [(\rho'v_iv_j + p'\delta_{ij} + \sigma_{ij})H] = (p'\delta_{ij} + \sigma_{ij})\nabla F\delta(F) \quad (2.43)$$

Following Lighthill's methodology, we combine the time derivative of (2.42) with

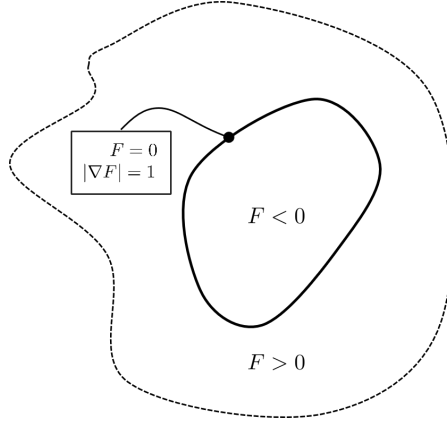


Figure 2.5: Body motion trajectory function F characteristics

the divergence of (2.43) to:

$$\frac{\partial^2(\rho'H)}{\partial t^2} - c_0^2 \frac{\partial^2(\rho'v_i H)}{\partial x_i^2} = \frac{\partial^2}{\partial x_i \partial x_j} (T_{ij}H) - \frac{\partial}{\partial x_i} [(p'\delta_{ij} + \sigma_{ij})\nabla F \delta(F)] + \frac{\partial}{\partial t} (\rho_0 V_n \delta(F)) \quad (2.44)$$

Ffowcs-Williams and Hawking's equation (2.44) can be written as:

$$\begin{aligned} \rho'(\mathbf{x}, t) = & \frac{\partial^2}{\partial x_i \partial x_j} \int_{-\infty}^t \iiint_V \frac{\partial^2 G}{\partial y_i \partial y_j} T_{ij}(\mathbf{y}, \tau) d^3 \mathbf{y} d\tau \\ & - \frac{\partial}{\partial x_i} \int_{-\infty}^t \iint_{\partial V} \frac{\partial G}{\partial y_i} f_i(\mathbf{y}, \tau) n_j d^2 \mathbf{y} d\tau \\ & + \frac{\partial}{\partial t} \int_{-\infty}^t \iint_{\partial V} \frac{\partial G}{\partial \tau} \rho_0 V_n(\mathbf{y}, \tau) d^2 \mathbf{y} d\tau \end{aligned} \quad (2.45)$$

where f is the force per unit area exerted by the surface on the fluid. Adopting again the free-field Green's function, Eq. (2.45) becomes:

$$\begin{aligned} \rho'(\mathbf{x}, t) = & \frac{\partial^2}{\partial x_i \partial x_j} \int_{-\infty}^t \iiint_V \frac{\delta(t - \tau - |\mathbf{x} - \mathbf{y}|/c_0)}{4\pi c_0^2 |\mathbf{x} - \mathbf{y}|} T_{ij}(\mathbf{y}, \tau) d^3 \mathbf{y} d\tau \\ & - \frac{\partial}{\partial x_i} \int_{-\infty}^t \iint_{\partial V} \frac{\delta(t - \tau - |\mathbf{x} - \mathbf{y}|/c_0)}{4\pi c_0^2 |\mathbf{x} - \mathbf{y}|} f_i(\mathbf{y}, \tau) n_j d^2 \mathbf{y} d\tau \\ & + \frac{\partial}{\partial t} \int_{-\infty}^t \iint_{\partial V} \frac{\delta(t - \tau - |\mathbf{x} - \mathbf{y}|/c_0)}{4\pi c_0^2 |\mathbf{x} - \mathbf{y}|} \rho_0 V_n(\mathbf{y}, \tau) d^2 \mathbf{y} d\tau \end{aligned} \quad (2.46)$$

To carry out the integration over τ , it is convenient to introduce Lagrangian coordinates η , which are fixed to the source. The relation between the Lagrangian

coordinates and the fixed system is given by the equation:

$$\mathbf{y} = \boldsymbol{\eta} + \int^t c\mathbf{M}(\boldsymbol{\eta}, t)dt \quad (2.47)$$

where the source convection velocity is written as the product of the Mach number $\mathbf{M} = \mathbf{V}/c_0$ and the sound velocity c_0 .

Rewriting Eq. (2.46) considering the coordinates transformation in Eq. (2.47) yields:

$$\begin{aligned} \rho'(\mathbf{x}, t) = & \frac{\partial^2}{\partial x_i \partial x_j} \int_{-\infty}^t \iiint_{V_\eta} \frac{\delta(g(\tau, t, \mathbf{x}, \boldsymbol{\eta}))}{4\pi c_0^2 |\mathbf{x} - \mathbf{y}(\boldsymbol{\eta}, \tau)|} T_{ij} d^3 \boldsymbol{\eta} d\tau \\ & - \frac{\partial}{\partial x_i} \int_{-\infty}^t \iint_{\partial V_\eta} \frac{\delta(g(\tau, t, \mathbf{x}, \boldsymbol{\eta}))}{4\pi c_0^2 |\mathbf{x} - \mathbf{y}(\boldsymbol{\eta}, \tau)|} f_i n_j d^2 \boldsymbol{\eta} d\tau \\ & + \frac{\partial}{\partial t} \int_{-\infty}^t \iint_{\partial V_\eta} \frac{\delta(g(\tau, t, \mathbf{x}, \boldsymbol{\eta}))}{4\pi c_0^2 |\mathbf{x} - \mathbf{y}(\boldsymbol{\eta}, \tau)|} \rho_0 V_n d^2 \boldsymbol{\eta} d\tau \end{aligned} \quad (2.48)$$

where the function $g(\tau, t, \mathbf{x}, \boldsymbol{\eta})$ permit to compute the retarded time t^* , indeed $\delta(g) = 0$ when $g = 0$, and this occurs only when $\tau = t^*$. For what has been said the retarded time equation is defined as:

$$g(t^*, t, \mathbf{x}, \boldsymbol{\eta}) \equiv t - t^* + \frac{|\mathbf{x} - \mathbf{y}(\boldsymbol{\eta}, t^*)|}{c_0} = 0 \quad (2.49)$$

To carry out the integration with respect to τ , the following Dirac function property must be considered:

$$\int_{-\infty}^{\infty} \delta(h(\xi)) f(\xi) d\xi = \sum_i \frac{f(\xi_i)}{|h'(\xi_i)|} \quad (2.50)$$

valid when $h(\xi) = 0$. Therefore to apply Eq. (2.50) to Eq. (2.49) must be evaluated:

$$\left(\frac{\partial g}{\partial \tau} \right)_\eta = 1 - \frac{\mathbf{R}}{c_0 R} \cdot \left(\frac{\partial \mathbf{y}}{\partial \tau} \right)_\eta = 1 - \frac{\mathbf{R}}{R} \cdot \mathbf{M} \quad (2.51)$$

where $R = |\mathbf{x} - \mathbf{y}|$ is the distance from the source point \mathbf{y} to the field point \mathbf{x} .

We can now use the property described in Eq. (2.50), this lead to the Ffwocs-Williams and Hawking equation:

$$\begin{aligned} \rho'(\mathbf{x}, t) = & \frac{1}{4\pi c_0^2} \frac{\partial^2}{\partial x_i \partial x_j} \iiint_{V_\eta} \left[\frac{T_{ij}}{R|1 - \mathbf{M} \cdot \mathbf{R}/R|} \right] d^3 \boldsymbol{\eta} \\ & - \frac{1}{4\pi c_0^2} \frac{\partial}{\partial x_i} \iint_{\partial V_\eta} \left[\frac{f_i n_j}{R|1 - \mathbf{M} \cdot \mathbf{R}/R|} \right] d^2 \boldsymbol{\eta} \\ & + - \frac{1}{4\pi c_0^2} \frac{\partial}{\partial t} \iint_{\partial V_\eta} \left[\frac{\rho_0 V_n}{R|1 - \mathbf{M} \cdot \mathbf{R}/R|} \right] d^2 \boldsymbol{\eta} \end{aligned} \quad (2.52)$$

where the bracketed expression is to be evaluated at the retarded time τ^* . Set $M_r = \mathbf{M} \cdot \mathbf{R}/R$, the factor $|1 - M_r|^{-1}$ is called Doppler factor, which take into account the effect of the source convection. Indeed, in the sources fixed coordinate system, the Doppler effects consider all convective amplification and frequency shift effect. It's clear that any estimation of the radiated sound based on this equation clearly runs into serious difficulties whenever the factor $|1 - M_r|^{-1}$ vanishes. Eq. (2.52) shows that in general sound can be regarded as generated by three source distributions:

- distribution of acoustic quadrupoles of strength density T_{ij} distributed throughout the region exterior to the surfaces;
- surface distributions of acoustic dipoles of strength density $F_i = f_i n_j$;
- surface distributions of sources essentially monopole in character representing a volume displacement effect.

2.5 Fan noise

The aerodynamic noise of conventional propellers, following a largely accepted classification, is due mainly to two different components: tonal and broad-band contributions [29, 30]. The first one is directly related to the periodic motion of the blade in the surrounding fluid. The physical mechanism which gives the harmonic noise is related to the blade thickness and its surface aerodynamic loading. An additional non-linear contribution can be present and is represented as a quadrupole source. When the tonal noise is considered, a parameter that coupled the frequency of the radiated noise to the rotational velocity is usually considered. The blade passing frequency is given as:

$$BPF = \frac{B\Omega}{60} \quad (2.53)$$

where B is the number of blades, Ω is the rotation rate (measured in rpm). On the other hand, broad-band noise, instead of presenting a discrete frequency spectrum, has a continuous behavior in the frequency domain. Broad-band noise is associated with the random distribution of forces over the surfaces of the blades, which could be caused by the turbulence in the flow or also self-induced when the evolving turbulent boundary layer interacts with the trailing edge of the blade itself. In conclusion, the broad-band contributions are typically induced by lateral flight and by recirculations inherent to the operational regimes.

Research studies tend to separate pressure fluctuations radiated from the blade surface in the far-field, into two components: [31, 29]

$$p' = p'_{NB} + p'_{BB} \quad (2.54)$$

where p'_{NB} is the narrow-band component of pressure fluctuations, and where p'_{BB} is the broad-band counterpart.

In this thesis only the tonal component is considered. We used Roger's formulation of rotor noise model [32, 33] based on the reformulation of Eq. (2.44) in the frequency domain. The derivation of the equations implemented for the estimation of the tonal noise is reported in the next sections.

2.5.1 Tonal fan noise: fundamental equations

The theoretical prediction of the periodic noise generated by propellers is based on the solution of the Ffowcs-Williams and Hawkins equation (2.45). As said before, the mathematical modeling provided in Eq. (2.45) leads to the recognition of three basic components:

- thickness noise associated with fluid-displacement effects around moving blades;
- loading noise generated by the steady and unsteady blade forces;
- flow noise due to flow inhomogeneities around the blades.

This last component is important in transonic flows and can be neglected in all the cases where the flow field around the propeller is subsonic [34]. Moreover, assuming the case of rotating thin blades, the loading noise most often dominates. In other words, in Eq. (2.45), only the contribution of the dipoles matter. In such a case Eq. (2.52) becomes:

$$\rho'(\mathbf{x}, t) = -\frac{1}{4\pi c_0^2} \frac{\partial}{\partial x_i} \iint_{\partial V_\eta} \left[\frac{f_i n_j}{R|1 - \mathbf{M} \cdot \mathbf{R}/R|} \right] d^2\boldsymbol{\eta} \quad (2.55)$$

At this stage, it becomes convenient to assume that the extent of the source domain is acoustically compact. Such approximation means that \mathbf{R} and \mathbf{M} now designate the coordinate and Mach number of the center of gravity of the surface S where the dipole is located. If the source domain is not acoustically compact, it can be decomposed as a sum of compact sources by dividing the surface S into compact sub-domains. The overall acoustic field is then obtained by summing sub-domain contributions that cite rogerNEARFIELDFANNOISE2007. In addition to the previous assumption, it might be considered that as the blade thickness is also compact at the frequencies of interest, the differences of retarded times over the surface can also be neglected [35], and Eq. (2.55) can be approximated by:

$$\rho'(\mathbf{x}, t) \sim -\frac{1}{4\pi c_0^2} \frac{\partial}{\partial x_i} \left[\frac{F_i}{RD} \right] \quad (2.56)$$

where the Doppler factor $|1 - \mathbf{M} \cdot \mathbf{R}/R|$ has been called D . With the point dipole strength given by:

$$F_i = \int_S f_i d^2\boldsymbol{\eta} \quad (2.57)$$

In order to derive the space derivative in Eq. (2.56) different steps must be followed [36]. First of all, since the retarded time τ depends on the listener position, the chain rule applied to the derivation of a quantity $f(\mathbf{x}, \tau)$ yields:

$$\frac{df}{dx_i} = \left(\frac{\partial f}{\partial x_i} \right)_\tau + \left(\frac{\partial f}{\partial \tau} \right)_\mathbf{x} \frac{\partial \tau}{\partial x_i} \quad (2.58)$$

where $\partial\tau/\partial x_i$ can be derived by applying the same chain rule to the retarded time equation (2.49), which leads to the general differentiation rule:

$$\frac{\partial \tau}{\partial x_i} = -\frac{R_i}{c_0 R D} \quad (2.59)$$

Applying what obtained to the term in Eq. (2.56) yields:

$$\frac{\partial}{\partial x_i} \left[\frac{F_i}{RD} \right] = -\frac{R_i}{c_0 R^2 D} \frac{\partial}{\partial \tau} \left(\frac{F_i}{D} \right)_\mathbf{x} - \frac{F_i R_i}{R^3 D^2} + \frac{F_i}{R^3 D^2} \left(M_i R - \frac{\mathbf{M} \cdot \mathbf{R} R_i}{R} \right) \quad (2.60)$$

so Eq. (2.56) becomes:

$$\rho'(\mathbf{x}, t) = \frac{1}{4\pi c_0^2} \left[\frac{R_i}{c_0 R^2 D} \frac{\partial}{\partial \tau} \left(\frac{F_i}{D} \right)_\mathbf{x} + \frac{F_i R_i}{R^3 D^2} - \frac{F_i}{R^3 D^2} \left(M_i R - \frac{\mathbf{M} \cdot \mathbf{R} R_i}{R} \right) \right] \quad (2.61)$$

where the bracketed terms still are evaluated at the retarded time τ .

Integration in the time domain is computationally demanding and requires a high resolution of the flow field at the higher frequencies of interest [37]. It is therefore convenient to compute the acoustic field in the frequency domain:

$$\rho'(\mathbf{x}, \omega) = \frac{1}{2\pi} \int_{-\infty}^{\infty} \rho'(\mathbf{x}, t) e^{-i\omega t} dt \quad (2.62)$$

Taking the Fourier Transform of Eq. (2.61) leads:

$$\rho'(\mathbf{x}, \omega) = \frac{1}{8\pi^2 c_0^2} \int_{-\infty}^{\infty} \left[\frac{R_i}{c_0 R^2 D} \frac{\partial}{\partial \tau} \left(\frac{F_i}{D} \right)_\mathbf{x} + \frac{F_i R_i}{R^3 D^2} - \frac{F_i}{R^3 D^2} \left(M_i R - \frac{\mathbf{M} \cdot \mathbf{R} R_i}{R} \right) \right] e^{-i\omega t} dt \quad (2.63)$$

Since the integrand is a function of the retarded time τ , it is more convenient to make it the variable of integration, which can be done using the retarded time expression (2.49) and:

$$\frac{dt}{d\tau} = D \quad (2.64)$$

giving:

$$\rho'(\mathbf{x}, \omega) = \frac{1}{8\pi^2 c_0^2} \int_{-\infty}^{\infty} \left[\frac{R_i}{c_0 R^2} \frac{\partial}{\partial \tau} \left(\frac{F_i}{D} \right)_{\mathbf{x}} + \frac{F_i R_i}{R^3 D} - \frac{F_i}{R^3 D} \left(M_i R - \frac{\mathbf{M} \cdot \mathbf{R} R_i}{R} \right) \right] e^{-i\omega(\tau+R/c_0)} d\tau \quad (2.65)$$

Integrating the different terms in the brackets by parts, the acoustic density generated by the rotating dipole then becomes:

$$\rho'(\mathbf{x}, \omega) = \frac{ik}{8\pi^2 c_0^2} \int_{-\infty}^{\infty} \frac{\mathbf{F} \cdot \mathbf{R}}{R^2} \left(1 + \frac{1}{ikR} \right) e^{-i\omega(\tau+R/c_0)} d\tau \quad (2.66)$$

Eq. (2.66) is quite general and it does not introduce any assumption on the periodicity of the forces nor trajectory of the dipole.

Considering a rotating point source, Figure 3.2 illustrate the propeller and listener coordinates. Calling Ω the constant angular speed of the dipole, and posing $\beta \equiv \Omega t + \varphi'$, then we have:

$$\mathbf{x} = (x \sin \theta \cos \varphi, x \sin \theta \sin \varphi, x \cos \theta), \quad (2.67)$$

$$\mathbf{y} = (r' \cos \beta, r' \sin \beta, \zeta_3), \quad (2.68)$$

$$\mathbf{F} = (-F_D \sin \beta + F_R \cos \beta, F_D \cos \beta + F_R \sin \beta, -F_T), \quad (2.69)$$

where F_R , F_D , and F_T are the radial, drag, and thrust forces acting on the blade, respectively.

Using $\mathbf{R} = \mathbf{x} - \mathbf{y}$, the $\mathbf{F} \cdot \mathbf{R}$ product in Eq. (2.66) becomes:

$$\mathbf{F} \cdot \mathbf{R} = -F_D x \sin \theta \sin(\beta - \varphi) + F_R (x \sin \theta \cos(\beta - \varphi) - r') + F_T (\zeta_3 - x \cos \theta) \quad (2.70)$$

Following the determination of the source field, the acoustic field of the propeller can be computed via Eq. (2.66). Furthermore, knowing that the source (and so the sound field) is periodic with angular frequency Ω , the acoustic field of the fan can be computed only for the harmonics, precisely at the blade passing frequency. Therefore, the need for only the tonal components leads to a reduction of the computation time. In the considered case, the sound field can be expanded as a Fourier series due to its periodicity. The n th harmonic of the density fluctuation becomes:

$$\rho'_n = \frac{\Omega}{2\pi} \int_0^{2\pi/\Omega} \rho'(\mathbf{x}, t) e^{-in\Omega t} dt \quad (2.71)$$

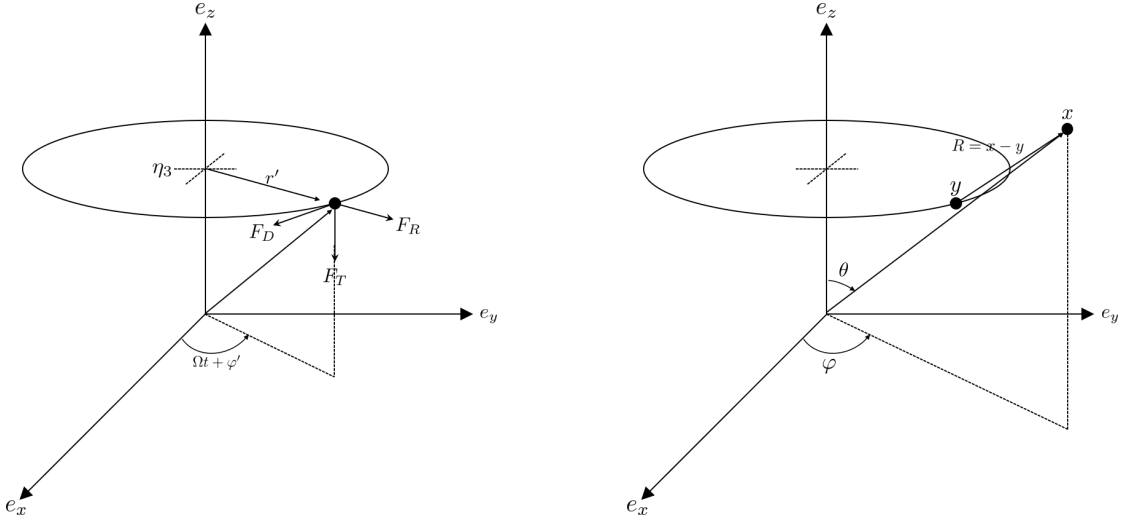


Figure 2.6: Source and listener coordinates.

2.5.2 Far-field approximation

Some applications need to compute the free-field acoustic fields for the observers located in both the geometrical and acoustical far-field of the fan. Such a situation allows to make simplifications in the derivation [38]. Considering large values of R , Eq. (2.60) becomes:

$$\frac{\partial}{\partial x_i} \left[\frac{F_i}{RD} \right] \sim -\frac{R_i}{c_0 R^2 D} \frac{\partial}{\partial \tau} \left(\frac{F_i}{D} \right) \quad (2.72)$$

Introducing Eq. (2.72) into Eq. (2.56) yields the acoustic density generated by a compact dipole source when the listener is considered far from the source:

$$\rho'(\mathbf{x}, t) \sim \frac{1}{4\pi c_0^2} \frac{R_i}{c_0 R^2 D} \frac{\partial}{\partial \tau} \left(\frac{F_i}{D} \right) \quad (2.73)$$

Then, the harmonic components of the sound are obtained by introducing Eq. (2.73) into Eq. (2.71):

$$\rho'_n \sim \frac{\Omega}{8\pi^2 c_0} \int_0^{2\pi/\Omega} \frac{x_j}{x^2 D} \frac{\partial}{\partial \tau} \left(\frac{F_i}{D} \right) e^{-in\Omega t} dt, \quad (2.74)$$

where the R_j/R^2 terms is replaced with its asymptotic value x_j/x^2 . It is convenient to change the integral variables from t to τ , since the integrand in Eq. (2.75) is evaluated at the retarded time τ . Acoustic density perturbations then becomes:

$$\rho'_n \sim \frac{\Omega}{8\pi^2 c_0} \frac{x_j}{x^2} \int_0^{2\pi/\Omega} \frac{\partial}{\partial \tau} \left(\frac{F_i}{D} \right) e^{-in\Omega(\tau+R/c_0)} d\tau, \quad (2.75)$$

where the scalar product, when the far-field approximation is considered, is equal to

$$\mathbf{F} \cdot \mathbf{x} = -F_D \sin \theta \sin(\beta - \varphi) + F_R \sin \theta \cos(\beta - \varphi) - F_T \cos \theta \quad (2.76)$$

The presence of the relative motion between the source and the observer lead to the necessity of introducing the Bessel function, which manages the modulation of the frequency shift caused by the mentioned motion. The Bessel functions identities are reported below:

$$e^{iZ \cos \beta} = \sum_{m=-\infty}^{+\infty} (-i)^m J_m(Z) e^{-im\beta}, \quad (2.77)$$

where $\beta \equiv \Omega\tau + \varphi' - \varphi$ and $Z \equiv n\Omega r' \sin \theta / c_0 = k_n r' \sin \theta$, with $k_n = n\Omega / c_0$ the wave number of the n th harmonics. Additionally, the derivatives of Eq. (2.77) are needed:

$$-\sin \beta e^{iZ \cos \beta} = \frac{1}{Z} \sum_{m=-\infty}^{+\infty} (-i)^m J_m(Z) m e^{-im\beta} \quad (2.78)$$

$$\cos \beta e^{iZ \cos \beta} = \sum_{m=-\infty}^{+\infty} (-i)^{m-1} J'_m(Z) e^{-im\beta} \quad (2.79)$$

Putting Eqs. (2.77)-(2.78)-(2.79) in Eq. (2.75) leads to:

$$\begin{aligned} \rho'_n \sim & -\frac{ik_n}{4\pi^2 c_0 x} e^{-ik_n x} \sum_{p=-\infty}^{\infty} e^{-i(n-p)(\varphi-\pi/2)} \\ & \left[J_{-n+p}(-k_n r' \sin \theta) \left(\cos \theta F_p^{(T)} - \frac{n-p}{k_n r'} F_p^{(D)} \right) \right. \\ & \left. - i J'_{-n+p}(-k_n r' \sin \theta) \sin \theta F_p^{(R)} \right], \quad (2.80) \end{aligned}$$

where the change of indices $p \equiv n + m$ has been used. Indeed, for practicality, the sum is considered over the harmonics of the forces than over the orders of the Bessel function.

Eq. (2.80) is general and applies even if every blade is different from every other. However, the propellers usually consist of B identical and equally spaced blades. The force acting on the $s = 1$ blade at time τ is the same as the force which acts at the time $\tau + (2\pi/\Omega B)(s-1)$ on the blade which is displaced by angle $2\pi(s-1)/(\Omega B)$. Using the identity:

$$\sum_{s=1}^B e^{in2\pi(s-1)/B} = \begin{cases} B & \text{for } n = mB \\ 0 & \text{for } n \neq mB \end{cases}, \quad (2.81)$$

where m is an integer, the density fluctuations becomes [35]:

$$\rho'_n \sim -\frac{iBk_{nB}}{4\pi^2 c_0 x} e^{-ik_{nB}x} \sum_{p=-\infty}^{\infty} e^{-i(n-p)(\varphi-\pi/2)} \left[J_{-nB+p}(-k_{nB}r' \sin \theta) \left(\cos \theta F_P^{(T)} - \frac{nB-p}{k_{nB}r'} F_P^{(D)} \right) - iJ'_{-nB+p}(-k_{nB}r' \sin \theta) \sin \theta F_p^{(R)} \right], \quad (2.82)$$

where $k_{nB} = nB\Omega/c_0$ is the wave number of the nB th harmonic. The $p = 0$ contribution considers only the steady forces acting on the blades (Gutin's model [39]).

2.5.3 Near-field correction

The theory mentioned in the previous section has been used in many industrial applications where the observer position is located in both geometrical and acoustical far-field. However, there are cases where the far-field assumption becomes invalid. Indeed, the acoustic quantities are required to be computed in the near-field of the propeller when the observer is located in the proximity of the fan or acoustic scattering takes part due to installation effects. A complete closed-form exact analytical solution was proposed by Roger without making the far-field assumption for the rotating machine [33, 36].

Using Eq. (2.70) in Eq. (2.66) gives:

$$\rho'(\mathbf{x}, \omega) = \frac{ik}{8\pi^2 c_0^2} \int_{-\infty}^{\infty} \left[-G_2(\tau) F_D x \sin \theta + G_3(\tau) F_R x \sin \theta + G_1(\tau) (F_T(\zeta_3 - x \cos \theta) - F_R r') \right] e^{-i\omega\tau} d\tau, \quad (2.83)$$

where the auxiliary functions G_1 , G_2 and G_3 are defined as:

$$G_1(t) = \frac{e^{-ikR}}{R^2} \left(1 + \frac{1}{ikR} \right), \quad (2.84)$$

$$G_2(t) = \sin(\Omega t + \varphi' - \varphi) G_1(t) \quad (2.85)$$

$$G_3(t) = \cos(\Omega t + \varphi' - \varphi) G_1(t), \quad (2.86)$$

where the acoustical near-field contribution is included by term $1 + 1/(ikR)$. As

previously done, the sound field can be again expanded as a Fourier series:

$$\rho'_n = \frac{ik_n\Omega}{8\pi^2c_0^2} \int_0^{2\pi\Omega} \left[-G_2(\tau)F_D x \sin \theta + G_3(\tau)F_R x \sin \theta + G_1(\tau)(F_T(\zeta_3 - x \cos \theta) - F_R r') \right] e^{-in\Omega\tau} d\tau \quad (2.87)$$

Moreover considering that also the sources have the same periodicity of the sound field, they can be represented as Fourier series:

$$F_\alpha(\tau) = \sum_{p=-\infty}^{\infty} F_p^{(\alpha)} e^{ip\Omega\tau}, \quad (2.88)$$

where $\alpha = T, D, R$ s the thrust, drag, and radial components of the source strength. The combination of Eqs. (2.87) and (2.88) yields:

$$\sum_{p=-\infty}^{\infty} F_p^{(\alpha)} \int_0^{2\pi\Omega} -G_N(\tau) e^{-i(n-p)\Omega\tau} = \frac{2\pi}{\Omega} \sum_{p=-\infty}^{\infty} F_p^{(\alpha)} G_{n-p}^{(\alpha)}, \quad (2.89)$$

where G_{Nm} is the m th Fourier component of the auxiliary Green's functions G_N ($N = 1, 2, 3$).

In the end, the acoustic field becomes:

$$\rho'_n = \frac{ik_n\Omega}{4\pi} \int_0^{2\pi\Omega} \left[-G_{n-p}^{(2)} F_p^{(D)} x \sin \theta + G_{n-p}^{(3)} F_p^{(R)} x \sin \theta + G_{n-p}^{(1)} (F_p^{(T)}(\zeta_3 - x \cos \theta) - F_p^{(R)} r') \right] e^{-in\Omega\tau} d\tau \quad (2.90)$$

Using the same assumptions as in the previous section, the model can be applied to B equally spaced blades:

$$\rho'_{nB} = \frac{ik_{nB}\Omega}{4\pi} \int_0^{2\pi\Omega} \left[-G_{nB-p}^{(2)} F_p^{(D)} x \sin \theta + G_{nB-p}^{(3)} F_p^{(R)} x \sin \theta + G_{nB-p}^{(1)} (F_p^{(T)}(\zeta_3 - x \cos \theta) - F_p^{(R)} r') \right] e^{-in\Omega\tau} d\tau \quad (2.91)$$

The main difference between Eq. (2.91) and Eq. (2.82) lies in the required computation of the Fourier Transform of the auxiliary Green's function for the near-field formulation.

2.5.4 Fixed dipoles array

The tonal noise caused by the rotation of the sources can be alternatively obtained from a continuous distribution of stationary, phase-shifted dipoles on the circle of

radius r [32]. Indeed, instead of one single rotating dipole, an infinite number of fixed dipoles can be used to reproduce equivalently the rotation (Figure 2.7). Therefore, the phase difference of the dipoles provides the rotation of the fan. Consequently, the azimuthal position of the dipoles β_{dipo} represents a key parameter to simulate the rotation of the dipole. Furthermore, since this methodology represents a numerical integration of the source field, the number of dipoles (integral resolution) required for an accurate representation also needs to be determined (Section 6.1.3).

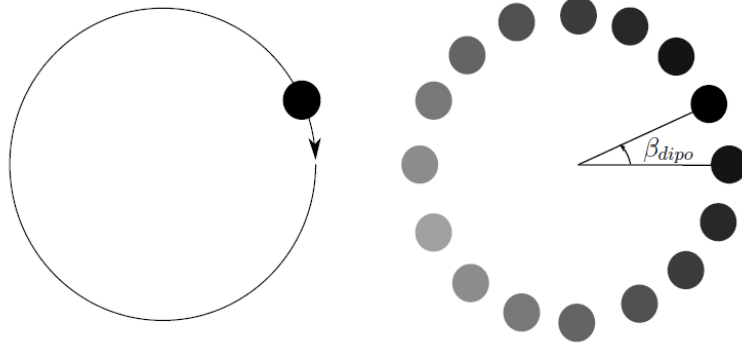


Figure 2.7: Fan source modeling strategies: single rotating dipole (left) and continuous array of phase shifted dipoles (right).

First of all, the source is assumed acoustically compact in the radial direction. Such approximation means the vanishing of the area integral in Eq. (2.55). On the other hand, the azimuthal variations of the dipole positions are kept with a radius equal to r' , since the source will be represented by a continuous distribution of dipoles. The integral from 0 to 2π can now be replaced by the summation of the dipoles:

$$\int_0^{2\pi} 2\varphi' = \sum_{N_{dipo}} \int_{\beta_{dipo} - \frac{2\pi}{N_{dipo}}}^{\beta_{dipo} + \frac{2\pi}{N_{dipo}}} d\varphi', \quad (2.92)$$

where N_{dipo} is the number of dipoles used. Considering that the dipole sources are assumed compact in the azimuthal direction, the azimuthal integral over φ' is substituted by a summation over β_{dipo} . From the initial dipole can be evaluated the strength of the phase-shifted dipoles:

$$F(\beta_{dipo}, t) = F\left(0, t - \frac{n\beta_{dipo}}{\omega}\right) \quad (2.93)$$

The source strength $F(0, t) = |F|e^{i\omega t}$, where $|F|$ stands for the dipole amplitude. The force strength of each dipole then becomes:

$$F_{n,dipo}^{(\alpha)} = \sum_{p=-\infty}^{\infty} F_p^{(\alpha)} e^{i(n-p)\beta_{dipo}} \quad (2.94)$$

Using the assumptions described in the previous section for a propeller containing B equally distributed blades, the source strength becomes:

$$F_{nB,dipo}^{(\alpha)} = \sum_{p=-\infty}^{\infty} F_p^{(\alpha)} e^{i(nB-p)\beta_{dipo}} \quad (2.95)$$

Introducing the source strength to the acoustic density formulation Eq. (2.55), the total acoustic field generated by the circular array of phase-shifted dipoles finally becomes:

$$\rho'_{nB} = \frac{B}{N_{dipo}} \sum_{N_{dipo}} \rho'_{nB,dipo} \quad (2.96)$$

Eq. (2.96) does not reproduce only the far-field. It generates a uniformly valid description in the entire space. Therefore, it can be applied separately to all stationary dipoles constituting the continuous array to compute its diffraction by an obstacle of arbitrary shape.

The formulation reported in this section will be implemented in Matlab for the computation of the tonal noise in the continuation of this thesis.

Chapter 3

Computational fluid dynamics theoretic background

Considering that the choice of the CFD model is strictly related to the acoustic estimation (as said in Section 2.3), then a better understanding of the theories regarding the computation of the flow-field seemed to be necessary. Therefore, this chapter aims to give further information about the nature of turbulence and the different models used in Computational Fluid Dynamics to analyze turbulent flows.

3.1 Introduction to turbulence

Turbulent motion is the natural state of most fluids in both nature and technology. Indeed, "*there are many opportunities to observe turbulent flows in our everyday surroundings, whether it be smoke from a chimney, water in a river or waterfall, or the buffeting of a strong wind*" [40].

Different definitions of flow turbulence or turbulent flow have been given over the years. In order to have a better understanding, the main characteristics of turbulence flows have been resumed [41]:

- Irregular or random. Turbulent flows have random velocity fluctuations with a wide range of length and time scales.
- Rich in scales of eddying motion. The large-scale motions are strongly influenced by the geometry of the flow. On the other hand, the behavior of the small-scale motions may be determined almost entirely by the rate at which they receive energy from the large scales.

- Large Reynolds number. Turbulence arises due to instabilities occurring at high Reynolds numbers. In other words, this happens when the timescale for viscous damping of a velocity fluctuation is much larger than the timescale for convective transport. Reynolds number is defined as:

$$Re = \frac{\text{Inertia force}}{\text{Viscous force}} = \frac{UL}{\nu}, \quad (3.1)$$

where U is the velocity, L is a characteristic length, and ν is the kinematic viscosity.

- Dissipative. In all turbulent flows, there is a flux of energy from the largest turbulent scales (energy extracted from the mean flow) to the small scales. At the smallest scales, the turbulent kinetic energy is dissipated into heat due to viscous stresses. This flux of energy is commonly referred to as the energy cascade. The reason for this energy flux is that large eddies are unstable and break up into smaller eddies, thereby transferring the energy to smaller scales. A consequence of the dissipation is that turbulence decays rapidly if no energy is supplied to the system.
- Highly vortical. Turbulent flow is rotational and characterized by high levels of fluctuating vorticity.
- Three dimensional. The vortices mechanisms, such as vortex stretching and vortex tilting (two important vorticity-maintenance mechanisms), cannot occur in two dimensions.
- Highly diffusive. Turbulent flows's diffusivity is much greater than that of a laminar flow (molecular diffusivity). The highly diffusive turbulence causes rapid mixing and increased rates of momentum, heat, and/or mass transfer.
- Continuum. Turbulence is governed by the equations of fluid mechanics. Even the smallest turbulent length scales are much larger than the molecular length.

3.2 Numerical methods

Turbulence modeling is one of the key elements in CFD. Unfortunately, as seen in the previous section, turbulent flows are characterized by fluctuating velocity fields in which exist small-scale and high-frequency fluctuations. Thus an enormous amount of information is required if one is to describe turbulent flows completely. In the end, a lot of computing power is required to solve turbulence simulations and their complex numerical models. On the other hand, we usually require something less than the complete time history of every flow property's overall

spatial coordinates. Instead of simulating the exact governing equations, these equations can be manipulated to remove the small-scale high-frequency fluctuations, resulting in a modified set of equations that is computationally less expensive to solve. As a consequence of the manipulation, the modified equations contain additional unknown variables. Hence, turbulence models are needed to determine these variables.

Turbulence modeling can therefore be described as the process of closing the modified Navier–Stokes equations by providing required turbulence models. During the last few decades, numerous turbulence models of varying complexity have been proposed. The selection among these models is crucial for a successful simulation. Knowledge about the flow (i.e. whether or not the flow involves separation, whether the features of the flow resulting from anisotropy etc.) significantly simplifies the decision by reducing the number of turbulence models that can be used. Furthermore, in practical engineering applications, the selection of turbulence models can be restricted by the computational resources that are available or affordable.

There are two extremes when it comes to turbulence modeling. The models based on the Reynolds-Averaged Navier-Stokes (RANS) equations [42] take care of all eddy scales, as none are resolved directly by the RANS equations. At the other extreme, there is the Direct Numerical Simulation (DNS) [43], where all turbulent eddies are explicitly resolved and no turbulence models are necessary. With the increase of the Reynolds number, the resolving of a growing number of progressively smaller momentaneous eddies forbids the practicality of DNS. For this reason, Large Eddy Simulation (LES) [44] and its counterparts that resolve eddies (but only the large ones) emerge as a versatile compromise.

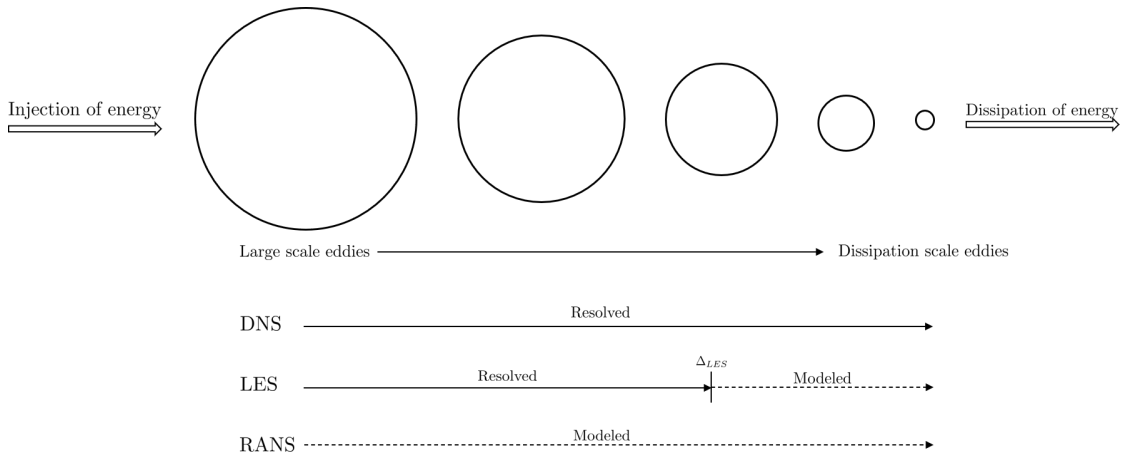


Figure 3.1: A schematic overview of turbulence modelling.

In the next sections will be provided a general description of the different models

mentioned before (resumed in Figure 3.1).

3.2.1 Direct numerical simulation

In Direct Numerical Simulation (DNS), a complete time-dependent, three-dimensional solution of the Navier-Stokes and continuity equations is calculated [45]. Indeed, there is no need for a turbulence model since the equations are solved without any further simplifications. Therefore, as all length scales from the largest to the smallest are explicitly resolved, DNS requires a grid size smaller than the smallest scale of turbulence (Kolmogorov scale) [46]. This, along with the required fine computational time step, makes it a forbidden task for large geometries and/or high Reynolds number problems.

At the present time DNS is a research tool rather than an aid to engineering design. The computational cost of DNS is high and it increases as the cube of the Reynolds number. Such deterministic simulations are useful for developing closures for statistical turbulence models and validation of these models, but in practical engineering simulations, DNS is less useful.

3.2.2 Reynolds average Navier Stokes equations

The intrinsic nature of turbulence flows (Section 3.1) make the solving of the unsteady Navier-Stokes more difficult than cases which involve laminar flows.

The main problem is that the extremely small time and space scales of the turbulent motion result in a large number of grid points and small time steps. One way to reduce the complications related to the features of turbulent flows is to use one of the principal characteristics of turbulence: the presence of random fluctuations of the various flow properties. Therefore a statistical approach can be formulated to numerically solve turbulent flow. One of the first to develop this way of reasoning was Reynolds [42], who expressed all quantities as the sum of mean and fluctuating parts.

According to the Reynolds decomposition, we express the instantaneous velocity $u_i(\mathbf{x}, t)$ for a Cartesian coordinate system, as the sum of a mean, $\bar{U}_i(\mathbf{x})$, and a fluctuating part, $u'_i(\mathbf{x}, t)$, so that:

$$u_i(\mathbf{x}, t) = \bar{U}_i(\mathbf{x}) + u'_i(\mathbf{x}, t), \quad (3.2)$$

where, following Reynolds, the time-average quantity \bar{U} is defined as:

$$\bar{U}(\mathbf{x}) = \lim_{T \rightarrow \infty} \frac{1}{T} \int_0^T u(\mathbf{x}, t) dt, \quad (3.3)$$

where T is the time period over which the average is taken, and for practical measurements, it must be a finite quantity.

In order to simplify the modeling substantially, in the remainder of this section, the case of a steady incompressible flow is considered. This assumption is valid for low-speed aerodynamics ($M < 0.3$). Considering this simplification, the equations for conservation of mass (2.1) and momentum (2.2) will assume the following form:

$$\frac{\partial u_j}{\partial x_j} = 0, \quad (3.4)$$

$$\rho \frac{\partial (u_j u_i)}{\partial x_j} = -\frac{\partial p}{\partial x_i} + \frac{\partial \tau_{ij}}{\partial x_j} \quad i = 1, \dots, 3 \quad (3.5)$$

Applying Eq. (3.2) at both the velocity and pressure field, and time averaging equations (3.4) and (3.5) yields the Reynolds averaged Navier-Stokes equations (RANS) of motion:

$$\frac{\partial \bar{U}_i}{\partial x_i} = 0, \quad (3.6)$$

$$\rho \frac{\partial (\bar{U}_i \bar{U}_j)}{\partial x_j} = -\frac{\partial \bar{P}}{\partial x_i} + \mu \frac{\partial^2 \bar{U}_i}{\partial x_j \partial x_j} - \rho \frac{\partial}{\partial x_j} (\overline{u'_i u'_j}), \quad (3.7)$$

where has been also assumed that there are no pressure fluctuations for this constant density flow, so \bar{P} is the time-averaging value of p .

In appearance, the Reynolds equations (3.6), (3.7) and the Navier-Stokes equations (3.4), (3.5) are the same, except for the appearance of the correlation $\overline{u'_i u'_j}$. Herein lies the fundamental problem of turbulence for the engineer. Therefore, in order to compute all mean-flow properties of the turbulent flow under consideration, we need a prescription for computing $\overline{u'_i u'_j}$.

The quantity $-\rho \overline{u'_i u'_j}$ is known as the Reynolds stress tensor, which is very important since it introduces a coupling between the mean and fluctuating parts of the velocity field (incorporates the effects of turbulent motions on the mean stresses), and we denote it by τ_{ij}^{turb} . Thus:

$$\tau_{ij}^{turb} = -\rho \overline{u'_i u'_j}, \quad (3.8)$$

this is a symmetric tensor and thus has six independent components. Hence, we have produced six unknown quantities as a result of Reynolds averaging.

Since the Reynolds stress term contains products of the velocity fluctuations this term must be modeled to close (3.7). This is the sole purpose of RANS turbulence modeling. So for general three-dimensional flows, the Reynolds equations are not closed: they cannot be solved unless the Reynolds stresses are somehow determined. The so-called ‘‘closure problem’’ [45] is the challenge associated with finding supplementary relationships for the unknown correlations. The number of additional PDEs considered in addition to the RANS and continuity equations is used to classify the turbulence models [47, 48].

The RANS turbulence models are briefly discussed below in Section 3.3.

Unsteady Reynolds averaged Navier Stokes equations

The application of RANS models to highly unsteady flows involves solving the RANS equations in their unsteady form, actually leading to the unsteady Reynolds-averaged Navier–Stokes equations approach (uRANS) [49]. In such cases, the application of time-averaging for the Reynolds decomposition (and subsequent steady-state solution of the mean flow) is inappropriate and can lead to a significant source of error. Instead, an ensemble averaging over a suitable finite time period is required [50], such that the non-turbulent unsteadiness is resolved in the mean flow and the turbulent fluctuations are described by the RANS model.

Those equations could be obtained by introducing the unsteady terms in Eqs. (3.6) and (3.7), thus:

$$\frac{\partial \bar{U}_i}{\partial x_i} = 0, \quad (3.9)$$

$$\rho \frac{\partial \bar{U}_i}{\partial t} + \rho \frac{\partial}{\partial x_j} (\bar{U}_i \bar{U}_j) = -\frac{\partial \bar{P}}{\partial x_i} + \mu \frac{\partial^2 \bar{U}_i}{\partial x_j \partial x_j} - \rho \frac{\partial}{\partial x_j} (\overline{u'_i u'_j}) \quad (3.10)$$

uRANS is not without its difficulties, which can be significant. A strong and undesirable sensitivity to the choice of RANS model (see Section 3.3) is unfortunately a well-established feature of URANS [51]. Furthermore, uRANS simulations are computationally more expensive than steady-state RANS [52], the precise increase in numerical expense depends strongly on the flow in question and is usually less than that of LES.

3.3 RANS turbulence models

3.3.1 Zero-order models

The simplest of all turbulence closures are strictly algebraic. As such, they apply only to the “simplest” of turbulent flows (free-shear flows such as axisymmetric jets, 2D jets, and mixing layers). Algebraic turbulence models invariably utilize the Boussinesq assumption [53, 54].

In 1877, Boussinesq introduced the eddy viscosity approximation, thereby allowing one to approximate the turbulent flow by assigning a quantitative value to the eddy (dynamic) viscosity. Therefore, he modeled the turbulent stresses responsible for significantly augmenting the molecular counterpart within this eddy viscosity. Specifically, Boussinesq suggested that a turbulent flow could be regarded as having an enhanced dynamic viscosity, also called a turbulent or eddy viscosity μ_{turb} . Then,

the turbulent shear stress is defined as:

$$\tau_{ij} = -\overline{\rho u'_i u'_j} = \mu_{turb} \frac{\partial \bar{u}_i}{\partial x_j}, \quad (3.11)$$

where we can see that this assumption implies that the turbulence shear stress is related uniquely to the mean-flow conditions at each point. The eddy viscosity μ_{turb} is generally much larger than the fluid dynamic viscosity μ [55]. Furthermore, note that while μ is a constant for a given fluid at a specified state, μ_{turb} is a function of both flow condition and fluid density. In other words, the fluid viscosity is a property of the fluid, which is specified by the thermodynamic state that the fluid is in, whereas the eddy viscosity depends also on the specific flow conditions involved. Hence, standard flow experiments need to be carried out to quantify μ_{turb} before we can apply it to problems with similar conditions.

The Boussinesq hypothesis can be somewhat generalized by using the kinematic viscosity as opposed to the dynamic viscosity, and the problem of the closure of the RANS only depend on the determination of ν_{turb} . Initially, Boussinesq assumed that the turbulent kinematic viscosity ν_{turb} is a constant [54].

Boussinesq's eddy-viscosity concept represented the base for preciser zero-order models (e.g. Prandtl's mixing-length model [56]).

The motivation for developing more advanced models than the zero-equation models is different. First of all, these models can not predict flows with complicating features. Furthermore, they require frequently ad-hoc additions and corrections to handle specific effects, and constants need to be changed to handle different classes of shear flows. Therefore, the appealing to develop a model general enough that specific modifications to the constants are not required to treat different classes of flows increase over the years.

3.3.2 One-equation models

In 1967 Prandtl introduced the eddy-viscosity model, where the eddy viscosity is directly expressed as a function of the turbulent kinetic energy per unit mass, k . This choice represented the birth of the first one-equation model, where a single transport equation for the turbulent viscosity is solved. The actual development is rather involved. Anyway, the purposes of this section are to simply introduce the need of the actual model used in this thesis, which is proposed in Section 3.3.4.

In the cartesian coordinate system, we have a contribution to the turbulent kinetic energy from the x , y , and z directions. Then, the specific turbulence kinetic energy is defined as:

$$k = \frac{1}{2} \left(\overline{u'^2} + \overline{v'^2} + \overline{w'^2} \right) \quad (3.12)$$

Via dimensional analysis [45], we can relate this to the kinematic eddy viscosity by constant:

$$\nu_{turb} = constant \sqrt{kl}, \quad (3.13)$$

where the characteristic length l represents a turbulence length scale [40]. Because the kinetic energy of turbulence is a measurable quantity and is easily interpreted physically, it is natural to inquire how k might be predicted. An exact transport partial differential equation can be developed for k from the Navier-Stokes equations. Back in time, the different equation has been proposed [57, 58], here for example, the model transport equation for k illustrated by Pope [40] is reported:

$$\begin{aligned} \frac{\partial k}{\partial t} + \bar{U}_j \frac{\partial k}{\partial x_j} = & - \underbrace{\frac{\partial}{\partial x_j} \left[u'_j \left(\frac{u'_i u'_i}{2} + \frac{p'}{\rho} \right) - 2\nu u'_i \frac{1}{2} \left(\frac{\partial u'_i}{\partial x_j} + \frac{\partial u'_j}{\partial x_i} \right) \right]}_D \\ & - \underbrace{u'_i u'_j \frac{\partial \bar{U}_i}{\partial x_j}}_{P_k} - \underbrace{\nu \left(\frac{\partial u'_i}{\partial x_j} \frac{\partial u'_i}{\partial x_j} + \frac{\partial u'_i}{\partial x_j} \frac{\partial u'_j}{\partial x_i} \right)}_{\varepsilon} \end{aligned} \quad (3.14)$$

The first two terms of Eq. (3.14) are self-explanatory. Other terms involving unknown correlations need some discussion. The term D represents the turbulent transport of k by diffusion, is an inertial term and vanishes when integrated over the representative volume of any flow, implying that the term neither creates turbulence energy nor destroys it. The term P_k represents the rate of transfer (or production) of kinetic energy from the mean to the turbulent motion. The term ε represents the average kinematic dissipation rate of turbulence kinetic energy. In other words, the rate at which turbulence energy is destroyed by molecular viscous stresses. All those terms have to be modeled to compute the specific turbulent kinetic energy, k .

Not all the one-equation models solved the transport equation of turbulent kinetic energy and required an algebraic prescription of a length scale. For example, one of the most used one-equation models in modern CFD is the Spalart-Allmaras turbulence model [59].

In the end, one-equation models have proven to be relatively unsuccessful to compute fields that exhibit shear flow, separated flow, or decaying turbulence. Notwithstanding this drawback, they provide a step to more successful, higher-order models. Indeed, directly from the deficiencies of the one-equation models come the basis of two-equation modeling, where in addition to the transport equation describing the specific turbulence kinetic energy, k , an equation expressing the characteristic turbulent length scale l , or another appropriate quantity, is also introduced. Therefore, two-equation models are sometimes referred to as complete models, since they allow the turbulent velocity and length scales to be determined

independently, without prior knowledge of the turbulence structure. The two most acclaimed two-equation models are briefly described in the next sections.

3.3.3 Two-equation models: $k - \varepsilon$ model

The $k - \varepsilon$ model is the most widely used two-equation model. As is the case with all turbulence models, both the concepts and the details evolved. Launder and Sharma [60, 61] among others led to the popularity of this $k - \varepsilon$ model. In this section has been reported only the model formulated by Launder-Sharma [61], which is known as the Standard $k - \varepsilon$ model.

The modeled equation for k , is obtained substituting the closures [62] into the exact transport equation for k (Eq. (3.14)), this leads to:

$$\frac{\partial k}{\partial t} + \bar{U}_j \frac{\partial k}{\partial x_j} = \nu_T \left[\left(\frac{\partial \bar{U}_i}{\partial x_j} + \frac{\partial \bar{U}_j}{\partial x_i} \right) \frac{\partial \bar{U}_i}{\partial x_j} \right] - \varepsilon + \frac{\partial}{\partial x_j} \left[\left(\nu + \frac{\nu_T}{\sigma_k} \right) \frac{\partial k}{\partial x_j} \right], \quad (3.15)$$

where σ_k is a model coefficient known as the Prandtl-Schmidt number, ν_T is the turbulent viscosity and ε is the energy dissipation of turbulent kinetic energy. To close Eq. (3.15) we need to compute ε and ν_T . The energy-dissipation rate is modeled with a second transport equation.

The general form of the modeled ε equation is here reported:

$$\frac{\partial \varepsilon}{\partial t} + \bar{U}_j \frac{\partial \varepsilon}{\partial x_j} = C_{\varepsilon_1} \nu_T \frac{\varepsilon}{k} \left[\left(\frac{\partial \bar{U}_i}{\partial x_j} + \frac{\partial \bar{U}_j}{\partial x_i} \right) \frac{\partial \bar{U}_i}{\partial x_j} \right] - C_{\varepsilon_2} \frac{\varepsilon^2}{k} + \frac{\partial}{\partial x_j} \left[\left(\nu + \frac{\nu_T}{\sigma_\varepsilon} \right) \frac{\partial \varepsilon}{\partial x_j} \right] \quad (3.16)$$

The relation between the turbulent viscosity ν_T , the turbulent kinetic energy k and the energy-dissipation rate ε is given by:

$$\nu_T = C_\mu \frac{k^2}{\varepsilon}, \quad (3.17)$$

where Eq. (3.17) give the closure of the RANS equations.

The five closure coefficients (C_μ , C_{ε_1} , C_{ε_2} , σ_k and σ_ε) in the $k - \varepsilon$ model are assumed to be universal and thus constant, although they can vary slightly from one flow to another. The values for these constants are given in Table 3.1.

The standard $k - \varepsilon$ model does not always give good accuracy. Examples of flows that cannot be predicted accurately with the standard $k - \varepsilon$ model are flows with streamline curvature, swirling flows, and axisymmetric jets. The inaccuracies stem from the underlying Boussinesq hypothesis which imposes isotropy and from how the dissipation equation is modeled. Actually, this model was derived and tuned for flows with high Reynolds numbers. Furthermore, the model parameters in the $k - \varepsilon$ model are a compromise to give the best performance for a wide range of different flows. The accuracy of the model can therefore be improved by adjusting

Constant	Value
C_μ	0.09
$C_{\varepsilon 1}$	1.44
$C_{\varepsilon 2}$	1.92
σ_k	1.00
σ_ε	1.30

Table 3.1: Closure coefficients in the standard $k-\varepsilon$ model.

the parameters for particular experiments. Improvements have been made to this model to improve its performance. In the literature, numerous modifications for the turbulence models have been suggested. The most well-known variants of the standard model are the RNG [63] and the realizable $k-\varepsilon$ models [64].

3.3.4 Two-equation models: $k-\omega$ model

The $k-\varepsilon$ model has been demonstrated to be inaccurate at predicting the boundary layer with adverse pressure gradients. The prediction is even worse when shocks are present (supersonic flows). Then, a better model is required for external aerodynamics and turbomachinery problems. The $k-\omega$ model is one of the models proposed to give a better performance when adverse pressure gradients are present. Many versions of the $k-\omega$ model have been proposed over the years [65, 66, 45]. The specific turbulence dissipation rate, ω , was firstly obtained by Kolmogorov [57] by dimensional analysis

$$\omega = \frac{\varepsilon}{C_\mu k} \quad (3.18)$$

where it should be interpreted as the inverse of the timescale on which dissipation occurs.

The modeled equation for the turbulent kinetic energy k is obtained similarly as Eq. (3.15), but introducing Eq. (3.18):

$$\frac{\partial k}{\partial t} + \bar{U}_j \frac{\partial k}{\partial x_j} = \nu_T \left[\left(\frac{\partial \bar{U}_i}{\partial x_j} + \frac{\partial \bar{U}_j}{\partial x_i} \right) \frac{\partial \bar{U}_i}{\partial x_j} \right] - \beta k \omega + \frac{\partial}{\partial x_j} \left[\left(\nu + \frac{\nu_T}{\sigma_k} \right) \frac{\partial k}{\partial x_j} \right], \quad (3.19)$$

and the modeled ω equation is:

$$\frac{\partial \omega}{\partial t} + \bar{U}_j \frac{\partial \omega}{\partial x_j} = \alpha \frac{\omega}{k} \nu_T \left[\left(\frac{\partial \bar{U}_i}{\partial x_j} + \frac{\partial \bar{U}_j}{\partial x_i} \right) \frac{\partial \bar{U}_i}{\partial x_j} \right] - \beta^* \omega^2 + \frac{\partial}{\partial x_j} \left[\left(\nu + \frac{\nu_T}{\sigma_k \omega} \right) \frac{\partial \omega}{\partial x_j} \right], \quad (3.20)$$

wherein this case the turbulent viscosity is calculated from:

$$\nu_T = \frac{k}{\omega} \quad (3.21)$$

Eq. (3.20) is obtained by making the same kind of assumptions that are made for the derivation of Eq. (3.16).

Eq. (3.18) shows that ω and ε represent the same physical quantity: the dissipation of the turbulent kinetic energy, indeed both of them are present in the turbulent kinetic energy equation as a sink term. However, there are slight differences between ω and ε which allows the $k - \omega$ to be more accurate for external aerodynamics and turbomachinery problems. One of the reasons the $k - \varepsilon$ model is less efficient when a wall is present, mainly because it uses damping functions in the viscous sub-layer, which are less rigorous in the presence of adverse pressure gradients.

The $k - \omega$ SST model

The main weakness of the $k - \omega$ model is the dependence on the freestream turbulence conditions [67]. It's not already clear why there is this freestream dependence, the most considerable answer are related to the missing of the cross-diffusion terms in the $k - \omega$ model and the not correctly tuning of the model coefficients ($\alpha, \beta, \beta^*, \sigma_k, \sigma_\omega$) [67]. A way founded to solve this sensitiveness is to blend the $k - \varepsilon$ and the $k - \omega$ model because the $k - \varepsilon$ model is not as susceptible to the freestream values of k , ω , and ε . This is the basis of the $k - \omega$ SST model [68].

The $k - \omega$ SST model deviate from the $k - \omega$ model for different elements. In order to understand is here reported the modified transport equation of ω :

$$\begin{aligned} \frac{\partial \omega}{\partial t} + \bar{U}_j \frac{\partial \omega}{\partial x_j} = & \alpha \frac{\omega}{k} \nu_T \left[\left(\frac{\partial \bar{U}_i}{\partial x_j} + \frac{\partial \bar{U}_j}{\partial x_i} \right) \frac{\partial \bar{U}_i}{\partial x_j} \right] - \beta^* \omega^2 \\ & + \frac{\partial}{\partial x_j} \left[\left(\nu + \frac{\nu_T}{\sigma_k \omega} \right) \frac{\partial \omega}{\partial x_j} \right] + 2(1 - F_1) \frac{\sigma_{\omega_2}}{\omega} \frac{\partial k}{\partial x_j} \frac{\partial \omega}{\partial x_j}, \end{aligned} \quad (3.22)$$

where the only difference between Eq. (3.20) and Eq. (3.22) is the presence of the fourth term on the right-hand side. This additional term presents the blending function F_1 [69], which blend the $k - \varepsilon$ model used far from the wall ($F_1 = 0$), to the $k - \omega$ model used in the areas close to the wall ($F_1 = 1$) (Figure 3.2). In order to have a smooth variation of the two models, F_1 is defined as a hyperbolic tangential function, whose argument depends on the distance to the closest wall. The blending function F_1 is also used to blend between the empirical constant of the two models:

$$\varphi = F_1 \varphi_\omega + (1 - F_1) \varphi_\varepsilon, \quad (3.23)$$

where φ_ω and φ_ε are the model constant in the $k - \omega$ and $k - \varepsilon$ model, respectively. Another important modification introduced in the SST model is the inclusion of a viscosity limiter in Eq. (3.21) to reduce the overprediction of the turbulent viscosity given by the standard $k - \omega$ model. The viscosity limiter is defined by using a blending function F_2 , which is defined similarly as F_1 .

The $k - \omega$ SST model has been proved to be the best turbulence model for external aerodynamics or a case where the separation is important. For this reason it will be used in the continuation of this thesis.

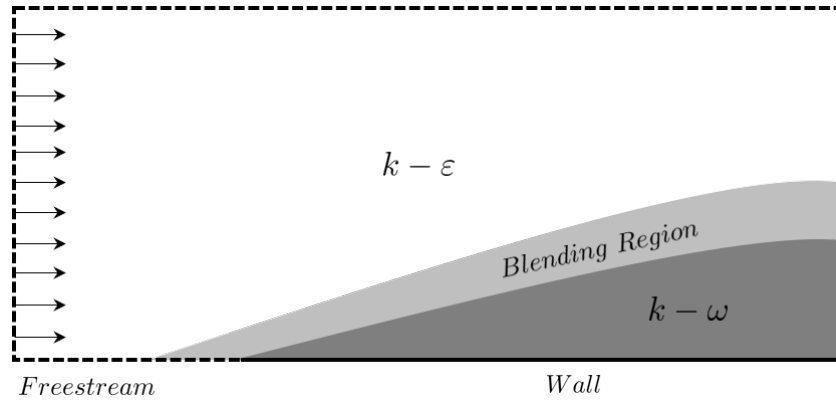


Figure 3.2: $k - \omega$ SST model basic idea representation. Picture modified from [70]

Chapter 4

Numerical setup for computational fluid dynamic simulations

In Chapter 2 the different reformulations of the Ffowcs-Williams and Hawkins analogy have been discussed, to highlight the input data needed for the prediction of the noise emitted by rotating machines. Since we are considering a hybrid approach to the acoustic, the flow field must be solved first. Therefore, Chapter 3 gave an introduction of the problems related to the numerical computation of turbulence flows and an overview of the turbulence models adopted in computation fluid dynamics (CFD).

The theoretical background exposed will be useful for the understanding of the choices done during the setup of the CFD simulations presented in this chapter. Three different situations have been considered:

1. actuator disk (case AD);
2. isolated propeller (case P);
3. propellers and drone air-frame (case PD).

4.1 Geometry

The DJI Phantom II quadcopter and its original DJI propeller were selected as the studied geometry. The CAD used in both cases P and PD were provided by NASA Ames Research Center, where the quadrotor and isolated rotor configurations were firstly tested and then 3D scanned [71]. The use of these CAD allows neglecting

the potential geometry errors during the validation of the data reported in Chapter 5.

The model 9450 used in the study has an average chord of approximately 0.025 m and a rotor diameter of 0.239 m (Figure 4.1 right). In order to simplify the creation of the rotating motion in case *PD*, the quadcopter geometry does not contain the brush motor, as shown in Figure 4.1 left.



Figure 4.1: Geometry CAD of cases *P* and *PD*.

4.2 Domain

The shape of the domain considered is based on two considerations: all the cases tested to operate well within the subsonic regime and with a Mach number $M < 0.3$. Therefore, STAR-CCM+ documentation [72] recommends using a bullet shape domain for incompressible external aerodynamics. Considering previous works [11, 10], the spherical end of the domain was created with a radius of ten times the characteristic length scale of the simulation (i.e the rotor diameter), L . The downstream domain was extended $20L$ downstream. For both *P* and *AD* simulations, the rotor is located within this domain at the center of the spherical end (Figure 4.2 left). On the other hand, for the *PD* simulation, the center of the spherical end coincides with the rotating plane of the four propellers (Figure 4.2 right).

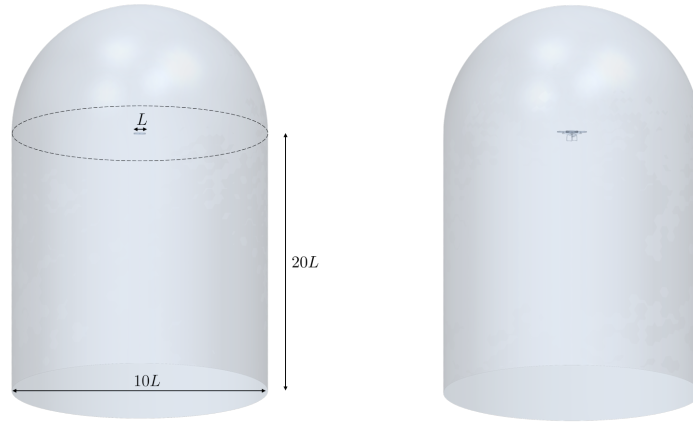


Figure 4.2: Simulation domains considered for the UAV CFD simulations in this thesis. Left: single-propeller domain (cases P , AD). Right: full-drone domain (case PD).

4.3 Motion

A rotating volume must be introduced inside the domain for the cases where a real rotating surface was present (P , PD). The shape of the rotating volume is different between the two simulations. Indeed, in the configuration P the propeller could be placed into a simple cylindrical shape volume (Figure 4.3 left) without any problems. However, the use of this shape also for the configuration PD , would have given an interference between the rotating region and the drone air-frame. Therefore, each of the four propellers of the simulation PD is contained in a rotating volume with a truncated cone shape (Figure 4.3 right).

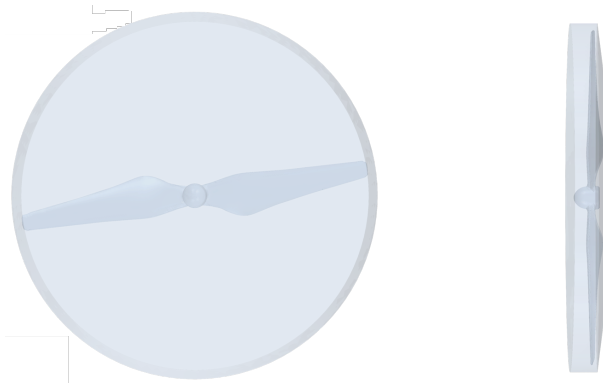


Figure 4.3: Simulation motion volume considered for the UAV CFD simulations in this thesis. Left: case P with isolated propeller. Right: case PD with propellers close to drone's surface .

All the simulations considered a propeller or actuator disk operating at the same

rotation rate of 6000 rpm. This choice is related to the availability of reference works for both the aerodynamic and acoustic validation of the results. Both case *P* and *AD* implemented counterclockwise rotations. Whereas case *PD* implemented both dual clockwise and counterclockwise rotors (Figure 4.4). Indeed, if all spun the same way it would cause the quadcopter to spin or yaw in the opposite direction due to the torque being generated by the motors.

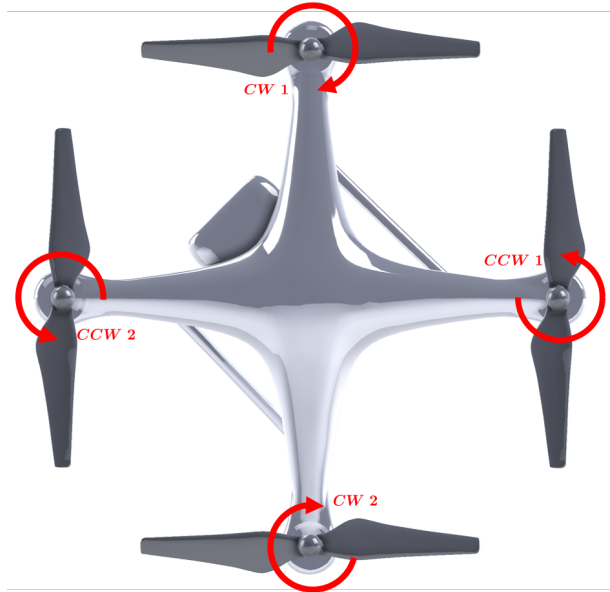


Figure 4.4: Full-drone propellers configurations. Two couple of both clockwise (top and bottom) and counterclockwise (left and right) rotating propellers.

4.3.1 Moving reference frame

The presence of a rotating part inside the domain in cases *P* and *PD* means the need of a CFD modeling technique to simulate the rotation. In current commercial CFD solvers, there are many approaches implemented to simulate fan rotation. In this thesis, two different approaches have been considered: the moving reference frame (MRF) model and the rigid body motion (RBM) model.

The MRF model [73] can be used in a steady-state simulation, employing a frozen rotor approach and transferring the velocities entering a user-defined region around the blades to a moving reference frame. The velocity viewed from the rotating frame is defined as:

$$\vec{v}_{MRF} = \vec{v} - \vec{\omega} \times \vec{r}, \quad (4.1)$$

where \vec{v} is the velocity from the global (stationary) reference frame, $\vec{\omega}$ is the rotational vector and \vec{r} is the position vector in the field of rotation (Figure 4.5).

An important limitation of this approach is that the user-defined MRF domain needs to be rotationally symmetric and must not contain any stationary non-rotationally symmetric parts. Must be noted that MRF assumes a weak interaction between the MRF volume and the surrounding stationary volumes.

On the other hand, the RBM method [72] is the most physically correct approach to use, since it actually performs the rotation, and can deal with strong interactions between the moving volume and the surrounding stationary volume. It requires an unsteady approach, where through interfaces the movement of a rotating domain (containing the rotor geometry) is transferred to the stationary domain. During the whole process, the mesh in each domain remains the same, sliding against each other. Therefore, this approach is often also referred to as the “sliding mesh” approach. In order to ensure proper exchange of information over the interface, the degree of rotation per time step is restricted, which typically results in extremely long runtimes.

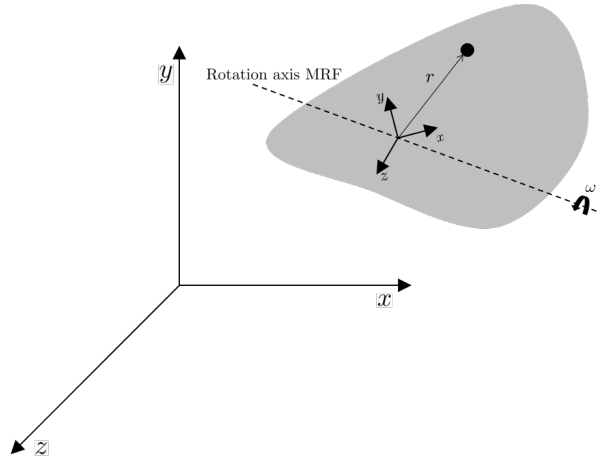


Figure 4.5: *Coordinate system for moving reference frame.*

4.4 Boundary conditions

The spherical end and the cylindrical surface of the domain were chosen to be a stagnation pressure inlet boundary, and the backside of the domain was defined as a pressure outlet boundary (Figure 4.6). These boundary conditions were all set to velocities of zero or the ambient pressure to represent hovering flight with no freestream flow. For both cases, P and PD , the transfer of cell information occurs only across the defined internal interface boundary, which corresponds with the surfaces of the rotating volumes described in the previous section. This type of boundary joins the two fluid volumes as though they were one continuous fluid

regime, like when an actual rotor is spinning in open space.

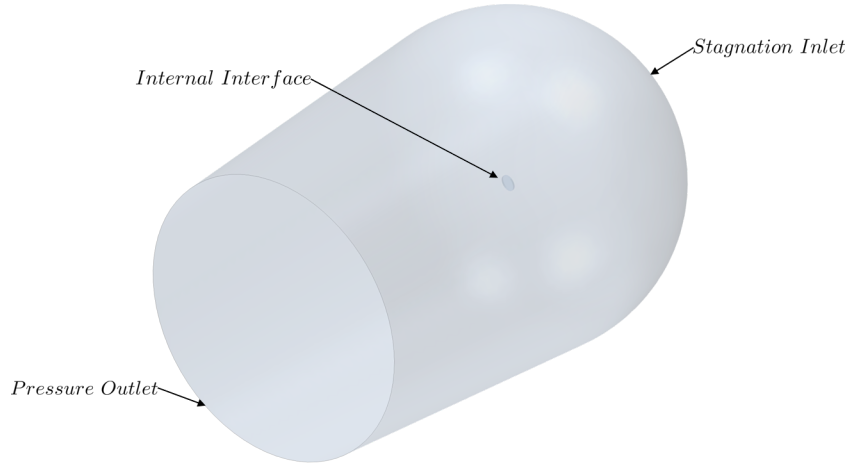


Figure 4.6: Boundary conditions used in simulations *P*, *AD* and *PD*.

4.5 Physics models and solvers

The physics models and solvers are largely dictated by the nature of our problem and the computational resources available. The three cases considered an incompressible ideal gas model since the rotors generally operate at a Mach number of less than 0.3, where compressibility and other air property changes are negligible.

The flow can be modeled in two ways: steady flow and unsteady flow. In steady flow modeling, time derivatives are made equal to zero, which simplifies the solution of the set of equations. Considering the simplicity of the problem analyzed in case *AD* (hovering of a single actuator disk in open space), only the steady case was analyzed. Furthermore, because case *AD* does not consider complex geometry, the RANS equations seemed to be the most reasonable choice for this simulation. On the other hand, unsteady flows advance in time according to a defined time step Δt . Therefore, because previous works [11, 74] show that the flow could contain relevant unsteadiness in cases similar to our *P* and *PD*, the implicit unsteady approach has been used. Given the aims and timeframe of this research, we focus on RANS and uRANS simulations of the UAV geometry.

In STARCCM+ two ways to solve the set of the equations are available: the coupled flow models and the segregated flow model. Coupled flow models solve the Navier-Stokes equations simultaneously, while segregated flow models solve the momentum equations independently and a predictor-corrector approach is used to link the solution variables together to satisfy the governing equations. STARCCM+'s user guide [72] suggests the segregated flow model in case of incompressible external

aerodynamics to save computational time. For this reason, the segregated flow model were used for the three cases in this thesis.

The turbulence model selected for all the three cases is the $k - \omega$ SST (Menter) [69] because of its long-time use within the aerospace industry, together with its better performances for solving complex body forces, which were expected in these simulations [75, 76].

In order to improve the initial conditions and speed up the convergence in the unsteady calculation with the sliding mesh approach (cases P and PD), a steady simulation using the MRF model was initially run until convergence. Furthermore, two key aspects for the convergence has been considered:

- the fixed high rotation rate of the propeller (6000 rpm). Using a very small time-step Δt at the beginning of the simulation would have meant an enormous amount of time to reach the convergency. Therefore, the time-step considered has been gradually reduced along with the simulation, with a final value of $8.333,3 \times 10^{-5}$ s, which correspond to a revolution of 3° per time-step;
- the number of iterations between advancements in time, called inner iterations, were varied along the simulation to ensure sufficient convergence within each time step.

The physics model used in the simulations are briefly reported in Table 4.1

	P, PD	AD
Turbulence Model	RANS + $k - \omega$ SST	
Flow Regime	Turbulent Flow	
Equation of State	Ideal Gas	
Solver	Segregated Flow Model	
Time-Dependent	Unsteady	Steady
Time-Step Size	$8.333,3 \times 10^{-5}$ s	–
Time Discretization	2^{nd}	–
Stopping Criteria	Thrust Convergence	
Additional Model	–	Virtual Disk

Table 4.1: *Physics parameters used in the simulations.*

4.5.1 Virtual disk model

In simulation AD a simplified model has been used to implement a propeller in STARCCM+: the Virtual Disk model. The actual geometry of the blades is not

resolved because the rotors are substituted by an actuator disk (Figure 4.7), where a momentum source is distributed. This choice permits a significant decrease of the computation cost and allows to evaluate of other methods to implement a propeller in STARCCM+.

There are currently three approaches available in STARCCM+ to model fans and propellers: Body Force Propeller Method (BFPM), Blade Element Method (BEM), and 1-D Momentum Method. The Body Force Propeller Method [72] was chosen for the case *AD*. The method employs a uniform volume force distribution over an open cylinder. The volume force varies with the radial direction, that distribution is given by:

$$f_{bx} = A_x r^* \sqrt{(1 - r^*)}, \quad (4.2)$$

$$f_{b\theta} = A_\theta \frac{r^* \sqrt{(1 - r^*)}}{r^*(1 - r'_h) + r'_h}, \quad (4.3)$$

$$r^* = \frac{r' - r'_h}{1 - r'_h}, \quad (4.4)$$

$$r'_h = \frac{R_H}{R_P}, \quad (4.5)$$

$$r' = \frac{r}{R_P}, \quad (4.6)$$

where f_{bx} is the body force component in the axial direction, $f_{b\theta}$ is the body force component in the tangential direction, r is the radial coordinate, R_H is the hub radius and R_P is the propeller tip radius. A_x and A_θ are constants given by:

$$A_x = \frac{105}{8} \frac{T}{\pi \Delta (3R_H + 4R_P)(R_P - R_H)}, \quad (4.7)$$

$$A_\theta = \frac{105}{8} \frac{Q}{\pi \Delta R_P (3R_H + 4R_P)(R_P - R_H)}, \quad (4.8)$$

where T is the thrust, Q is the torque and Δ is the virtual disk thickness.

Even though the force distribution input in the actuator disk (Eqs. (4.2)-(4.3)) depends only on the radius, the variation of the force distribution with angle θ is considered in the iteration process.

The computation of the body force components requires several user inputs. Indeed, to be able to model the propeller, a propeller performance curve is needed, which

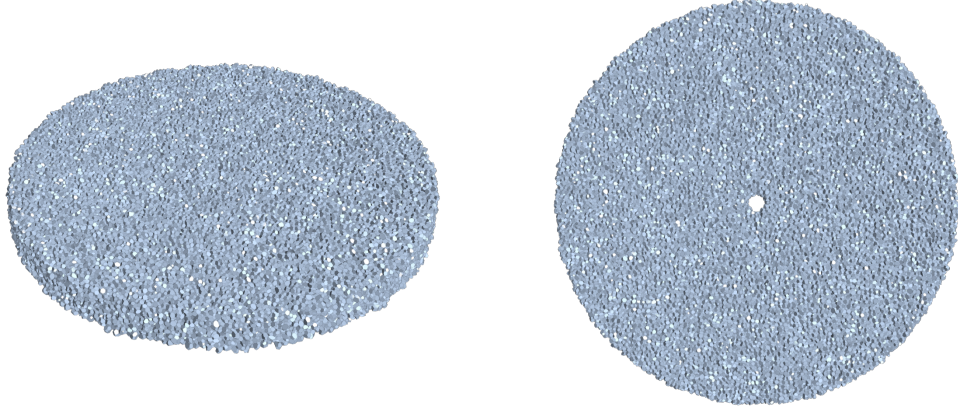


Figure 4.7: Visualization of the actuator disk by the polyhedral cells where the momentum source is added following the body force propeller method.

is usually defined by the following characteristics:

$$J = \frac{V_\infty}{nD}, \quad (4.9)$$

$$K_T = \frac{T}{\rho n^2 D^4}, \quad (4.10)$$

$$K_Q = \frac{Q}{\rho n^2 D^5}, \quad (4.11)$$

$$\eta = J \frac{K_T}{K_Q}, \quad (4.12)$$

where J is the advance ratio, K_T is the thrust coefficient, K_Q is the torque coefficient, η is the efficiency, V_∞ is the flow velocity, D is the propeller diameter, n is the rotation rate.

Further inputs are the position of the propeller within the computational domain, the direction of the propeller rotational axis, and the direction of rotation.

The simulation is performed for a certain operating point, which can be specified by either of n , T , Q . Considering the case of the operation point given by the rotation rate, the procedure for obtaining the body force component distribution over the virtual disk is the following:

1. the advance ratio J is calculated as:

$$J = \frac{V_\infty}{nD}; \quad (4.13)$$

2. the thrust coefficient K_T and the torque coefficient K_Q are interpolated from

the specified propeller performance curve:

$$K_T, K_Q = f(J); \quad (4.14)$$

3. with K_T and K_Q available, the thrust T and the torque Q are computed:

$$T = \frac{K_T \rho V_\infty^2 D^2}{J^2}, \quad (4.15)$$

$$Q = \frac{K_Q \rho V_\infty^2 D^3}{J^2}; \quad (4.16)$$

4. with T and Q available, the axial and the tangential body force components are calculated according to Eqs. (4.2)-(4.3).

In this thesis, the most reasonable choice in terms of propeller performance curve would have been the performance data of the model 9450 (the same used in case P and PD). Indeed, this would have allowed comparing results of case P and AD with each other, and with the experimental results [71]. However, the performance of a propeller with similar geometric characteristics to model 9450 (Figure 4.8) has been selected due to the unavailability of data for model 9450. The performance table of the APC 9x4.5 MR used for the BFBM has been reported in Appendix A. The operating point is given by the rotation rate, using the same rotation rate of case P and PD : 6000 rpm.

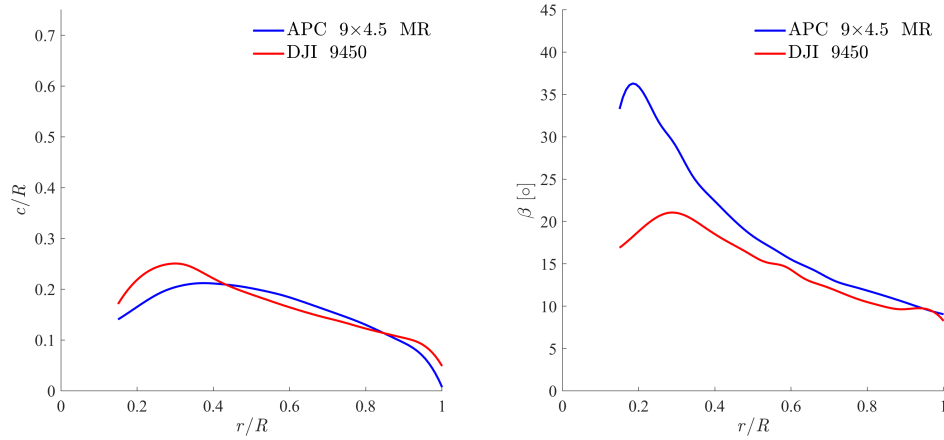


Figure 4.8: Comparison of the DJI Phantom 3 propeller and, the APC 9x4.5 MR.

4.6 Mesh generation

The meshing choices and the selected models considered for the three cases P , AD , PD were largely based on the recommended mesh settings section from the

STAR-CCM+ documentation on external aerodynamics [72]. Basically, the decision was between two different mesh models: an unstructured polyhedral mesh and a block-structured trimmed mesh. The final choice was supported on the presence of complicated curved surfaces in the cases P and PD (rotors and drone air-frame). Therefore, for the three simulations, a polyhedral mesh with a prism layer mesher was chosen for the whole domain. The decision to use the polyhedral mesh also for the simpler case AD has been investigated comparing the results obtained from the two types of mesh models mentioned above (Section 5.1.1).

The polyhedral mesh has been set following the recommendations found in the documentation, a grid convergence study (Section 5.2.1), and iterating based on post-processing visualization. The final mesh scheme’s default control values are reported in Table 4.2. Additional custom controls were applied to the mesh to achieve the desired mesh. The surface of the outer domain boundary is located far away from the source of motion, therefore a lower mesh resolution is needed to capture correctly the flow in these zones. For this reason, the surface of the outer domain boundary was set to have a target surface size of 43% of BS. Another custom control was applied to guaranteed accurate mesh along all surfaces within the domain (rotors and drone air-frame in the cases P and PD). Setting the target surface size value to 25% of BS, and the minimum surface size value to 15% of BS. All other settings within the default controls were left unmodified. The resulting mesh on the rotor and the drone air-frame surfaces can be seen in Figure 4.9.

Base Size (BS)	1 m
Target Surface Size	10% of BS
Minimum Surface Size	1% of BS
Surface Curvature	75pts

Table 4.2: Polyhedral mesh control values.

In order to capture the boundary layer and the near-wall flow, a prism layer grid is essential. Therefore, alongside the polyhedral mesh, orthogonal prismatic cells next to wall surfaces are generated. STARCCM+’s documentation [72] suggests that at least 10 – 20 layers are required in the cross-stream direction with greater numbers required for resolving the viscous sublayer. Considering the need to resolve the shear layer effectively for our simulations, $N = 20$ prism layer cells have been used, which results in a total boundary layer thickness of 1 mm. The cross-section prism layer cells along with the rotor and the drone air-frame surface can be seen in Figure 4.10.

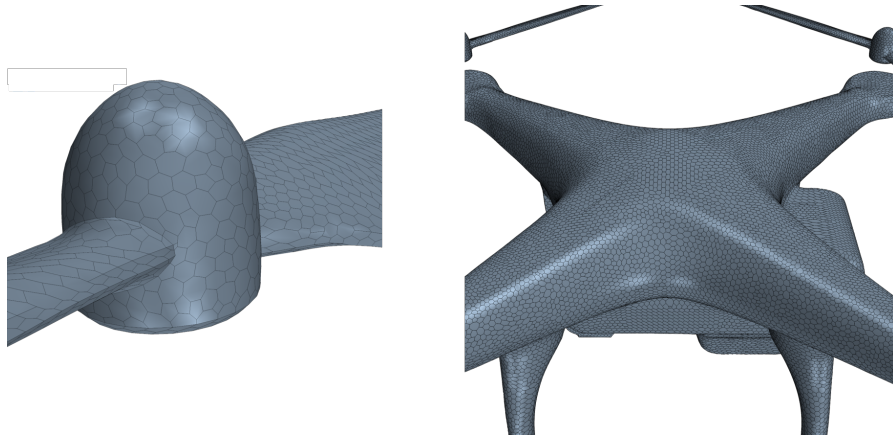


Figure 4.9: Final surface mesh. Left: details of the propeller surface mesh. Right: details of drone-airframe surface mesh.

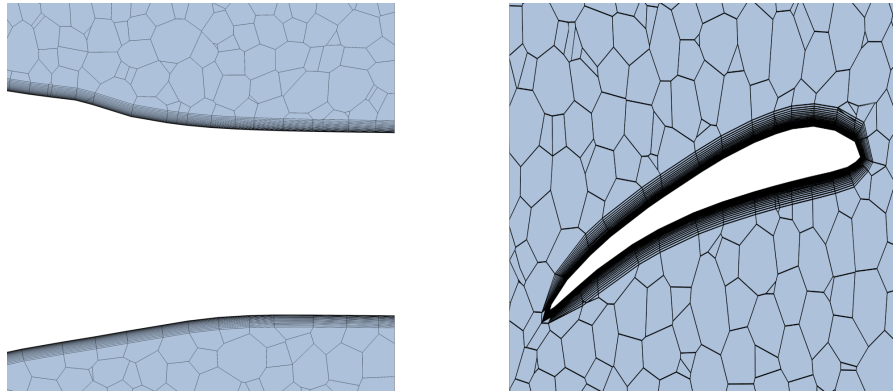


Figure 4.10: Prism layer mesh details. Left: drone arms boundary layer detail. Right: blade section boundary layer detail.

A very common refinement scheme among similar rotor simulations [77, 78] was the volumetric refinement, which is very simple to set up. For the three simulations considered in this thesis, the volume refinement region was a cylinder with different dimensions depending on the case. Therefore, using the volumetric refinement of case *PD* for both case *P* and *AD* would lead to a useless concentration of cells in regions where the flow is almost stagnant. Which means a needless loss of time. Following those considerations, the cylinder refinement region is a cylinder that begins $0.85D$ upstream of the rotor and ends $6D$ downstream, with a radius of $1.3D$ for cases *P* and *AD* (Figure 4.11) and with a radius of $1.5D$ for the case *PD*. The number of cells of the final mesh scheme of the three cases are reported in Table 4.3.

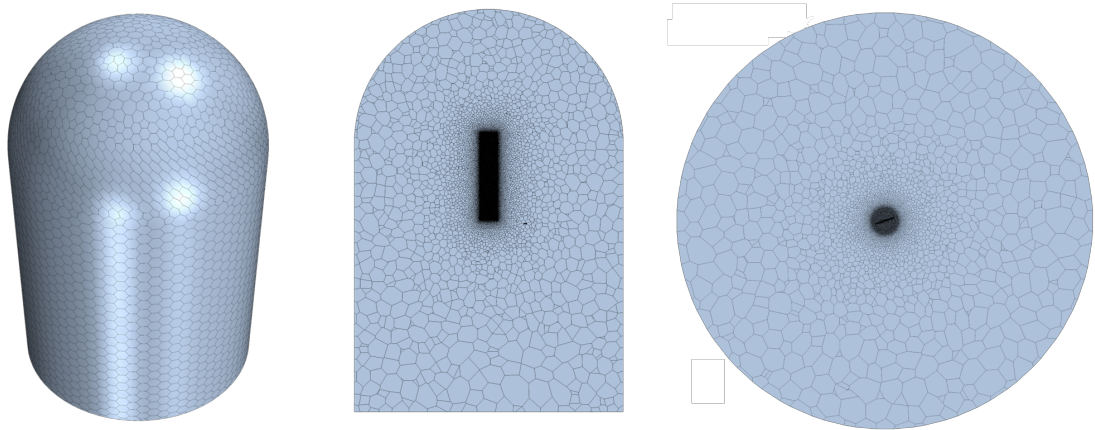


Figure 4.11: Final meshing scheme used for the fluid domain for cases *P* and *AD*. Left: external view. Center: midplane view through rotor plane. Right: topview through rotor plane.

	<i>P</i>	<i>AD</i>	<i>PD</i>
Total Cells	$8.5 \cdot 10^6$	$5.98 \cdot 10^6$	$3.05 \cdot 10^7$
Propellers Surface Cells	$4.6 \cdot 10^3$	-	$1.84 \cdot 10^4$
Drone Surface Cells	-	-	$2.92 \cdot 10^5$

Table 4.3: Cell number final mesh schemes.

4.6.1 Polyhedral and trimmed grid comparison

For simplicity, the same mesh model has been used for all three cases. However, in order to better understand the differences between the polyhedral and the trimmed mesh, the latter was also investigated for the simple case *AD*. To comprehend the results reported in Section 5.1.1, a brief resume of the main properties of the two mesh model was considered necessary [79].

The trimmed mesher utilizes hexahedral cells. The main advantage of the hexahedral cells is that they can be aligned with a specified coordinate system and that the grid works well with surfaces that are not well defined in the CAD model used to generate the surface. On the other hand, polyhedral grids are efficient and easy to build. The main disadvantage is that the grid quality is dependent upon the quality of the CAD. However, the reason that a polyhedral mesh was chosen for the three cases was caused by three important characteristics:

1. unstructured grids generation is faster with complex geometry;
2. many cell faces (and, hence, neighboring cells), leads to having a greater

number of optimal flow directions that can be computed with a single cell;

3. smoother growth away from the body, lead to a better estimation of aerodynamic coefficients

The two meshes scheme considered in Section 5.1.1 are reported in Figure 4.12

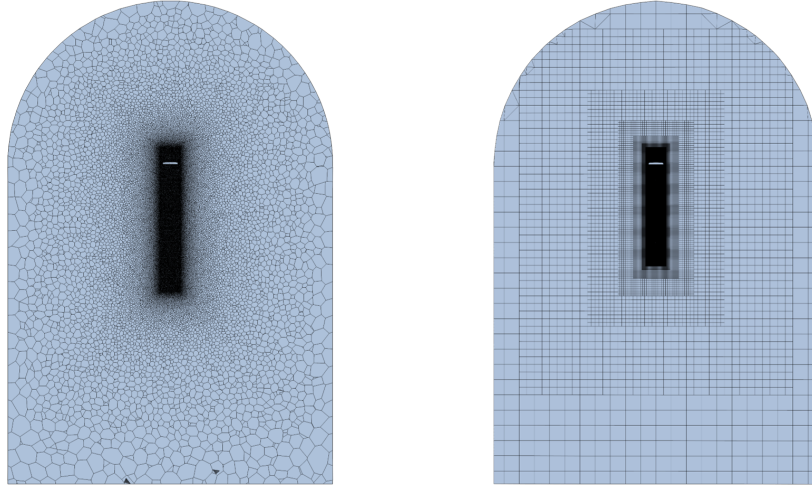


Figure 4.12: Midplane view through rotor plane of polyhedral mesh (left) and trimmed (right) mesh for case B.

4.7 CFD data extraction

The main aim of simulations P and PD is the data extraction needed for the implementation of the hybrid acoustic method. Indeed, once the simulations have been validated (Section 5.2.1), the acoustic analysis started from the CFD data. In Chapter 2 was described the methodology which has been implemented in Matlab and permit to compute the tonal noise at the different blade passing frequency considering a formulation made from the Ffowcs-Williams and Hawkings analogy. As seen, the inputs needed from the CFD simulation are only related to the position of the noise source and the forces operating on the surface of the rotating source. In order to apply the theory of Section 2.5.4, the surface of the blade must be divided into discrete radial sections. Indeed, one of the essential simplifications made by Lightill's analogy is based on the acoustical compactness of the source, which is not satisfied by the full propeller. In the remainder of this thesis, the different sections of the propeller will be referred to as "strips".

It must be noted that what will follow in this section is valid for both cases P and PD . The only difference belongs to the acoustic analysis, where the number of

propellers and the different orientations must be taken into account.

4.7.1 Accumulated force tables

Practically, the data needed from the CFD simulations are the values of the forces operating on the different strips and the coordinates of the center of those strips. STARCCM+ provided an in-built function, called "accumulated force tables", that allows extracting the force computed over a selected surface, dividing the surface into discrete intervals [72].

This function needs few simple inputs:

- the surface part where the forces are acting;
- the number of strips (or bands) across the part;
- a coordinate system in which the bin, force, and profile directions are defined;

The evaluated forces consider both pressure and shear forces contribution:

$$\sum_{faces} (\mathbf{f}_{faces}^{pressure} + \mathbf{f}_{faces}^{shear}) \cdot \mathbf{n}_{faces}, \quad (4.17)$$

where f and \mathbf{n}_f is related to the direction that indicates the direction decided by the users in which to compute the force. $\mathbf{f}_f^{pressure}$ and \mathbf{f}_f^{shear} is the pressure and shear force vectors on the surface face automatically calculated by STARCCM+.

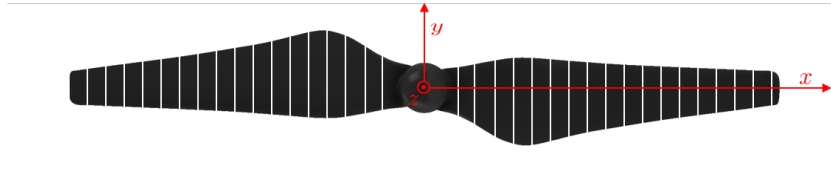


Figure 4.13: Example of blade stripping.

The propeller is divided along the span (x direction in Figure 4.13). Considering the reference system in Figure 4.13, the normal, the tangential, and the radial force are in direction z , y , and x , respectively. The normal and the radial force are always considered positive in the respectively positive axis direction. The drag force's positive direction, instead, depends on the rotating direction of the propeller.

The "accumulated force tables" function gives the position of the center of the strips along the x axes, in addition to the three forces. Then, considering that the reference system is attached to the body (so is rotating), we had the radial position of the strips in the reference frame centered on the propeller.

The data extracted will not consider the whole propeller, instead, the analysis formulation requires only one blade. Therefore, the data are extracted only for the strips present along the positive x direction. Furthermore, the number of strips represents a new parameter, whose effect on the tonal noise has been investigated (Section 6.1.2).

Chapter 5

CFD validation and results

In this chapter, the results obtained from the CFD analysis for the three cases P , AD , and PD are reported. The outcomes are divided into three sections, one per case. In order to validate the achieved results, the comparison between the data obtained and the data from previous works is reported in each section. Additionally, two different mesh studies have been done. For the case, P , the influence of the mesh size on the thrust has been investigated. For case AD , the influence of the mesh cell type has been explored.

5.1 Isolated actuator disk

The results obtained from the CFD setup of case AD described in the previous chapter are reported in this section. First of all, a comparison between two mesh schemes and the validation of the results are discussed. Afterward, a brief description of the flow field of the hovering of an isolated actuator disk is given. The study of the actuator disk case is a good starting point for the more complex simulations that will follow in this thesis. Indeed, it allowed us to study different mesh strategies and the most suitable domain shape to carry onto the next steps, and without demanding a lot of resources (steady RANS instead of uRANS).

5.1.1 Structured-unstructured grid comparison

A comparison between the polyhedral and the trimmed mesh scheme for the case AD is reported in this section. The aim is to justify the choices made behind the grid schemes discussed in Chapter 4.

The two mesh schemes considered in this analysis are reported in Figure 4.12. Because of the setting of the grids reported in Table 5.1, few comments can be done. The first noticeable difference between the two schemes is related to the

resolution of the mesh. Indeed, the schemes provide a similar overall number of cells (mesh size), but the polyhedral case results in cell size smaller locally (minor base size). Therefore, the polyhedral mesh should give more accurate solutions than the trimmed scheme with the same number of cells. On the other hand, the orthogonality and regularity of the structured trimmed mesh could result in improved convergence when the flow direction is aligned with one of the main grid axes, possibly justifying the use of fewer cells for a given level of accuracy. Therefore, the performance and the velocity field obtained from the two schemes have been compared to have a better understanding of the results produced by the two mesh schemes,.

	Polyhedral	Trimmed
Base Size (BS)	0.595 m	1.19 m
Target Surface Size	10% of BS	
Minimum Surface Size	1% of BS	
Mesh Size (Cells)	$4.21 \cdot 10^6$	$5.98 \cdot 10^6$

Table 5.1: Structured and unstructured mesh parameters for case AD (see Figure 4.12)

The velocity profile at different wake positions for the two mesh schemes has been reported in Figure 5.1. The results obtained show a good agreement between the two mesh schemes considered. Therefore, the fact that the trimmed cells are advantaged with cases where the flow is basically unidirectional, balance out the lower mesh resolution used. Furthermore, the agreement between the two simulations can be noticed also comparing the performances in terms of thrust T and torque Q . Table 5.2 backs up the results shown in Figure 5.1 reporting similar values of thrust T and torque Q .

	Thrust [N]	Torque [N·m]
Polyhedral	3.585	0.0582
Trimmed	3.583	0.0584

Table 5.2: Structured and unstructured mesh T and Q comparison.

In conclusion, both grids produce virtually identical thrust and torque values. Must be noticed that the achievement of virtual grid independence, implies that the grid used for the computation of the results for the case AD could be simplified into a coarser scheme.

In the continuation of this thesis, the next steps will be studied considering the polyhedral mesh, mainly for the reason of the presence of the elaborated geometries. Furthermore, especially for the case *PD*, the flow field should be characterized by many directions due to the presence of different interactions.

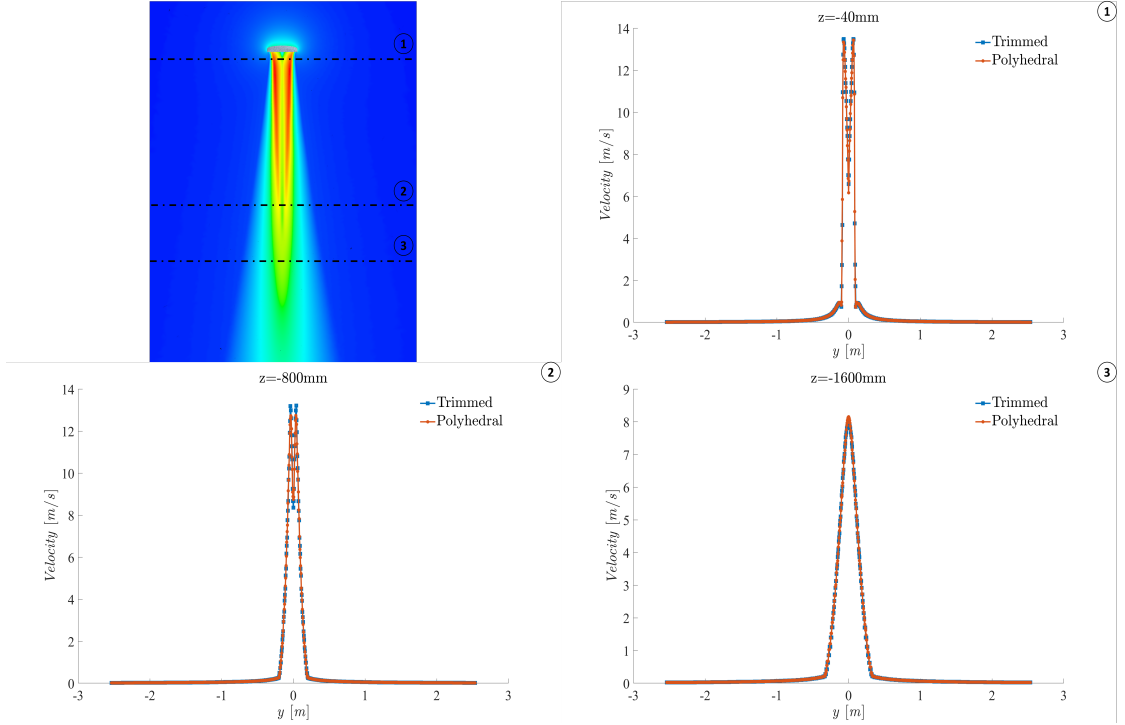


Figure 5.1: Structured and unstructured mesh schemes for case *AD* velocity field (top-left) and velocity profile comparison at $z = -40\text{mm}$ (1), $z = -800\text{mm}$ (2) and $z = -1600\text{mm}$ (3).

5.1.2 Validation of the virtual disk model for hovering configuration

The isolated actuator disk results were validated against computer-generated data of the reference propeller made by the manufacturer [80], and against experimental data [81]. Table 5.3 shows that the relative difference between CFD results and the compared measurements is below 4% for the thrust, setting of the good prediction made by the virtual disk model.

The deviation from the experimental data could be caused by different reasons. The most significant explanations could be related to the assumptions at the base of the virtual disk model (Section 4.5.1) and the input data used for the virtual disk model. Indeed, the performance table considered was not obtained experimentally but was

carried out by the manufacturer following the vortex theory, which is based too on some simplifications. However, the agreement between the data highlights the utility of the methodology implemented in the case *AD* when a first approximated computation of the performance of a propeller is required.

	Thrust [N]	Torque [N·m]
CFD	3.585	0.0582
Manufacturer Computational [80]	3.723	0.0607
Deters Experimental [81]	3.557	N/A

Table 5.3: Comparison of thrust and torque CFD results of case *AD* to manufacturer and experimental data [80, 81]

5.2 Isolated propeller

The results obtained from the CFD setup of case *P* described in the previous chapter are reported in this Section. First of all, the mesh convergence study and the validation of the obtained results are discussed in Section 5.2.1. Afterward, a brief description of the flow field of the hovering of an isolated propeller is given. Furthermore, the differences between the use of an actuator disk instead of the actual propeller have been emphasized putting in contrast case *P* and *AD*'s results.

5.2.1 Validation and verification of the isolated propeller simulation

The main objective of this thesis, the tonal noise computation, leads to the necessity of the convergence of the aerodynamic force components. Therefore, a mesh convergence study was performed to verify adequate mesh resolution used in the remainder of this work. This was performed by varying the target surface size of the volume refinement from 0.75% to 0.125% of the base size. This range of variation of the target surface size corresponds to grids constituted by 500 thousand and 16 million elements, respectively (see Table 5.4).

In order to validate the results, the performances obtained using the different grids are compared against experimental data [71]. The CFD output for thrust and torque both laid inside of the presented error bars (Figure 5.2), showing a good agreement with the results reported by NASA Ames.

A mesh of 8 million cells is chosen as the cornerstone of our study since it provides significant savings in computational time while offering acceptable results in terms

Mesh	Mesh Size (Cells)	Thrust [N]
M1	$1.61 \cdot 10^7$	4.5244
M2	$8.5 \cdot 10^6$	4.5028
M3	$1.45 \cdot 10^6$	4.4772
M4	$6.14 \cdot 10^5$	4.4576

Table 5.4: Grid size and predicted thrust.

of flow details captured. Indeed, the considered mesh resolves the thrust values within 5% of the fully-converged value. The results obtained have been considered a valid starting point for the acoustic analysis presented in Chapter 6. The final mesh scheme considered is shown in Figures 4.9, 4.10, 4.11.

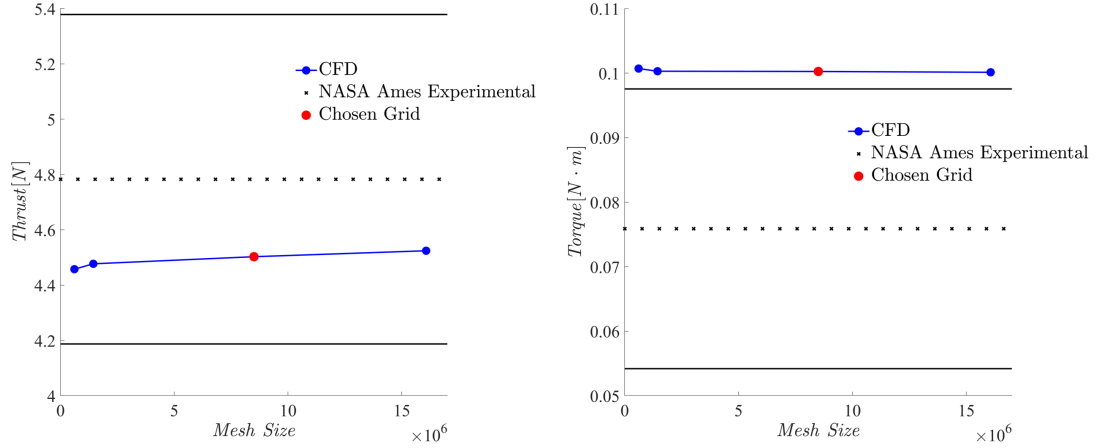


Figure 5.2: Comparison of thrust (left) and torque (right) CFD results to experimental data from NASA Ames [71] considering different mesh sizes. The horizontal levels indicate the confidence interval of 95%.

5.2.2 Flow field of an isolated propeller in hovering configuration

The performance data previously illustrated does not give any information about the flow structures. For this reason, velocity and vorticity magnitude plots are shown in this section. Those plots are compared with numerical results (Figure 5.3 and Figure 5.4) from Yoon & Diaz [76], who performed Detached Eddy Simulations on a much finer grid with 396 million cells (against the 8 million cells of our case).

Furthermore, the visualization of the flow field is a helpful approach to give a first understanding of the wake development of a propeller in hovering conditions. We can see general agreement in the flow behavior, despite that the fine-scale flow structure shown by Yoon & Diaz is not captured by the current results. This is attributed to the different computational methods considered.

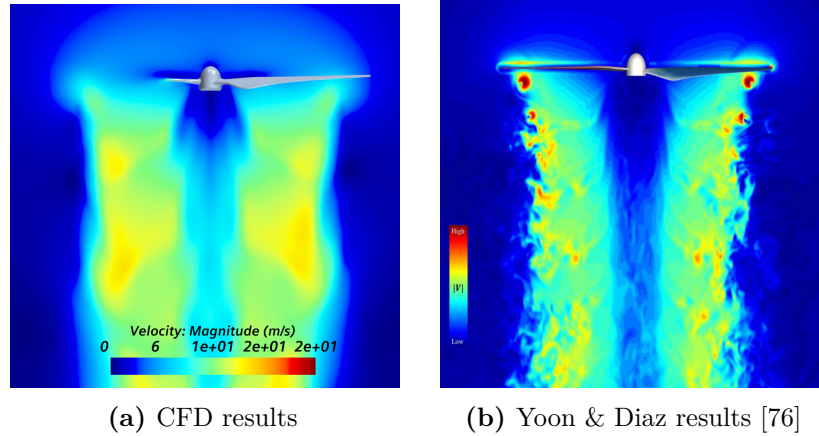


Figure 5.3: Velocity magnitude plot (a), compared with previous work (b).

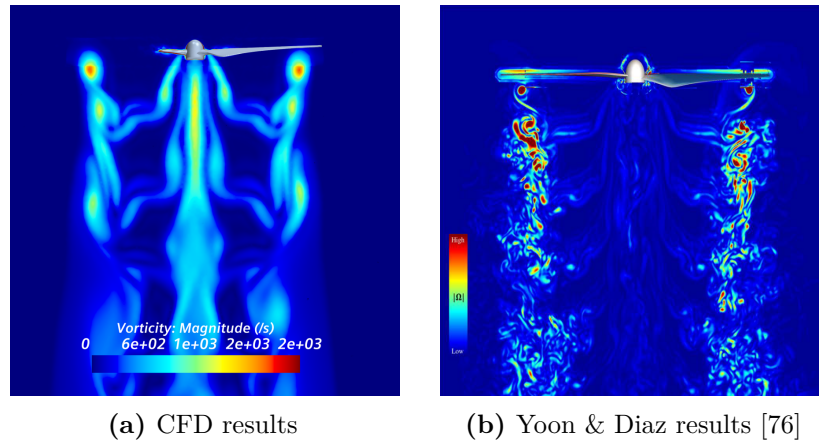


Figure 5.4: Vorticity magnitude plot (a), compared with previous work (b).

In conclusion, the use of the uRANS allows to both look at the general development of the wake, and to compute the aerodynamic forces needed for the acoustic analysis with good accuracy. Nevertheless, the saving in terms of computational time does not allow to show the smaller flow structures, such as the turbulent eddies or roll-ups at the edges of the wake presented in the results of Yoon & Diaz. However, the fine-scale flow structure is not the purpose of this study.

Further comments regarding the flow field related to a hovering propeller can be made considering the evolution of the turbulent kinetic energy (TKE) (Figure 5.5). The figure reveals that the vortices shed by the hub contain low levels of turbulence energy. Indeed, the peaks of the TKE are reached below the tip of the propeller, which was deducible from Figure 5.4, where the main contribution of the vorticity where located below the extremities of the propeller.

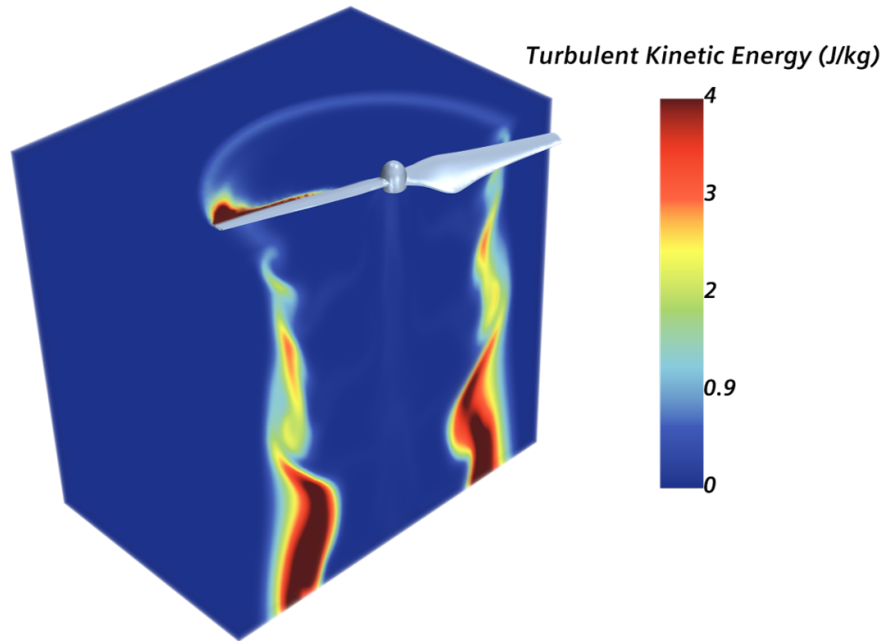


Figure 5.5: *Turbulent Kinetic Energy plot.*

A full view of the flow field is provided by Figure 5.6 where an extensive development of the wake can be seen. Although the uRANS is not a high-fidelity method, which can capture the vortex structures, can notice anyway that there is no phase shift between the velocity peaks and the corresponding vortex cores (which define the wake limits in Figure 5.6 (b)), a fact that may suggest the physical consistency of the solution. Moreover, the strong diffusion caused by the vortices is underlined by the TKE behavior in the regions located far away from the rotating plane (Figure 5.6 (c)).

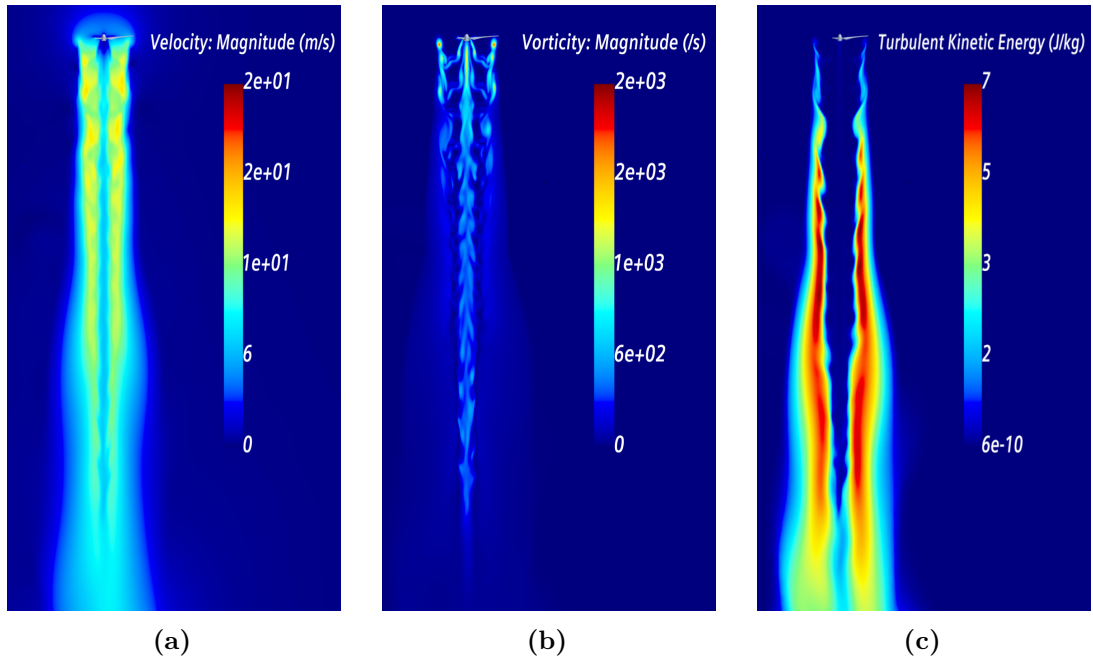


Figure 5.6: Full wake development representing by velocity magnitude (a), vorticity magnitude (b) and turbulent kinetic energy (c) plot.

5.2.3 Actuator disk and propeller flow field comparison

This section's purpose is to highlight the limits of the virtual disk model. Looking at the following paralleling between the two approaches must be taken in mind the geometries differences presented between the actual propeller, and the propeller implemented through the actuator disk. However, the qualitative comparison of the flow fields obtained from simulation P and AD could allow giving a first distinction of the two approaches. The velocity fields obtained from the two models have been reported in Figure 5.1 and Figure 5.4.

Slice sections are extracted from the velocity solution at different positions for the two considered cases (Figure 5.7). The rotating plane is marked as section a , and the distances of section $b-e$ to section a are $0.25R$, $0.5R$, $0.75R$ and R , respectively. Where the radius R considered is the radius of case P which is slightly bigger than the radius of the actuator disk (caused by the different propeller implemented in the virtual disk model).

Figure 5.7 (a)–(e) show vectors comparisons between case P (left column) and case AD (right column) at each slice sections. In the rotating plane (Figure 5.7 (a)) the presence of the actual rotating blades has great effects on the flow field of case P , and the vectors show a periodical distribution at the interval of 90° . On the other hand, the circumferential average treatment in the actuator disk model leads

to a different distribution of the vector for the case AD . Moving away from the rotating plane, the distribution of the vectors of case P tends towards case AD . Indeed the effect of the presence of the actual blade grows weak in the far-field. In figure 5.7 (e), which reports the section at a distance of one radius R behind the propeller, the plot from the two models looks very similar. That a consequence of the almost full development of the wake. Therefore, for the flow field that lies behind the propeller at a downstream distance greater than one radius of the blade, the actuator disk model can substitute the full blade model.

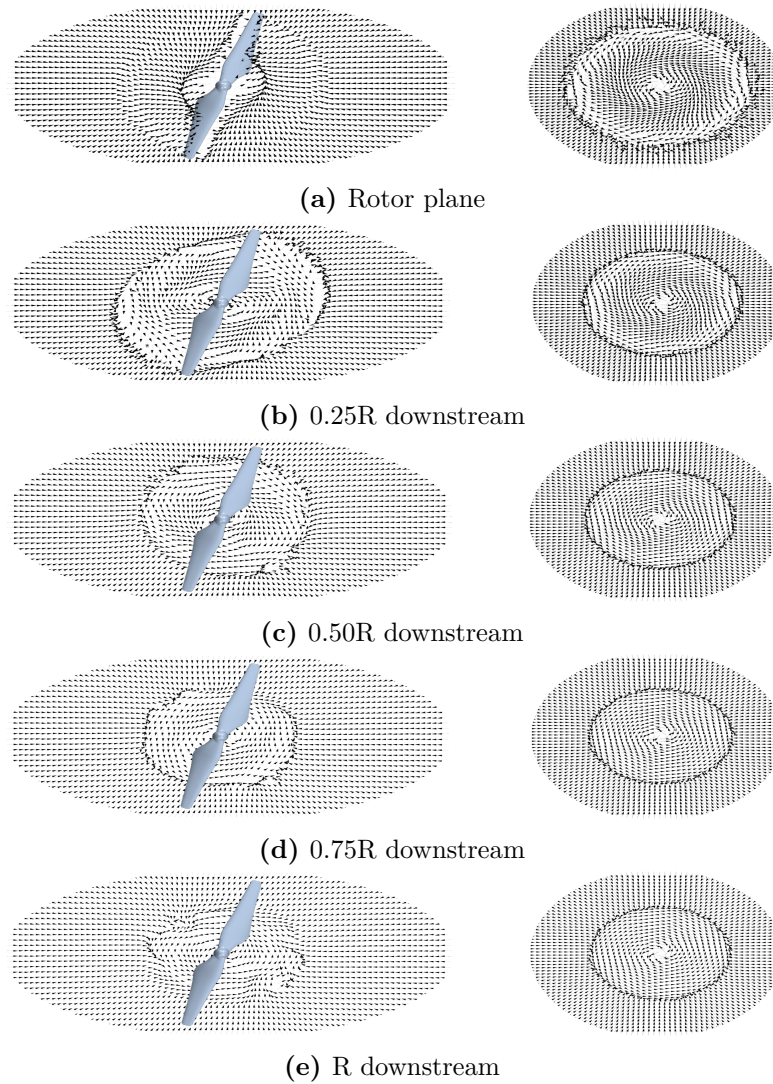


Figure 5.7: Comparison between the vector contours of case P (left) and PD (right) in different sections downstream.

5.3 Drone air-frame and propellers

A full quadrotor simulation is performed using the same RPM of case P to provide a data-set for comparison with the isolated rotor results. First of all, the simulation outputs are validated comparing to experimental data and literature works previously done. Successively, the flow field generated by the hovering configuration of a quadcopter is described. The main focus is given to the interaction of the propeller wake with the air-frame of the drone. As done in the previous section, the flow field obtained by other works is used as means to evaluate the accuracy of the current results presented in this section.

5.3.1 Validation of a full drone configuration in hovering

The thrust time-history behavior within a full period of rotation is reported against numerical data obtained by A. Thai [74] in Figure 5.8. Few differences between the numerical setup must best be kept in mind looking at the compared data: the rotation rate, the turbulence model, the grid resolution, and the different time-step. In order to make the comparison easier, the thrust is plotted against a non-dimensional time such as:

$$t^+ = \frac{t}{T}, \quad (5.1)$$

where T is the revolution period associated at the considered rotation rate (0.01 s for our case, 0.008 s for the 7000 rpm case).

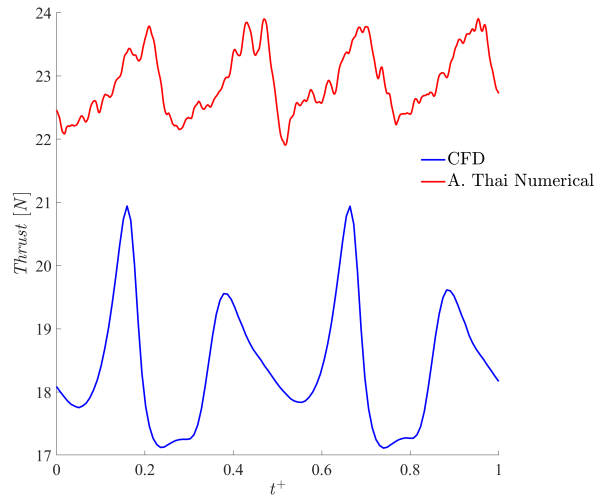


Figure 5.8: Thrust time-history comparison between case C and previous works [74].

The different magnitude order is caused by the bigger rotation rate [74] (7000rpm instead of 6000rpm), and the lower oscillation can be caused by the other factors mentioned above. However, the overall oscillating behavior caused by the presence of the interactions shows a good qualitative agreement. Indeed, the presence of the four peaks in the current results proves that the rotor-fuselage and rotor-rotor interaction effects (see Section 5.3.2) were properly characterized by the simulation. In order to give a validation of the magnitude of the performance computed, the mean values of the thrust are plotted against the values obtained by NASA Ames [71] (Figure 5.9). Can be noticed that the current results are well within the experimental uncertainty. Therefore, the reasonable magnitude and trend of the thrust obtained by this study seem to be an appropriate starting point for the acoustic prediction reported in Chapter 6.

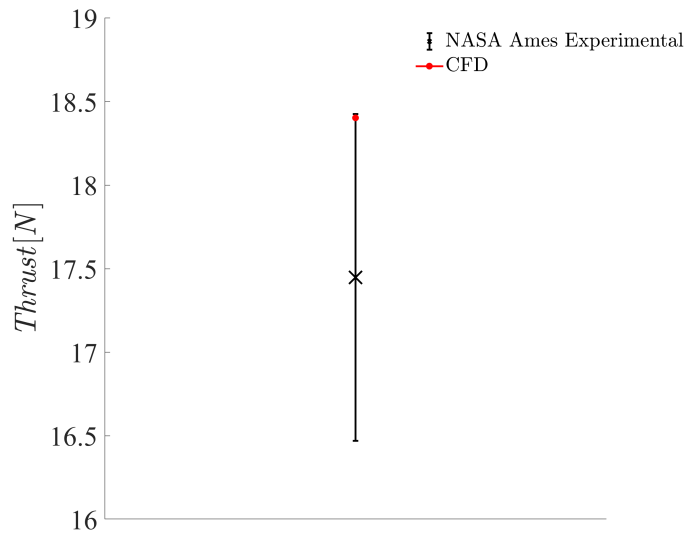


Figure 5.9: Comparison of thrust CFD results to empirical data from NASA Ames [71].

5.3.2 Quadcopter flow field: rotor-on-rotor interactions

The good agreement in terms of performances does not prove the level of accuracy in the prediction of the complex flow field developed by a hovering quadcopter configuration. In this regard, the flow expected from case *PD* will be different from the one observed in Section 5.2.2. Indeed, the interactions with other rotors and with the surface downstream the rotor, complicate the features of the wake structure.

The mentioned interactions can be first noticed considering the comparison between the thrust value obtained from case P and the mean value of a single propeller of case PD (Table 5.5). The lower value from the propeller in the quadcopter configuration could have been due to multiple different reasons. One of them is the rotor-rotor tip interaction, which has been widely studied in the literature [11, 10, 16], proving that the measured thrust for multi-rotor cases presents a little drop (2%) from the single propeller case when the relative rotor distance is less than $1D$. This conclusion suggests that this kind of interaction could be one of the sources of the oscillating behavior of the thrust observed in Figure 5.8.

Case	Thrust per propeller [N]
Single propeller	4.5
Multirotor propeller [80]	4.42

Table 5.5: Comparison of thrust value between isolated propeller (case P) and single propeller of the multi-rotor configuration (case PD).

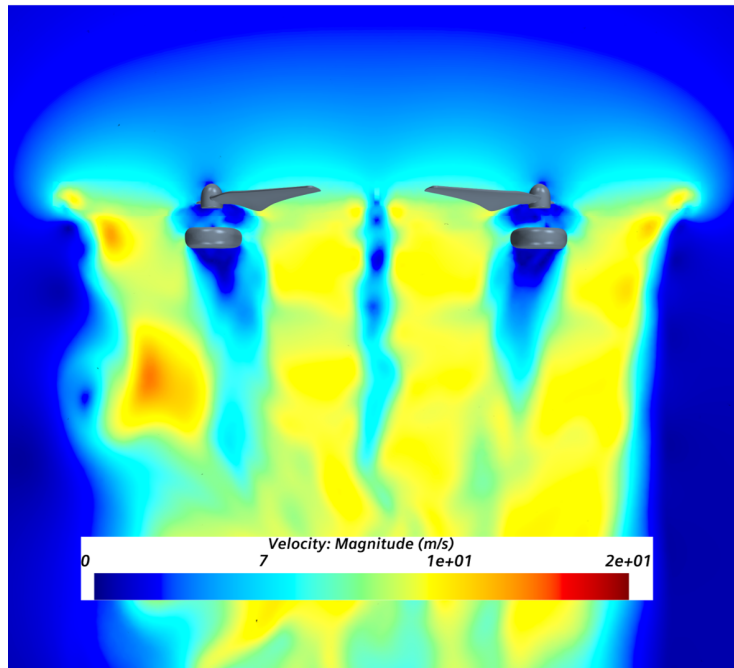


Figure 5.10: Velocity magnitude plot of a multi-rotor configuration.

The slight influence of the rotor-rotor tip interactions can be analyzed by the visualization of the flow field. In the region directly under the rotors, the velocity

field of the multi-rotor configuration (Figure 5.10) shows global features similar to the results found considering the isolated propeller (Figure 5.3). However, the trends of the two-rotors wake to tend to each other can be noticed, meaning that the simultaneous presence of more rotors yields a mutual interaction of the wakes. Other aspects related to the considered interaction can be seen by the visualization of the vorticity distribution and the turbulence kinetic energy. The main vortex structures of the rotors, the tip vortices, and the trailing edge vortex sheets, interact along with the development of the wake. Indeed, following the counterclockwise propeller wake (Figure 5.11 (a) right), the red circular spots, which correspond to trailing edge vortex sheets, coupled with the blue circular spots, which correspond to tip vortices belonged to the wake of the clockwise propeller wake (Figure 5.11 (b) left). The close distance between the rotors makes this strong interaction [16] source of a higher TKE level within the rotor interaction region (Figure 5.12 left red dots zone) than the ones presents in the single rotor case (Figure 5.12 right) at the corresponding region.

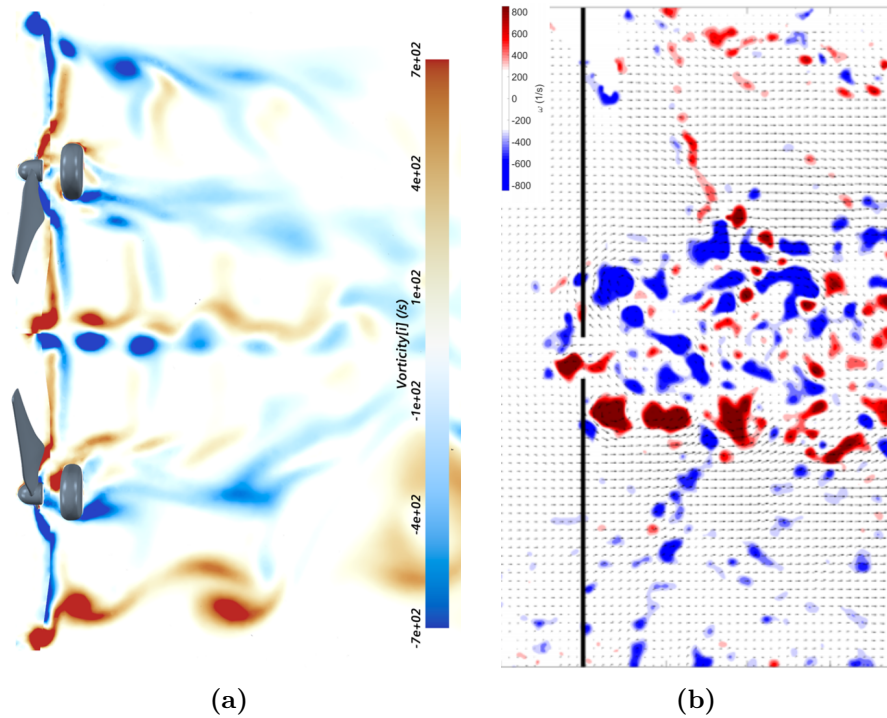


Figure 5.11: Vorticity distribution of a multi-rotor configuration: (a) CFD results (b) D. Shukla PIV results [82].

The results obtained by particle image velocimetry (PIV) from precedent works [82] has been reported in Figure 5.11 (b), to provide robust evidence that supports the results of case *PD* analyzed in this section. It can be noticed that the overall

CFD trends are in agreement with the experimental test, giving additional confidence that the CFD simulations are correctly representing the flow characteristics. Discrepancies are possibly caused, in part, by the motor and stand not being included in the simulation. Moreover, as mentioned several times, the models used in this thesis are not able to capture any turbulent details in the wake, which is not part of the final goal of this research.

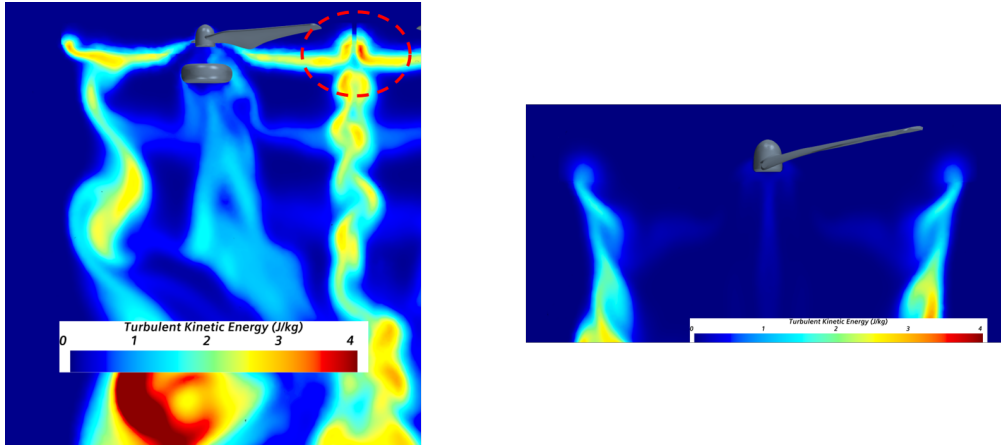


Figure 5.12: TKE magnitude plot of a multi-rotor configuration.

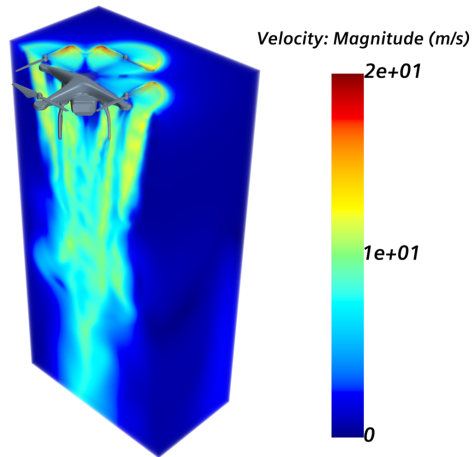
5.3.3 Quadcopter flow field: rotor-on-body interactions

Interactions between multiple rotors and the airframe will have also an impact on the aerodynamic performance. Indeed, different works show that a combination of flow reingestion, fuselage effect, and download, produce nonlinear effects on thrust production [12]. Indeed, the download component is one of the reasons that lead to the lower value of the thrust obtained for a single rotor reported in Table 5.5. The other mechanisms caused by the presence of the drone body are not subject of further study in this thesis, we limit ourselves to show the overall flow behavior of the full drone configuration, to add information to what has been said in Section 5.3.2.

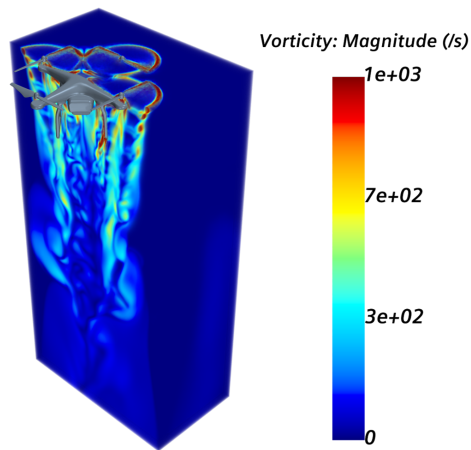
The velocity and the vorticity field in the symmetry plane of the drone air-frame are reported in Figure 5.13, from this picture, different considerations can be made:

- the rotor tip interaction is highlighted in the upper view of both Figure 5.13 (a) and (b);
- the wake interaction the landing gear can be easily noticed from Figure 5.13 (b), where a vortex shedding mechanism starts where the wake slam to the landing gear;

- the complex amalgamation of the vortices caused by the interaction of the four rotors wake;
- the interesting zones of high vorticity in the center of the top of the fuselage, where the rotor-tip passes, which could be an effect of the rotor-on-body interaction (Figure 5.13 (b)).



(a)



(b)

Figure 5.13: Full wake development of a full quadcopter configuration represented by velocity magnitude (a) and vorticity magnitude (b) plot.

5.4 Conclusion remarks

This chapter aimed to discuss and show the results obtained based on the numerical setup illustrated in Chapter 4. Furthermore, comparing the current results with previous works it has been useful for highlighting the limitations of the aerodynamic models presented in Chapter 3.

The steps followed to reach the multi-rotor simulation have been described in 3 sections:

1. The actuator disk simulation has permitted us to deal with the problems related to the choice of the most suitable shape and dimensions of the domain for the external aerodynamic problems. Moreover, the comparison between the structured and unstructured grid showed the potentiality of both the grids type for the kind of problems which this thesis is interested to examine. The choice for the continuation of the work is relapsed on the polyhedral grid for its adaptability to complex geometry;
2. The isolated propeller case showed that the proposed numerical setup allows predicting with good agreement the experimental data, and permit to have a first qualitative look to the flow field by the comparison with previous numerical works;
3. Based on the good results obtained by the single propeller case, we moved forward into the last simulation run, the quadcopter case. Considering the multiple interactions present between the rotors and with the drone surface and the wakes, the flow field comparison has been again only qualitative. Showing, a good level of agreement of the wake development from the tip-to-tip interactions. The main focus of the simulation was again on the performances, which drops inside the interval of values predicted by NASA Ames.

In conclusion, the reported results demonstrated that the presented aerodynamic model is sufficiently accurate as a basis of the acoustic analysis. Thus, the forces computed from the CFD results showed in this chapter will be implemented as the sources for aero-acoustic assessments following the theories described in Chapter 2.

Chapter 6

Acoustic results

In this chapter, the methods analysed in 2.5.1 will be used to compute the tonal noise generated by the isolated propeller of case *P* and by the full quadcopter configuration of case *PD* at different receiver positions. The analytical acoustic theory introduced in Chapter 2 defines the CFD input needed, which came from the results presented in Chapter 5. Therefore, the first aim of this chapter is to describe the methodology followed to post-process the STARCCM+'s outputs.

The acoustic model of the continuous array of phase-shifted dipoles (Section 2.5.4) and the approach used for the extraction of the aerodynamic forces (Section 4.7.1), implied the addition of two important parameters, whose effect could affect the presented results:

- the number of strips used for the subdivision of the surfaces of the blades (Section 4.7.1);
- the number of dipoles used in the continuous array approach (Section 2.5.4).

The choices of those parameters have been studied only for the simpler case *P*, the discussions are reported in Section 6.1.2 and Section 6.1.3, respectively.

Thereafter, the validation of the acoustic data of the two cases is presented, where the current results are compared against experimental outcomes obtained from previous works [83, 14]. In the end, a brief discussion of the tonal noise behavior emitted by the considered configurations is proposed.

The acoustic results reported in this section will be in terms of sound pressure level (SPL):

$$SPL = 20 \log_{10} \frac{p'_{rms}}{p_{ref}}, \quad (6.1)$$

where p_{ref} corresponds to 2×10^6 Pa is the reference value of the sound pressure and p'_{rms} is the sound pressure computed by the analytical noise theory. We will be

then able to analyze the pressure level of the sound (measured in dB) at different receiver positions.

Moreover, the two studied cases reported in this chapter consider only propellers rotating at 6000 rpm, which means that the blade passing frequency is $6000 \cdot 2/60 = 200$ Hz. Therefore, the tonal noise will be computed only at this frequency, and its multiples.

6.1 CFD post-processing and preliminary analysis

This section has to be considered as an introduction to the validation of the acoustic data. The process followed for the manipulation of the CFD data is summarily reported. Afterward, the study of the influence of the two parameters introduced previously is discussed.

6.1.1 Acoustic analysis input data elaboration

The input data for the tonal noise computation includes the position of the source and of the receiver in a fixed reference frame, the rotation rate of the propeller, and the three forces components in the frequency domain. Considering that the receiver position is arbitrary, and the radial position from the center of the propeller is directly given by the STARCCM+'s tool, the only pre-processing for the acoustic analysis regards the three force components.

The forces are extracted from each strip at every time-step by STARCCM+. In other words, the time history of the three force components is available (Figure 6.1 right). However, as described in Chapter 2, the noise computation is performed in the frequency domain instead of the time domain. For this reason, the fast Fourier transformation (FFT) has been computed along with the time evolution of the forces (Figure 6.1 left). Finally, the obtained complex forces represent the inputs used for the noise computation in the continuous of the thesis.

Must be noted that the Fourier spectrum of the axial force has been obtained by averaging the spectra computed for each individual propeller rotation (shown in red squares in Figure 6.1 left).

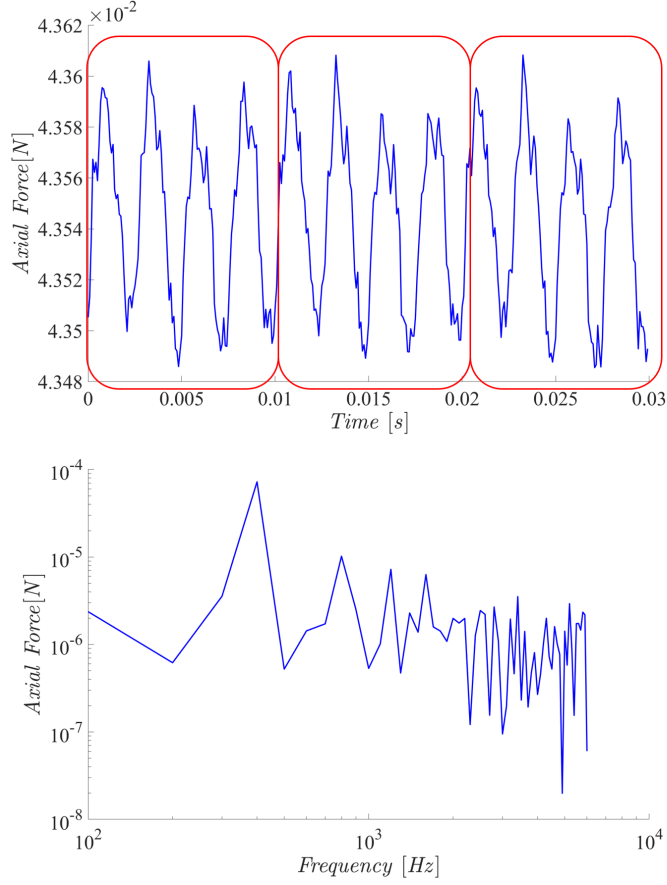


Figure 6.1: Case P force post-processing example considering the propeller surface divided in 120 strips. Left: time-history of the axial force of a single strip. Right: Fourier spectrum of the axial force of a single strip.

6.1.2 Number of the strips convergence study

The subdivision of the blade surface in different strips was a necessary step to reach the acoustic compactness of the source. Therefore, the correct number of strips to use for the continuation of the chapter need a detailed analysis.

Considering that the choice of the number of dipoles used to simulate the rotation of the source is addressed to the next section, for a first approximated analyses a number of 361 dipoles seemed reasonable. The study of the convergence of the SPL has been considered for different receiver positions (Figure 6.2) varying the number of strips used to divide the blade surfaces. The three receivers are located on a section perpendicular to the rotation plane of the propeller at three different polar angles ($\theta = 0^\circ$, 90° and 180° at a distance of 1.2 m from the center of the propeller). Considering the results plot in Figure 6.3 can be noticed that for the three cases

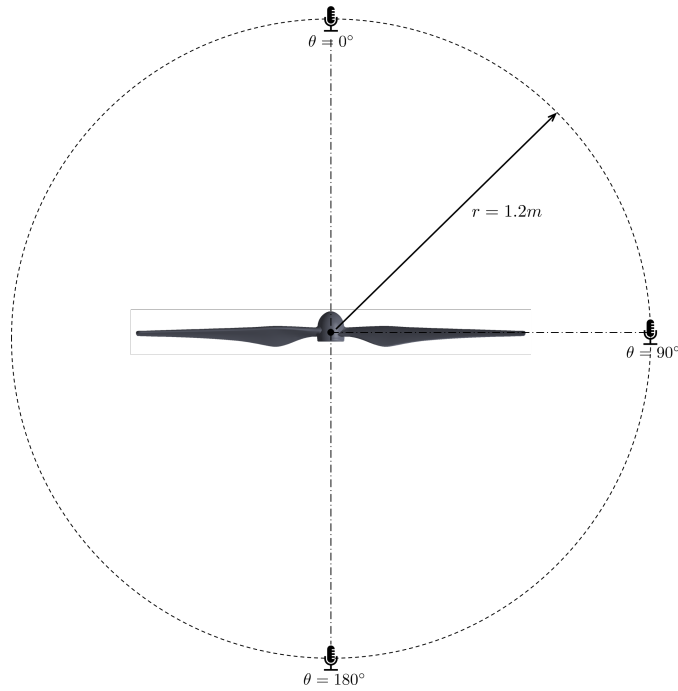


Figure 6.2: Diagram of microphone locations considered for the strip convergence study. (Diagram not to scale).

studied, a convergence of the values of the SPL has been reached. Therefore, for the isolated propeller case, a division of the blade surface with a number of strips bigger than 4 would ever lead to a similar value of the SPL computed. Thus, hereinafter the number of strips used for the isolated propeller case is fixed at 5. On the other hand, for the *PD* cases the number of strips has not been investigated. However, considering the more complex flows involved, the simulations were initially run with 69 strips. Indeed, the observations in this paragraph show that this number is sufficient to achieve converged SPL results.

Note that a preview of the noise behavior of a propeller has been given by Figure 6.3. Indeed, we can see that a propeller is louder for a receiver located at height of the rotating plane instead of under/over it. This will be further discussed in this section and it's principally caused by one of the basic assumptions made by the used formulation: only the dipole contribute is considered.

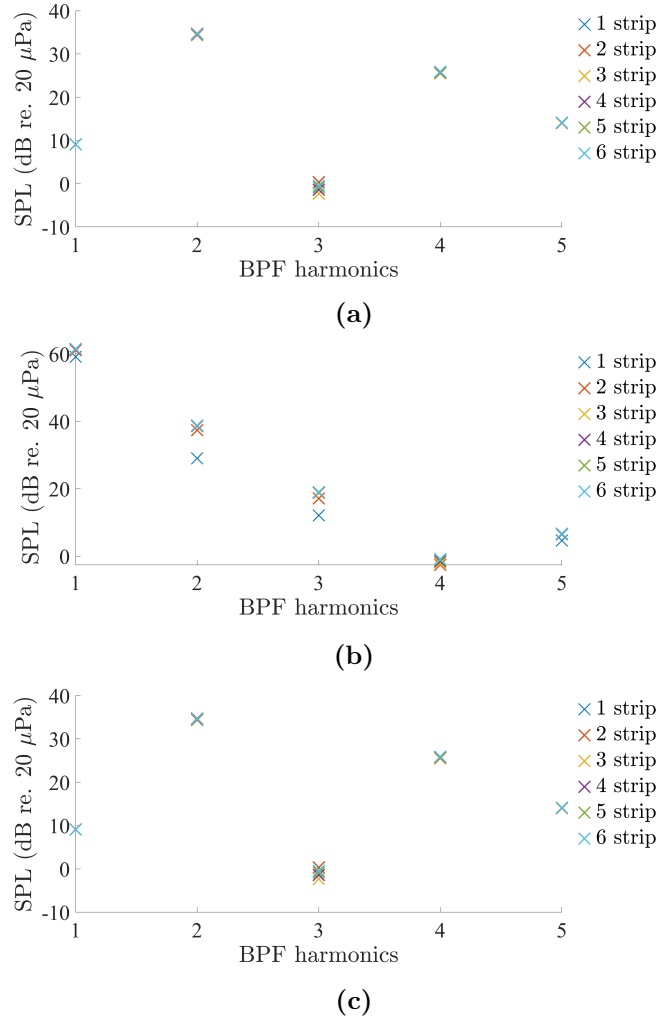


Figure 6.3: Sound pressure level considering different number of strips at different receiver positions. (a) above the rotor (b) rotation plane (c) below the rotor.

6.1.3 Number of the dipoles convergence study

In the continuation of the thesis, the procedure followed for the computation of the tonal noise considers the formulation of the continuous dipoles array reported in Section 2.5.4. However, before proceeding with the validation of the obtained results against experimental data, a study of the number of phase-shifted dipoles needed to emulate the rotation of the source is necessary. For this reason, a comparison of the emitted noise computed by the three models described in Chapter 2 is reported in this section.

Figure 6.4 (a),(b) report the sound pressure level computed from the acoustic

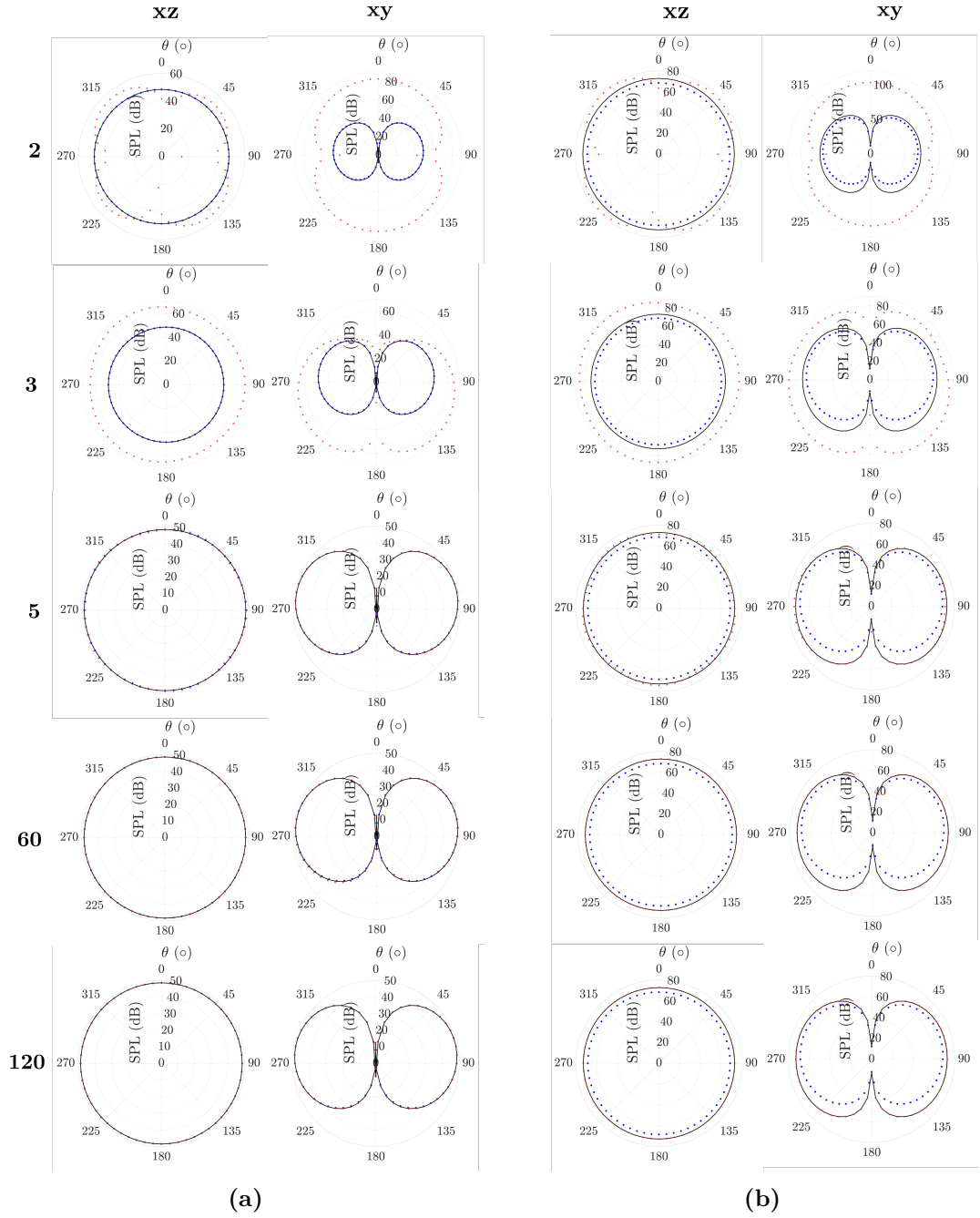


Figure 6.4: Comparison of the free-field directivities of the isolated propeller in its far-field (a) and near-field (b) at the first BPF. Different number of dipoles are used in the formulation (2.96). Blue dot symbols (solution Eq. (2.82)), black solid line (solution Eq. (2.91)) and red cross symbols (formulation (2.96)).

pressures obtained from Eq. (2.82) (far-field solution), Eq. (2.91) (near-field solution) and Eq. (2.96) (circular array of phase-shifted dipoles), represented by blue dot symbols, black solid line, and red cross symbols, respectively. A first comparison is made in the acoustical far-field of the propeller. Figure 6.4 (a) shows the directivity at the first BPF on the xy and xz planes (represented in Figure 6.6) at a distance of 5 m. The number of dipoles used in Eq. (2.96) is changed in order to see when the convergence is reached. The three solutions converge in the far-field since the near-field terms are negligible. Qualitatively, can be seen that the convergence is satisfied employing at least 40 fixed point dipoles.

A second comparison is performed in the acoustical near-field of the propeller (Figure 6.4 (b)). In this case, the observers are located at a distance of 0.5 m. One more time can be seen that the convergence is satisfied employing at least 40 fixed point dipoles. Important evidence of the different formulations can be now seen. Indeed, solution Eq. (2.91) and solution Eq. (2.96) converge at the near-field of the propeller. However, a deviation is observed with the solution Eq. (2.82). This difference can be addressed to the effect of the far-field approximation used to obtain Eq (2.82) (Section 2.80).

In order to get a better understanding of the influence of the number of dipoles, a quantitative study of the variation of the SPL with the number of dipoles for two receiver positions is now considered. The following parameters have been introduced:

$$\eta_n = \frac{SPL_n}{SPL_{fix/near}}, \quad (6.2)$$

$$\varepsilon_n = \frac{\eta_{n+1} - \eta_n}{\eta_n} \cdot 100, \quad (6.3)$$

where the subscript n refers to the number of dipoles considered, and the subscript fix or $near$ is the reference value obtained from Eq. (2.82) or Eq. (2.91) when the computation is done in the far-field or the near-field, respectively. Therefore, Figure 6.5 shows that increasing the number of the dipoles over approximately 65 dipoles, would lead to values of ε_n lower than 0.1% for both far-field (Figure 6.5 (a)) and near-field (Figure 6.5 (b)). Moreover, from Figure 6.5 can be noticed that the estimation of the acoustic pressure on the plane xz requires a higher number of dipoles to reduce ε_n .

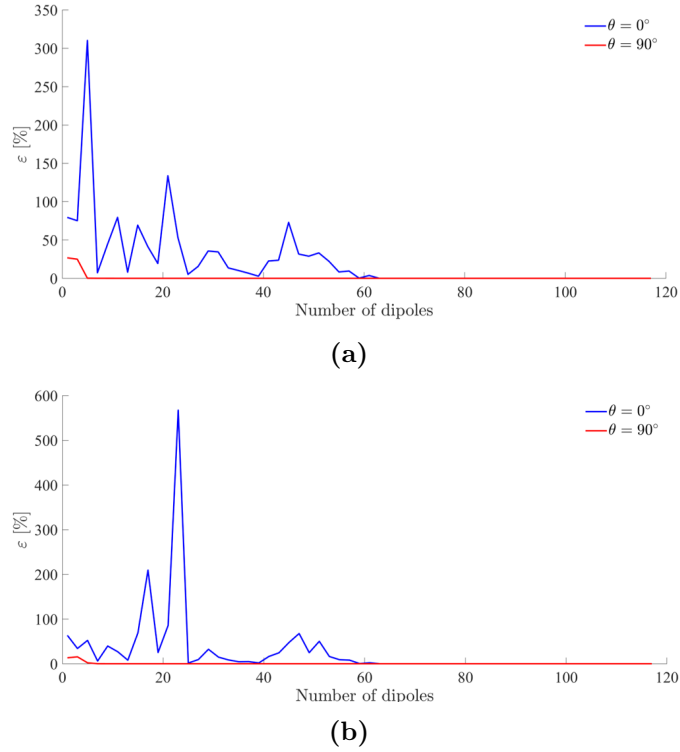


Figure 6.5: Comparison of the free-field normalized sound pressure level of the isolated propeller in its far-field (a) and near-field (b) at the first BPF. Different number of dipoles are used in the formulation (2.96).

6.2 Validation of the tonal noise computation methodology

In this section, the SPL of case P and PD are validated against experimental data [83] at different receiver positions are compared. The current results are obtained following the study reported in Section 6.1.2 and Section 6.1.3. Therefore, the blade surface is divided into 5 and 69 strips for case P and PD , respectively, and 65 dipoles are used to represent an equivalent propeller source using formulation (2.96).

6.2.1 Isolated propeller case

The isolated propeller acoustic results are validated against both experimental and numerical data [83], comparing the tonal noise at the different harmonics of the blade passing frequency and considering different receiver positions (Figure

6.6). However, a foreword is necessary: the experimental data consider a propeller rotating at 5300 rpm, which is slightly lower than the rotation rate of case *P* (6000 rpm). Therefore, in order to compare the data, the following formula has been considered:

$$SPL_{scal}(f_{scal}) = SPL_{ref}(f_{ref}) + 40 \log \left(\frac{N_{scal}}{N_{ref}} \right), \quad (6.4)$$

where the subscript '*scal*' is referred to as the value at 6000 rpm and the subscript '*ref*' is referred to as the value of the SPL at 5300 rpm. Eq. 6.4 is an empirical formula [84], that permits to compute the SPL at a specific rotation rate (N_{scal}) knowing the SPL at a known rotation rate (N_{ref}). The bigger constraint is that N_{ref}/N_{scal} must be close to one, which is respected by our case (~ 0.9).

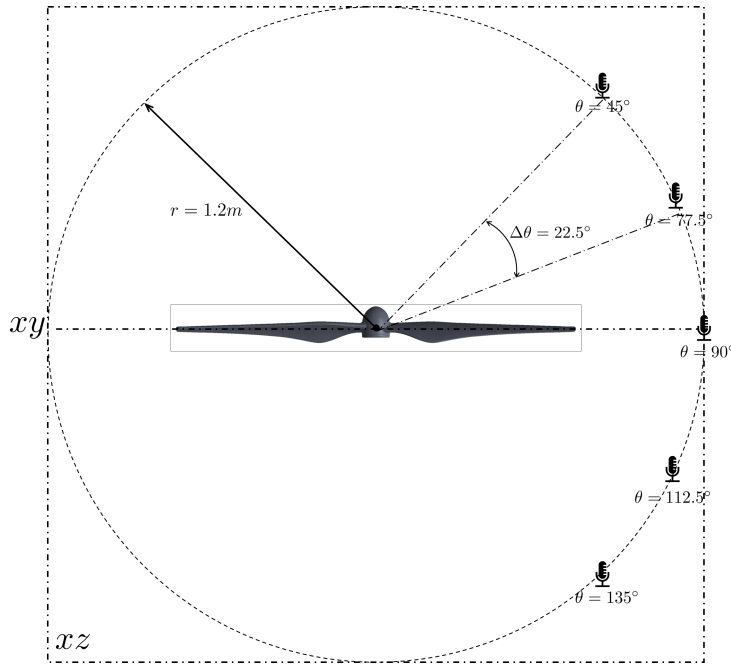


Figure 6.6: Diagram of microphone locations considered for the validation of the CFD results against experimental and numerical data [83]. (Diagram not to scale).

Figure 6.7 reports the comparison of the SPL at the BPF for the five receiver positions represented in Figure 6.6. We can see that the methodology followed in this thesis lead to a satisfying agreement of the results with the data from the literature. The best concordance between the results is reached at $\theta = \pm 45^\circ$, and the bigger discrepancy is reached at the level of the rotation plane ($\theta = 0^\circ$). However, the maximum error committed is below 3 dB, highlighting the accuracy of the followed methodology for the prediction of the tonal noise at the first BPF at different receiver positions.

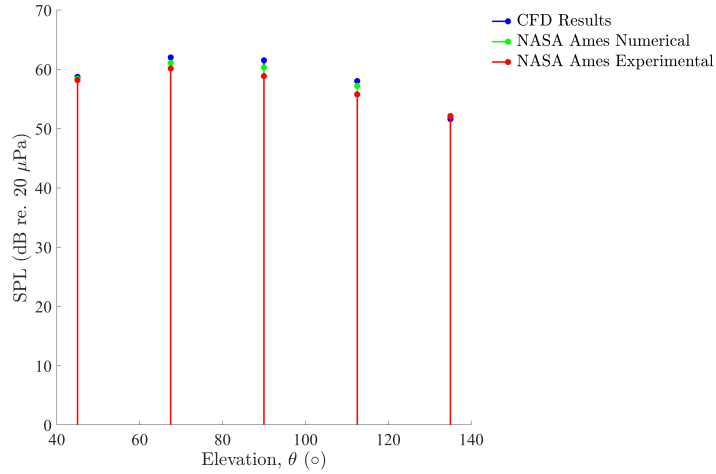


Figure 6.7: Comparison of the sound pressure level at the BPF of the isolated propeller between the CFD results and both numerical and experimental data from literature [83]. Radial position of the listener: 1.2m. Five elevation angles considered: $45^\circ, 77.5^\circ, 90^\circ, 112.5^\circ, 135^\circ$.

Consolidated the strength of the method for the prediction at the first BPF is necessary to verify the goodness of the SPL's estimation at a higher frequency. Therefore, the current results are compared against the experimental and numerical data [83] considering different harmonics of the BPF. Figure 6.8 reports the comparison for two elevation positions ($\theta = 90^\circ$ top, $\theta = 112.5^\circ$ bottom). The validation shows that the current methodology is able to predict with good accuracy only the first and the second harmonics of the tonal noise. However, at the rest of the BPF harmonics, the predicted noise levels do not match as well. The reasons related to the consistent discrepancy can be addressed to the basis of the used formulation, which considers only the dipoles contribution. A deeper investigation of the causes is left to future work. Nevertheless, the optimum behavior at the first (seen also in Figure 6.6) and at the second harmonics (maximum under-prediction of approximately 4 dB), allows using the current methodology for the prediction of the tonal noise at the higher frequencies.

Must be noted that the current results show similar behavior to the reference numerical results [83]. Particularly, the current results present an additional underprediction of the experimental results, which is prevalently related to the accuracy of the method used for acoustic propagation. Indeed, the reference numerical data are not obtained considering only the dipole contribution in the Ffowcs-Williams and Hawkings equation.

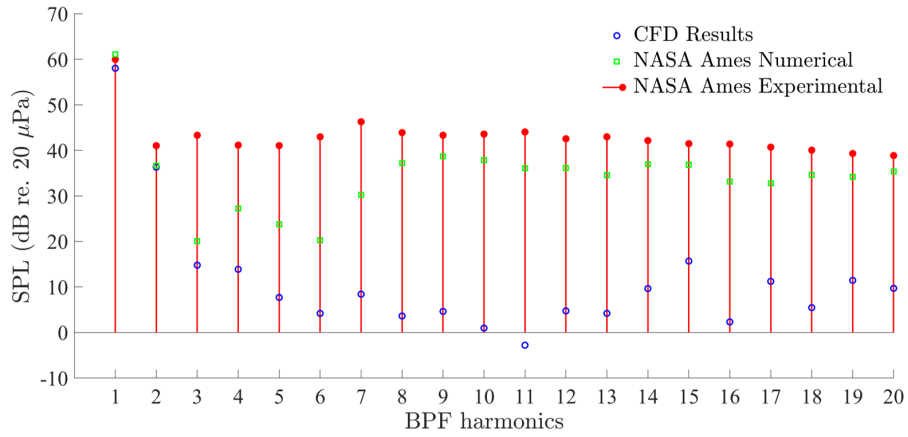
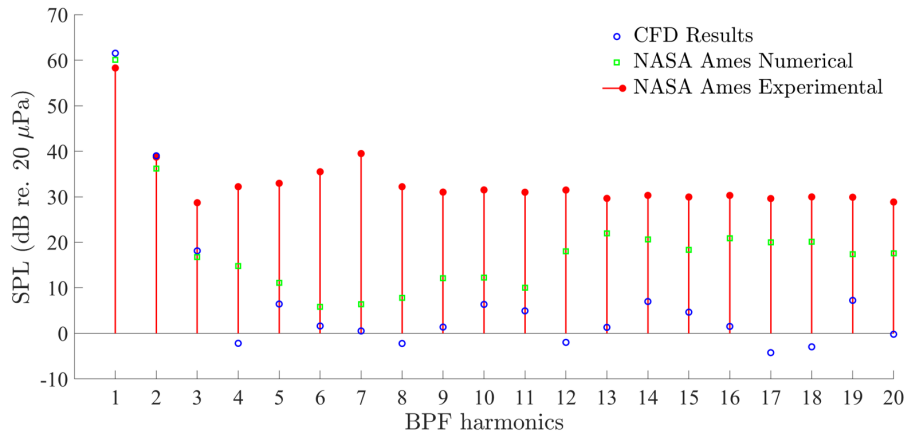


Figure 6.8: Comparison of the sound pressure level at the first twenty BPFs of the isolated propeller between the CFD results and both numerical and experimental data from literature [83]. Radial position of the listener: 1.2m. Two elevation angles considered: 90° (top) and 112.5° (bottom).

6.2.2 Quadcopter case

The quadcopter acoustic results are validated against experimental data [14], comparing the tonal noise at the different harmonics of the blade passing frequency considering the receiver position reported in Figure 6.9. Must be noted that the reference paper [14] reports the PSD of the SPL evaluated at the receiver position instead of the SPL. Therefore, the experimental data in Figure 6.10 are obtained shifting the PSD considering the frequency resolution used by Intarattep et al. [14].

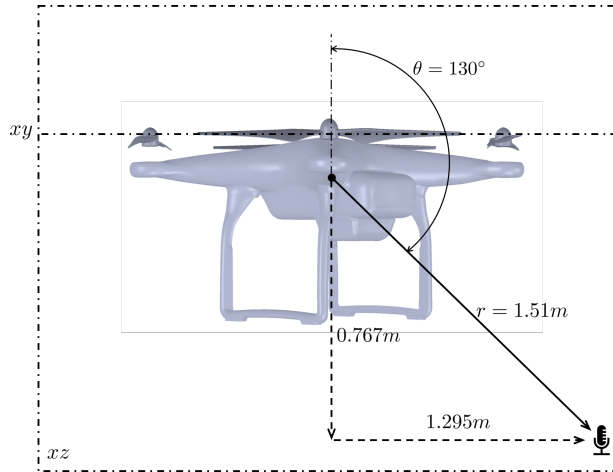


Figure 6.9: Diagram of microphone locations considered for the validation of the CFD results against experimental data [14]. (Diagram not to scale).

The comparison of the tonal noise computed by the current methodology with the experimental results shows a good agreement at the first 3 BPFs (Figure 6.10). Indeed, within this interval of frequencies, the maximum discrepancy reported is approximately 3.5 dB.

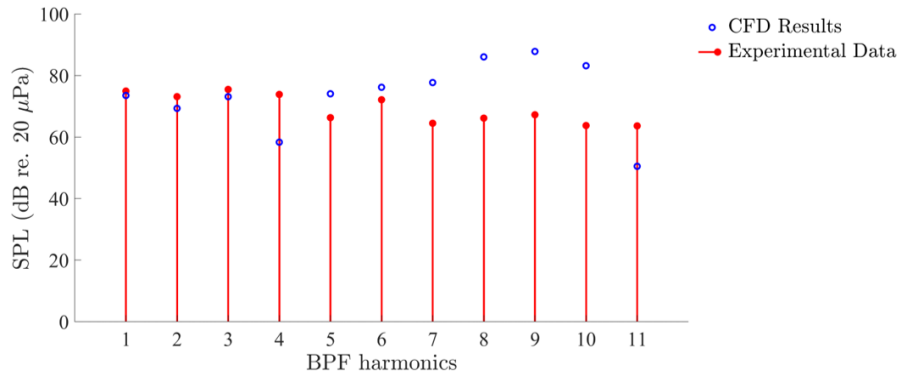


Figure 6.10: Comparison of the sound pressure level at the first eleven BPFs of the quadcopter configuration between the CFD results and experimental data from literature [14]. Radial position of the listener: 1.51 m. Elevation angle considered: 130°.

A second comparison has been made, in order to emphasize the ability of the current methodology to predict the emitted sound by multi-rotor configuration. Due to the lack of similar works founded in literature, the only reasonable comparison that could have been made is related to a qualitative paralleling between the directivity plots obtained from cases that present slight differences. Indeed, looking at the following comparison few things must be taken in mind:

- the propeller used in the reference case is different (DJI 9450 vs. DJI 9443), anyway, the two are comparable from an acoustic point of view considering literature works [14];
- the rotating rate of the propellers is different (6000 rpm vs. 5400 rpm);
- the distance between the tips of adjacent rotors (22 mm vs. 48 mm);
- the reference case reports the overall sound pressure level (OSPL) instead of the SPL.

However, the aim of this comparison is to visualize the goodness of the present methodology in the prediction of the directivity plots when a multi-rotor configuration is present and not to validate the current results (partially done in Figure 6.10). Thus, the comparison reported in Figure 6.11 considers numerical data [9] obtained using the nonlinear vortex lattice method (NVLM). The observers are located in section xz (Figure 6.9) at a radial distance of approximately 1.907 m (16R) from the center of the vehicle. Discarding the values (that are different for the reasons described previously), the shape assumed by the directivity plot obtained from the current results show good agreement with the reference data [9]. Therefore, we can be optimistic on the capacity of the current methodology to predict the noise at different receiver positions further than predict it for different BPFs.

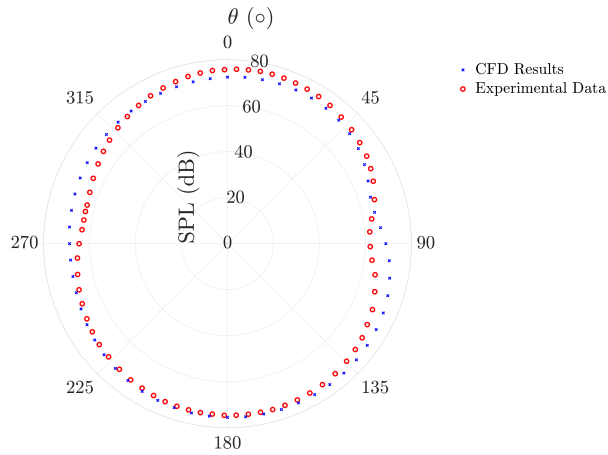


Figure 6.11: Comparison of the free-field directivities of the quadcopter configuration with numerical results [9]. Receivers at a radial distance of approximately 16R on plane xz .

6.3 Multi-rotors noise field characterization

In this section, the acoustic results previously validated are used to describe briefly the radiated noise pattern generated by propellers. Furthermore, the comparison between the results of case P and PD allow to highlight the effect of the interaction between the rotors and the drone air-frame on the tonal noise.

6.3.1 Isolated propeller noise pattern

The radiation pattern of the isolated propeller on the axis plane reported in Figure 6.12 shows the pattern typical of a compact dipole (steady loading sources). Indeed, the two characteristic symmetric lobes are presents, which highlight the presence of the highest tones at the height of the plane of rotation and the lower along the rotation axis.

The effect of the high frequencies can be seen in Figure 6.13. The loss of the acoustic compactness, caused by the increase of the importance of the scattering phenomena, leading to more complicated directivity patterns. Moreover, it can be noticed a consistent decrease in terms of the magnitude of the acoustic pressure with the increasing of the frequencies, underlying that the louder tones are present at the lower frequencies.

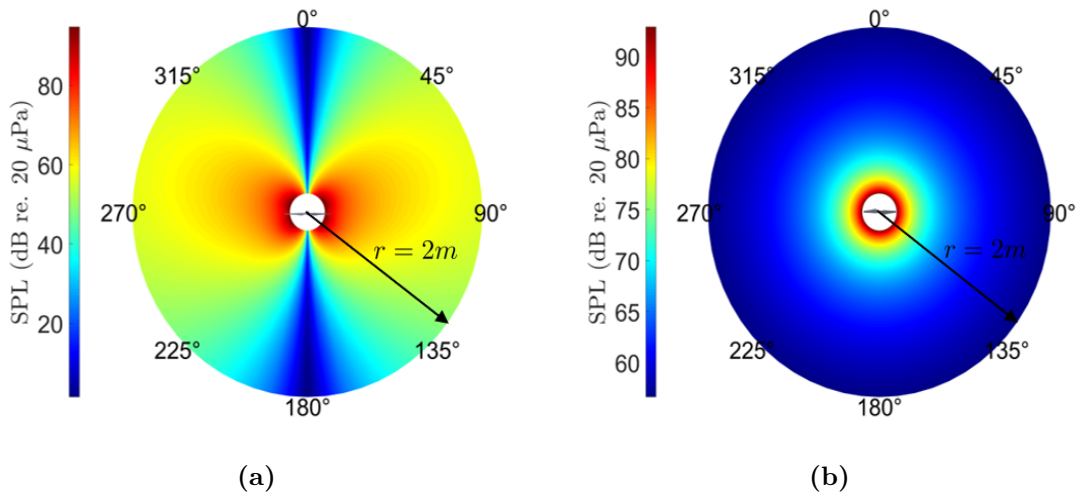


Figure 6.12: Radiation map in the $\theta = 90^\circ$ (a) and $\theta = 0^\circ$ (b) plane of the full acoustic field radiated by an isolated propeller represented by a circular array of phased dipoles.

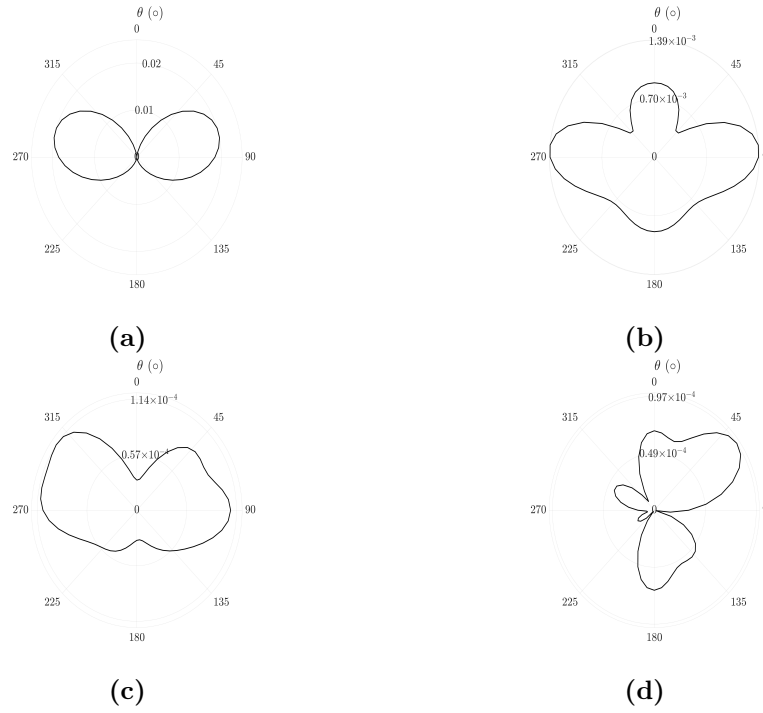


Figure 6.13: Free-field directivities plot in the $\theta = 90^\circ$ (a) plane for the isolated propeller configuration at different blade passing frequencies. (a) BPF (b) 2BPF (c) 3BPF (d) 5BPF.

6.3.2 Installation effect of a propeller in a quadcopter configuration

The effect of the interaction rotor-on-rotors and rotors-on-airframe is qualitatively analyzed considering the comparison of the radiation maps on xz plane between the results of case P and of a single propeller of case PD . A premise must be made. The analytical method used for the computation of the tonal noise from the aerodynamic forces is not integrated with any code which takes into consideration the scattering due to the presence of other surfaces. Therefore, the acoustic results discussed in this chapter allow only to give a first insight into the acoustics of the drone through the effect that the mentioned interactions have on the aerodynamic forces. In other words, only the acoustic field radiated in free-field conditions has been computed in this thesis, therefore the acoustic reflection has been neglected for the current results. However, considering the good agreement with other works previously demonstrated (Section 6.2.2), the current methodology permit to have a first view on the effect of the installation effects of a propeller.

The comparison of Figure 6.12 with Figure 6.14 shows that the unsteady aerodynamic loading introduced by the rotor interactions causes the lost of the classical

dipole directivity pattern (figure 6.14 (a)) and an increase of the sound pressure level, especially in the normal direction of the rotor plane ($\theta = 90^\circ$). Indeed, the biggest noticeable difference is related to the radiated sound along the rotor's axis direction. Indeed, in the case of the isolated rotor the region directly above the axis was definitely silent, but due to the presence of a surface below the rotors, a relatively high sound level is expected for an observer located upstream. This last finding is in accord with preceding works which treat the installation effects of propellers [32, 36]. Moreover, can be noticed a changing of the directivity pattern on the rotor plane, where the azimuthally symmetry has been lost respect of the isolated propeller case.

We can conclude that the rotor-on-rotor and rotor-on-airframe interaction affects the noise characteristics of the multi-rotor in a bigger way than what has been seen regarding the aerodynamic performance.

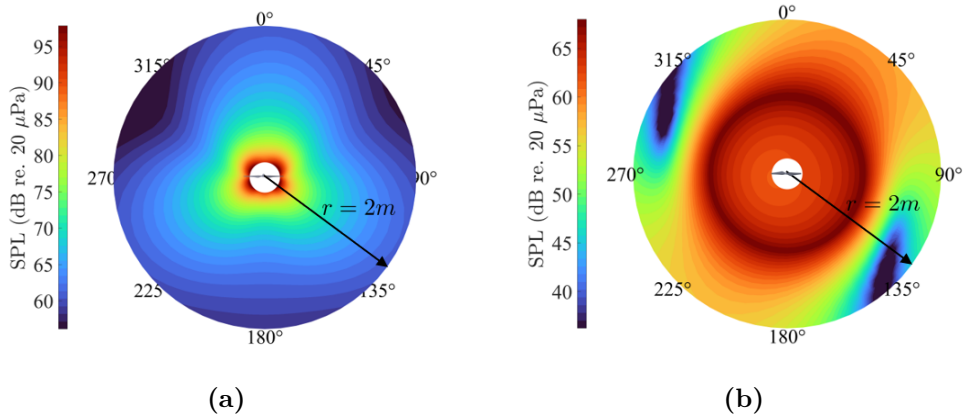


Figure 6.14: Radiation map in the $\theta = 90^\circ$ (a) and $\theta = 0^\circ$ (b) plane of the full acoustic field radiated by a quadcopter configuration represented by four circular array of phased dipoles.

Chapter 7

Conclusions and Future Works

The diffusion of the unmanned air vehicles for urban transportation runs into problems related to public acceptance of the noise level generated. The presence of close-spaced rotors and a closed downstream fuselage lead to aerodynamic interactions and acoustic scattering whose effects are a growing area of research. Many studies regarding the effect of the aerodynamic interactions on the aerodynamic performances have been realized, but few looked in-depth at the consequences on noise generation. In this study, the focus is set on multi-rotor configurations, looking in particular at the effect of the mentioned interactions on the unsteady loading of the rotors which directly affect the noise generation. Thus, this research aims to build a robust methodology for the prediction of the noise generated by multi-rotor configurations using a reasonable amount of computational resources, without a loss in terms of accuracy.

7.1 Conclusions

This research aimed to investigate a typical quadcopter configuration by using computational fluid dynamics integrated with an acoustic propagation method. The scope has been reached proceeding gradually beginning from simpler cases. The uRANS model is selected for the purpose of predicting the performance generated by the propellers, which represent the input data for the acoustic computation. A grid study is done for the finding of the best compromise between aerodynamic performance prediction and flow field resolution.

The following observations and conclusions were obtained based on the presented simulations:

- the CFD methodology was able to predict the thrust value within a 2% and 4% error from experimental data for the isolated propeller and quadcopter case, respectively;
- the computed tonal noise components show a good agreement with literature works at the first BPF, resulting in an error lower of 1% for both the isolated propeller and the quadcopter configuration;
- the aerodynamic interactions (rotor-rotor and rotor-fuselage) in the quadcopter case lead to a negligible decrease of the thrust produced by a single propeller (lower of the 2%);
- the aerodynamic interactions (rotor-rotor and rotor-fuselage) in the quadcopter case lead to an increasing of the sound pressure level of approximately $12dB$ in the rotor planes;
- the aerodynamic interactions (rotor-rotor and rotor-fuselage) in the quadcopter case lead to a change of the directivity pattern of the noise generated by a single propeller.

7.2 Perspectives

This thesis explored the tonal noise generated by both isolated propeller and quadcopter in hovering conditions through a low-order hybrid acoustic methodology. We suggest different directions for expanding upon or furthering the current study:

- the choice of studying only the classic quadcopter configuration is caused by the lacking of experimental researches, which is essential for the validation of the numerical results. Therefore, the literature review done for this study highlighted the necessity of the development of further experimental acoustic campaigns about multi-rotor configurations;
- the formulation of the Ffowcs-Williams and Hawkings implemented in this research is based on the aerodynamic forces generated on the blade surfaces, therefore these data must be correctly predicted by the CFD computation. Thus, the use of higher-order computational methods could show additional details of the effect of the aerodynamic interactions on the tonal noise generation;
- the effect of the aerodynamic interactions on the tonal noise has been investigated only through the effects on the aerodynamic forces. Therefore, the effect of the presence of surfaces has been neglected. Thus, the integration of the acoustic scattering effect in the acoustic propagation represents an

important step for the full understanding of the noise generated by multi-rotor configurations;

- the hovering configuration is the most studied in the literature for its relative simplicity and because it is a characteristic feature of the multi-rotor configuration. However, the extension of the presented study to the forward-flight case is fundamental. Indeed, the interactions between the wakes on the propeller's inflow conditions can be potentially added to the possible causes of the increase of the noise level between multi-rotor configuration and the isolated rotor case.

Appendix A

APC 9x4.5 MR Performance Table

V [m/s]	J	η	K_T	K_P	Torque [N·m]	Thrust [N]
0	0	0	0.117	0.048	0.058	3.919
0.581	0.030	0.061	0.116	0.048	0.059	3.874
1.162	0.050	0.119	0.115	0.049	0.060	3.830
1.743	0.080	0.175	0.113	0.049	0.060	3.781
2.325	0.100	0.228	0.111	0.050	0.061	3.723
2.906	0.130	0.278	0.109	0.050	0.061	3.661
3.487	0.150	0.325	0.107	0.050	0.061	3.585
4.068	0.180	0.370	0.105	0.051	0.061	3.505
4.649	0.200	0.412	0.102	0.050	0.061	3.412
5.230	0.230	0.452	0.099	0.050	0.061	3.309
5.812	0.250	0.488	0.096	0.050	0.061	3.203
6.393	0.280	0.522	0.092	0.050	0.060	3.083
6.974	0.310	0.553	0.088	0.049	0.060	2.958
7.555	0.330	0.581	0.084	0.048	0.059	2.825
8.136	0.360	0.606	0.080	0.047	0.058	2.687
8.717	0.380	0.628	0.076	0.046	0.056	2.544
9.298	0.410	0.648	0.072	0.045	0.055	2.398
9.880	0.430	0.665	0.067	0.044	0.053	2.242
10.505	0.460	0.680	0.062	0.042	0.051	2.086

Table A.1: Performance data of the APC9x4.5MR from [80] considering a rotation rate of 6000rpm.

Bibliography

- [1] Dario Floreano and Robert J. Wood. «Science, Technology and the Future of Small Autonomous Drones». In: *Nature* 521 (May 2015) (cit. on p. 1).
- [2] Prescient & Strategic Intelligence Private Limited. *Urban Air Mobility Market - UAM Industry Forecast, 2030*. 2020 (cit. on p. 1).
- [3] Research and Markets Ltd. *Unmanned Aircraft and Systems (UAS) Marketplace - Global and Regional Market Assessment and Forecasts, 2020 - 2025*. 2020 (cit. on p. 1).
- [4] U.S. Department of Transportation. *Integration of Civil Unmanned Aircraft Systems (UAS) in the National Airspace System (NAS) Roadmap*. 2013 (cit. on p. 1).
- [5] Christopher Courtin and Michael J. Burton. «Feasibility Study of Short Take-off and Landing Urban Air Mobility Vehicles Using Geometric Programming». In: American Institute of Aeronautics and Astronautics, June 2018 (cit. on p. 1).
- [6] Ohad Gur and Aviv Rosen. «Optimizing Electric Propulsion Systems for Unmanned Aerial Vehicles». In: *Journal of Aircraft* 46.4 (July 2009). DOI: 10.2514/1.41027 (cit. on p. 1).
- [7] Mike Cherney. «Delivery Drones Cheer Shoppers, Annoy Neighbors, Scare Dogs». In: *Wall Street Journal* (Dec. 2018) (cit. on p. 2).
- [8] Antonio J. Torija and Charlotte Clark. «A Psychoacoustic Approach to Building Knowledge about Human Response to Noise of Unmanned Aerial Vehicles». In: *IJERPH* (Jan. 2021). ISSN: 1660-4601. DOI: 10.3390/ijerph18020682 (cit. on p. 2).
- [9] «Rotor Interactional Effects on Aerodynamic and Noise Characteristics of a Small Multirotor Unmanned Aerial Vehicle». In: *Physics of Fluids* 32 (Apr. 2020). DOI: 10.1063/5.0003992 (cit. on pp. 2, 3, 88).
- [10] Steven S (ARC-TNF) Yoon. «Simulations of XV15 Rotor Flows in Hover Using Overflow». In: *NASA Ames Research Center* (2014) (cit. on pp. 2, 4, 45, 71).

- [11] Austin R Schenk. «Computational Investigation of the Effects of Rotor-on-Rotor Interactions on Thrust and Noise». PhD thesis. Brigham Young University, 2020 (cit. on pp. 2, 45, 49, 71).
- [12] Austin D Thai and Sheryl M Grace. «A Numerical Study of Important Flow Effects for Quadrotor Performance in Hover». In: *Boston University, Massachusetts*, (2015) (cit. on pp. 2, 3, 73).
- [13] Seokkwan Yoon, Patricia Ventura Diaz, D Douglas Boyd Jr, William M Chan, and Colin R Theodore. «Computational Aerodynamic Modeling of Small Quadcopter Vehicles». In: *AHS Forum 73* (2017), p. 16 (cit. on pp. 2, 3).
- [14] Nanyaporn Intaratep, William N. Alexander, William J. Devenport, Sheryl M. Grace, and Amanda Dropkin. «Experimental Study of Quadcopter Acoustics and Performance at Static Thrust Conditions». In: (May 2016). DOI: 10.2514/6.2016-2873 (cit. on pp. 2, 76, 86–88).
- [15] Nikolas S. Zawodny and Douglas D. Boyd. «Investigation of Rotor–Airframe Interaction Noise Associated with Small-Scale Rotary-Wing Unmanned Aircraft Systems». In: (Jan. 2020). DOI: 10.4050/JAHS.65.012007 (cit. on p. 3).
- [16] Wenwu Zhou, Zhe Ning, Haixing Li, and Hui Hu. «An Experimental Investigation on Rotor-to-Rotor Interactions of Small UAV Propellers». In: *American Institute of Aeronautics and Astronautics* (June 2017). DOI: 10.2514/6.2017-3744 (cit. on pp. 4, 71, 72).
- [17] Reda R. Mankbadi. *Transition, Turbulence, and Noise*. Boston, MA: Springer US, 1994. DOI: 10.1007/978-1-4615-2744-2 (cit. on p. 6).
- [18] S W Rienstra and A Hirschberg. *An Introduction to Acoustics*. July 2020 (cit. on pp. 8, 10).
- [19] George B. Arfken. *Mathematical methods for physicists*. 3rd ed. Academic Press, 1985 (cit. on p. 10).
- [20] Tapan K. Sengupta and Yogesh G. Bhumkar. *Computational Aerodynamics and Aeroacoustics*. Springer Singapore, 2020. DOI: 10.1007/978-981-15-4284-8 (cit. on p. 12).
- [21] Eric Manoha, Stephane Redonnet, and Stephane Caro. «Computational Aeroacoustics». en. In: *Encyclopedia of Aerospace Engineering* (2010) (cit. on p. 12).
- [22] Susann Boij. «The Influence of Flow Coupling on Sound Propagation in Flow Ducts». In: *Proceedings of the Tenth International Congress on Sound and Vibration* (Jan. 2003) (cit. on p. 13).

- [23] Anastasios S Lyrantzis. «Integral Methods in Computational Aeroacoustics -From the CFD Near-Field to the Acoustic Far-Field». In: (2002) (cit. on p. 13).
- [24] Lightill M. J. «On Sound Generated Aerodynamically I. General Theory». en. In: (1951) (cit. on pp. 13, 14).
- [25] Curle N. «The Influence of Solid Boundaries upon Aerodynamic Sound». In: *Philosophical Transactions of the Royal Society of London. Series A, Mathematical and Physical Sciences* (1955) (cit. on pp. 13, 17).
- [26] J. E. Ffowcs Williams and D. L. Hawkings. «Sound Generation by Turbulence and Surfaces in Arbitrary Motion». en. In: *Philosophical Transactions of the Royal Society of London. Series A, Mathematical and Physical Sciences* 264 (1969) (cit. on pp. 13, 19).
- [27] Gavin R Putland. «Exact Derivation of Kirchhoff's Integral Theorem and Diffraction Formula Using High-School Math». In: (2020) (cit. on p. 13).
- [28] Lightill M. J. «On Sound Generated Aerodynamically II. Turbulence as a Source of Sound». en. In: (1953) (cit. on p. 17).
- [29] Paolo Candeloro, Tiziano Pagliaroli, Daniele Ragni, and Silvia Di Francesco. «Small-Scale Rotor Aeroacoustics for Drone Propulsion: A Review of Noise Sources and Control Strategies». In: (Oct. 2019). DOI: 10.20944/preprints201910.0078.v1 (cit. on p. 22).
- [30] Stewart Glegg and William Devenport. «Open Rotor Noise». In: *Aeroacoustics of Low Mach Number Flows*. Elsevier, 2017. DOI: 10.1016/B978-0-12-809651-2.00016-3 (cit. on p. 22).
- [31] Giorgia Sinibaldi and Luca Marino. «Experimental Analysis on the Noise of Propellers for Small UAV». In: *Applied Acoustics* 74 (Jan. 2013). DOI: 10.1016/j.apacoust.2012.06.011 (cit. on p. 22).
- [32] M Roger and S Moreau. «Aero-Acoustic Installation Effects in Cooling Fan Systems Part 1: Scattering by Surrounding Surfaces». In: The 12th International Symposium on Transport Phenomena (2008) (cit. on pp. 23, 30, 91).
- [33] Michel Roger. «Near-Field Fan Noise Modeling and Installation Effects due to Scattering Surfaces». In: (2007) (cit. on pp. 23, 28).
- [34] Fink M.R. Hanson D. B. «The importance of quadrupole sources in prediction of transonic tip propeller noise». In: *Sound and Vib.* (1979) (cit. on p. 23).
- [35] M.E. Goldstein. *Aeroacoustics*. McGraw-Hill International Book Company, 1976. ISBN: 978-0-07-023685-1 (cit. on pp. 23, 28).

- [36] S Moreau, O Marck, and M Roger. «Aero-Acoustic Installation Effects in Cooling Fan Systems Part 2: Near-Field and Ground Effects». In: The 12th International Symposium on Transport Phenomena (2008) (cit. on pp. 24, 28, 91).
- [37] Hadrien Beriot, Gwenael Gabard, Karim Hamiche, and Michael Williamschen. «High-Order Unstructured Methods for Computational Aero-Acoustics». In: (Nov. 2015) (cit. on p. 24).
- [38] Michel Roger and Korcan Kucukcoskun. «Near-and-Far Field Modeling of Advanced Tail-Rotor Noise Using Source-Mode Expansions». In: *Journal of Sound and Vibration* (2019). DOI: 10.1016/j.jsv.2019.02.007 (cit. on p. 26).
- [39] L. Gutin. *On the Sound Field of a Rotating Propeller*. Physical magazine of the Soviet Union (Translated by NACA Technical Memorandums), 1948 (cit. on p. 28).
- [40] S.B. Pope, P.J. Eccles, S.B. Pope, and Press. *Turbulent Flows*. Cambridge University Press, 2000 (cit. on pp. 32, 39).
- [41] David S.-K. Ting, ed. *Basics of Engineering Turbulence*. London, U.K: Academic Press is an imprint of Elsevier, 2016 (cit. on p. 32).
- [42] O. Reynolds. «IV. On the Dynamical Theory of Incompressible Viscous Fluids and the Determination of the Criterion». In: *Phil. Trans. R. Soc. Lond. A* 186 (Dec. 1895). DOI: 10.1098/rsta.1895.0004 (cit. on pp. 34, 35).
- [43] Steven A. Orszag. «Analytical Theories of Turbulence». In: *J. Fluid Mech.* 41 (Apr. 1970). DOI: 10.1017/S0022112070000642 (cit. on p. 34).
- [44] Yang Zhiyin. «Large-Eddy Simulation: Past, Present and the Future». In: *Chinese Journal of Aeronautics* 28 (Feb. 2015). DOI: 10.1016/j.cja.2014.12.007 (cit. on p. 34).
- [45] D.C. Wilcox. *Turbulence Modeling for CFD*. Turbulence Modeling for CFD v. 1. DCW Industries, 2006 (cit. on pp. 35, 36, 39, 41).
- [46] A. Kolmogorov. «The Local Structure of Turbulence in Incompressible Viscous Fluid for Very Large Reynolds' Numbers». In: *Akademiia Nauk SSSR Doklady* 30 (Jan. 1941) (cit. on p. 35).
- [47] Paul A Durbin. «Turbulence Closure Models for Computational Fluid Dynamics». In: *Aerospace Engineering Publications*. 2018 (cit. on p. 36).
- [48] Giancarlo Alfonsi. «Reynolds-Averaged Navier–Stokes Equations for Turbulence Modeling». In: *Applied Mechanics Reviews* 62 (July 2009). DOI: 10.1115/1.3124648 (cit. on p. 36).

-
- [49] Charles Mockett. «A Comprehensive Study of Detached-Eddy Simulation». In: () (cit. on p. 37).
- [50] Paul G. Tucker. *Computation of Unsteady Internal Flows*. Boston, MA: Springer US, 2001. DOI: 10.1007/978-1-4615-1439-8 (cit. on p. 37).
- [51] W. Haase, ed. *FLOMANIA: A European Initiative on Flow Physics Modelling: Results of the European-Union Funded Project, 2002-2004*. Notes on Numerical Fluid Mechanics and Multidisciplinary Design. Berlin ; New York: Springer, 2006 (cit. on p. 37).
- [52] P. A. Durbin. «Separated Flow Computations with the K-Epsilon-v-Squared Model». In: *AIAA Journal* 33 (Apr. 1995). DOI: 10.2514/3.12628 (cit. on p. 37).
- [53] J. Boussinesq. «Théorie des ondes et des remous qui se propagent le long d'un canal rectangulaire horizontal, en communiquant au liquide contenu dans ce canal des vitesses sensiblement pareilles de la surface au fond.» In: *Journal de Mathématiques Pures et Appliquées* (1872) (cit. on p. 37).
- [54] Joseph (1842-1929) Auteur du texte Boussinesq. «Essai sur la théorie des eaux courantes / par J. Boussinesq». In: (1877) (cit. on pp. 37, 38).
- [55] R.J. Garde. *Turbulent Flow*. New Age Science, 2010 (cit. on p. 38).
- [56] L. Prandtl. «7. Bericht über Untersuchungen zur ausgebildeten Turbulenz». In: *Z. Angew. Math. Mech.* 5 (1925). DOI: 10.1002/zamm.19250050212 (cit. on p. 38).
- [57] A. N. Kolmogorov. «Equations of turbulent motion in an incompressible fluid». In: *Proceedings of the USSR Academy of Sciences* 30 (1941) (cit. on pp. 39, 41).
- [58] Ludwig Prandtl and Karl Wieghardt. *Über ein neues Formelsystem für die ausgebildete Turbulenz*. Vandenhoeck & Ruprecht, 1947 (cit. on p. 39).
- [59] P R Spalart. «Strategies for Turbulence Modelling and Simulations». In: (2000) (cit. on p. 39).
- [60] B. E. Launder and D. B. Spalding. *Lectures in mathematical models of turbulence [by] B. E. Launder and D. B. Spalding*. Academic Press London, New York, 1972 (cit. on p. 40).
- [61] B E Launder and B I Sharma. «Application of the Energy-Dissipation Model of Turbulence to the Calculation of Flow Near a Spinning Disc». In: *Lett Heat Mass Trans.* 1 (1974) (cit. on p. 40).
- [62] Bengt Andersson, ed. *Computational Fluid Dynamics for Engineers*. Cambridge ; New York: Cambridge University Press, 2012. ISBN: 978-1-107-01895-2 (cit. on p. 40).

- [63] V. Yakhot, S. A. Orszag, S. Thangam, T. B. Gatski, and C. G. Speziale. «Development of Turbulence Models for Shear Flows by a Double Expansion Technique». In: *Physics of Fluids A: Fluid Dynamics* 4 (July 1992). DOI: 10.1063/1.858424 (cit. on p. 41).
- [64] Tsan-Hsing Shih, William W. Liou, Aamir Shabbir, Zhigang Yang, and Jiang Zhu. «A New K- ε Eddy Viscosity Model for High Reynolds Number Turbulent Flows». In: *Computers & Fluids* 24 (1995). DOI: 10.1016/0045-7930(94)00032-T (cit. on p. 41).
- [65] D. Wilcox and R. Traci. «A Complete Model of Turbulence». In: *9th Fluid and Plasma Dynamics Conference*. American Institute of Aeronautics and Astronautics, July 1976. DOI: 10.2514/6.1976-351 (cit. on p. 41).
- [66] David C. Wilcox. «Reassessment of the Scale-Determining Equation for Advanced Turbulence Models». In: *AIAA Journal* 26 (Nov. 1988). DOI: 10.2514/3.10041 (cit. on p. 41).
- [67] Johan C. Kok. «Resolving the Dependence on Freestream Values for the K-Omega Turbulence Model». In: *AIAA Journal* 38 (Jan. 2000). DOI: 10.2514/3.14547 (cit. on p. 42).
- [68] F. R. Menter. «Influence of Freestream Values on K-Omega Turbulence Model Predictions». In: *AIAA Journal* 30 (June 1992). DOI: 10.2514/3.11115 (cit. on p. 42).
- [69] F. R. Menter. «Two-Equation Eddy-Viscosity Turbulence Models for Engineering Applications». In: *AIAA Journal* (Aug. 1994). DOI: 10.2514/3.12149 (cit. on pp. 42, 50).
- [70] *Fluid Mechanics 101* (cit. on p. 43).
- [71] C. Russell, G. Willink, and C. Theodore. «Wind Tunnel and Hover Performance Test Results for Multicopter UAS Vehicles». In: *TM—2018–219758 NASA Ames* (2018) (cit. on pp. 44, 53, 63, 64, 70).
- [72] Siemens Digital Industries Software, ed. *Star CCM+ User Guide*. 2020 (cit. on pp. 45, 48, 49, 51, 54, 58).
- [73] M. Baris Dogruoz and Gokul Shankaran. «Computations with the Multiple Reference Frame Technique: Flow and Temperature Fields Downstream of an Axial Fan». In: *Numerical Heat Transfer, Part A: Applications* 71 (Mar. 2017). DOI: 10.1080/10407782.2016.1277930 (cit. on p. 47).
- [74] Austin Thai and Sheryl M. Grace. «Prediction of Small Quadrotor Blade Induced Noise». In: *25th AIAA/CEAS Aeroacoustics Conference* (May 2019). DOI: 10.2514/6.2019-2684 (cit. on pp. 49, 69, 70).

- [75] Patricia Ventura Diaz and Steven Yoon. «Computational Study of NASA’s Quadrotor Urban Air Taxi Concept». In: (2020). DOI: 10.2514/6.2020-0302 (cit. on p. 50).
- [76] Patricia Ventura Diaz and Steven Yoon. «High-Fidelity Computational Aerodynamics of Multi-Rotor Unmanned Aerial Vehicles». In: *American Institute of Aeronautics and Astronautics* (Jan. 2018). DOI: 10.2514/6.2018-1266 (cit. on pp. 50, 64, 65).
- [77] Zhenyu Wang and Pandey. «A Comprehensive Approach to Study Aerodynamic and Aeroacoustic Performances of Small Multicopter Unmanned Aerial Systems». In: *American Institute of Aeronautics and Astronautics* (Jan. 2018). DOI: 10.2514/6.2018-0268 (cit. on p. 55).
- [78] Jennifer N. Abras and Nathan Hariharan. «Comparison of Computational Fluid Dynamics Hover Predictions on the S-76 Rotor». In: *Journal of Aircraft* (Jan. 2018). DOI: 10.2514/1.C034121 (cit. on p. 55).
- [79] Ideen Sadrehaghghi. *Mesh Generation in CFD*. 2020 (cit. on p. 56).
- [80] *APC Propeller Performance Data*. URL: https://www.apcprop.com/files/PER3%5C_9x45MR.dat (cit. on pp. 62, 63, 71, 97).
- [81] Robert W. Deters, Stefan Kleinke, and Michael S. Selig. «Static Testing of Propulsion Elements for Small Multirotor Unmanned Aerial Vehicles». In: *American Institute of Aeronautics and Astronautics* (June 2017). DOI: 10.2514/6.2017-3743 (cit. on pp. 62, 63).
- [82] Dhwanil Shukla and Narayanan Komerath. «Multirotor Drone Aerodynamic Interaction Investigation». In: *Drones* (Dec. 2018). DOI: 10.3390/drones2040043 (cit. on p. 72).
- [83] Nikolas S Zawodny, D Douglas Boyd Jr, and Randolph H Cabell. «Combined Experimental and Computational Aeroacoustic Analysis of an Isolated UAV-Scale Propeller». In: (2015) (cit. on pp. 76, 83–86).
- [84] Alain Guédel. *Acoustique des ventilateurs*. fr. Villeurbanne, France: PYC Livres, 1999 (cit. on p. 84).